Copyright

by

Michael Adewunmi Asoro

2012

The Dissertation Committee for Michael Adewunmi Asoro certifies that this is the approved version of the following dissertation:

Coalescence and Sintering in Metallic Nanoparticles: *In-situ* Transmission Electron Microscopy (TEM) Study

Committee:

Paulo J. Ferreira, Supervisor

Desiderio Kovar, Co-Supervisor

Llewellyn K. Rabenberg

Jeremy P. Meyers

Michael F. Becker

Coalescence and Sintering in Metallic Nanoparticles: *In-situ* Transmission Electron Microscopy (TEM) Study

by

Michael Adewunmi Asoro, B.S.; M.S.E.

Dissertation

Presented to the Faculty of the Graduate School of

The University of Texas at Austin

in Partial Fulfillment

of the Requirements

for the Degree of

Doctor of Philosophy

The University of Texas at Austin

May 2012

Dedication

I dedicate this dissertation to the Almighty God for his grace and to my family for their love and support.

Acknowledgements

I would like to thank my research supervisor, Prof. Paulo Ferreira and co-supervisor Prof. Desiderio Kovar for their support and guidance throughout my journey in graduate school. I am very grateful to both of you for introducing me to nanomaterials research and for letting me work on such an interesting project. I would also like to thank my committee members: Prof. Llewellyn Rabenberg, Prof. Jeremy Meyers and Prof. Michael Becker for serving on my committee and providing very valuable feedback on my research.

My gratitude goes to Dr. Ji-Ping Zhou, the Transmission Electron Microscopy (TEM) facility manager for teaching me how to use the equipment used for this research. I also thank Dr. Domingo Ferrer, Dr. Dwight Romanovicz, Dr. Arturo Ponce (University of Texas at San Antonio) and Dr. Lawrence Allard (Oak Ridge National laboratory) for their help with the other microscopes used. In addition, I would like to thank Dr. Stephen Mick and Dr. John Damiano from Protochips Inc. for their collaboration regarding the *in-situ* TEM heating instrumentation used for this work. I would like to acknowledge the assistance of Manuj Nahar, Michael Gammage and Guillaume Noiseau in preparing some of the samples used for the experiments and my lab mates: Jai Ganesh, Karalee Jarvis, Shreyas Rajasekhara and Daniel Groom for all their help and valuable discussions. I thank Sandia National Laboratory and National Science Foundation for providing financial support for this work.

Also, I would like to thank my uncle, Mr. Taiwo Asoro and his family for making me feel at home here in Texas, thousands of miles away from my parents and siblings. I thank my brother, Bayo Asoro for his encouragement and support during my graduate studies and my uncle back home, Dr. Lekan Gbadamosi for always supporting me to finish my PhD. Lastly I would like to thank my wife and best friend, Tosin Abiodun for going through graduate school experience with me for five years and for bearing with me during the long evenings and weekends spent in the lab.

Coalescence and Sintering in Metallic Nanoparticles: *In-situ* Transmission Electron Microscopy (TEM) Study

Michael Adewunmi Asoro, Ph.D.

The University of Texas at Austin, 2012

Supervisors: Paulo J. Ferreira and Desiderio Kovar

Nanoparticles possess unique physical, chemical, optical and electronic properties stemming from their nanoscale dimensions and are currently used in catalysis, microelectronics, drug delivery, as well as other applications. However, due to their large surface area-to-volume ratio, nanoparticles have a strong tendency to coalesce and sinter during processing or usage over short time scales and at low temperatures, which lead to significant changes in behavior and performance. In this work, *in-situ* transmission electron microscopy (TEM) heating has been used to investigate the effects of particle size, temperature and carbon capping layers on sintering in face-centered cubic (FCC) metallic nanoparticles. For the first time, we make direct and real-time measurements of nanoparticle size, neck growth, dihedral angle and grain boundary motion during sintering, which are then used to calculate fundamental material transport parameters such as surface diffusivity and grain boundary mobility. We observe that carbon surface coatings typically present on most commercial nanoparticles can significantly inhibit sintering in nanoparticles. Also, a new mechanism for coalescence in nanoparticles is shown where small clusters on the support can initiate neck growth by forming a bridge between the nanoparticles consisting of individual atoms or small clusters of atoms. *In-situ* TEM experiments provide critical and valuable real-time dynamic information for

direct investigation of the link between the evolution of sintering and controlling mechanisms, which conventional experiments such as post-mortem TEM observations are not capable of conveying.

Table of Contents

List of Tables

List of Figures

Chapter 1: Introduction

1.1 Motivation

The 21st century has been characterized by a growing research interest in the study of new and challenging materials for both industrial and commercial applications. Of particular importance is the area of nanomaterials, which is a study of materials with extremely small feature sizes, less than 100 nm. Nanoparticles, classified as zero-dimensional (0-D) nanomaterials, (because all of its dimensions are confined to the nanoscale) exhibit unique size-dependent properties due to the large fraction of their surface atoms compared to bulk materials [1-5]. These unique physical, chemical, optical and electronic properties are already being exploited for applications in areas such as chemical catalysis, microelectronics, biological sensors and other applications [6-12]. For example in the semiconductor fabrication industry, the need for faster microprocessors has led to a continued decrease in the dimensions of electronic devices to the nanometer range and according to Moore's law [13], the current 32 nm technology is expected to shrink further to 11 nm or less by 2015 [14].

Materials typically exhibit novel behavior when the size of the building blocks is smaller than the critical length scale of a particular property. For metals, the mean free path of an electron at room temperature is about 10 nm to 100 nm, and one would therefore predict that as the characteristic length of metals is decreased to nanoscale dimensions; unusual effects would be observed in the material's physical behavior and properties. For example, gold nanoparticles less than 100 nm in diameter appear red (not

gold) when suspended in transparent media [15], and gold nanoparticles of diameter less than 3 nm are no longer noble and unreactive, but can be used to catalyze chemical reactions [16, 17].

However, it is important that nanoparticles remain thermally stable in order to be used for these applications. Due to their large surface area-to-volume ratio, nanoparticles have a strong tendency to coalesce and sinter during processing or usage, over short time scales, which can lead to significant changes in their desirable properties with subsequent changes in behavior and performance. In some applications, such as catalysis, coalescence is detrimental. For example, the coalescence of platinum nanoparticles catalysts used in proton exchange membrane fuel cells is responsible for a reduction in the electrochemically active surface area of the nanoparticles, which leads to an undesired catalyst deactivation and subsequent reduction in cell performance after several cycles [18, 19]. In other situations, such as in the fabrication of thick film conductors, the ability to enhance sintering is beneficial because it allows high conductivity lines to be produced at low temperatures and would therefore open the door to the development of many novel devices. For example, silver nanoparticles that are readily sintered at low temperatures have been proposed as a viable lead-free alternative to conventional lead solders used for semiconductor device interconnect applications, due to its low processing temperature, high electrical and thermal conductivity and ability to withstand high operating temperatures [20-22].

Fundamentally, it is therefore important to understand the sintering process at the nanoscale so that we can better control sintering in nanoparticles and tailor nanoparticles

for different applications. One important question is whether the coalescence and sintering of nanoparticles shows the same size dependencies as larger particles. In general, as particle size is reduced, an enhancement in sintering kinetics is predicted from simple scaling models such as Herring's law [23] and other analytical models [24-26]. However, these models do not accurately predict the particle size dependence of sintering behavior at the nanoscale. For example, data from micron-sized particles that are extrapolated to the nanoscale and correspondingly lower process temperatures consistently fail to predict the sintering kinetics of nanoparticles [27-29]. Groza [28] and Yeadon *et al*. [29] both describe experiments in which sintering occurs at temperatures that are far below that which would be predicted from conventional scaling models that account only for the increased curvature that occurs as particle size is reduced. Possible reasons for these differences include 1) unique defect structures in nanoparticles (twins and facets) [27], 2) enhanced diffusivity due to size or temperature effects, 3) enhanced, localized agglomeration present in nanoparticles. However, to date, the reasons for the discrepancies between models and experimental results remain uncertain.

1.2 Approach

In-situ transmission electron microscopy (TEM) heating is used to conduct sintering experiments by directly heating the nanoparticles while imaging in the microscope. This technique allows us to monitor the response of a material to an external applied stimulus, (e.g. heat) in real-time as opposed to conventional post-mortem TEM observations of the material after firing in a furnace. The *in-situ* experiments are

performed in both conventional bright field (BF) TEM using phase-contrast imaging and aberration-corrected high angle annular dark field (HAADF) scanning transmission electron microscopy (STEM) using Z-contrast imaging. The aberration-corrected STEM is ideal for imaging small nanoparticles, atomic clusters and single atoms supported on a carbon substrate. The HAADF or Z-contrast images show a pure mass-thickness contrast and zero diffraction contrast, and is therefore a powerful technique for observing the coalescence process, particularly the development of the neck region between two particles due to variations in thickness in that region. For the *in-situ* heating, we used a novel Aduro^{TM} heating stage designed by Protochips Inc. (Raleigh, NC) which provides very stable heating with minimal thermal drift for high resolution imaging and is capable of achieving nearly instantaneous heating and cooling.

This *in-situ* TEM heating capability is combined with an analysis methodology that allow direct measurements of fundamental mass transport parameters that are important in understanding coalescence and sintering at the nanoscale. For the first time, we make direct, real-time measurements of nanoparticle size, neck growth, dihedral angle and grain boundary motion during coalescence and sintering. The surface diffusivity is then calculated from measurements obtained from the images acquired during the initial stages of sintering and the grain boundary mobility is determined from measurements made during the latter stages of sintering.

This work focuses on FCC metallic nanoparticles using platinum and silver as model systems, since these are very important metallic nanoparticles both from an academic and industrial application perspective. The FCC system is chosen for this study

because it is well understood in the literature and most of the earlier sintering experiments were done on micron-sized particles of FCC metals like silver, copper and gold. Therefore our results on FCC metallic nanoparticles can be readily compared with previous findings in order to study size effects. The choice of silver and platinum allows us to study noble metals with a wide range of melting temperatures and their relative inertness makes them suitable for *in-situ* TEM heating experiments, without suffering from oxidation or contamination. However, this methodology can also be extended to other systems as well.

1.3 Objectives and Main Contributions

1.3.1 Objectives

To address the aforementioned issues, the primary objective of this dissertation is to study the fundamental mechanisms that influence low temperature (less than 0.5 T_m, where T_m is the melting temperature) sintering of FCC metallic nanoparticles. These experiments will allow us to:

1. Determine how particle size and temperature influence sintering of metallic nanoparticles, by directly measuring the neck growth and dihedral angle as a function of time.
2. Measure the influence of particle size, temperature and carbon surface layers, on fundamental mass transport parameters like surface diffusivity and grain boundary mobility for nanoparticles.

3. Determine the possible mass transfer mechanisms for sintering in nanoparticles, such as Ostwald ripening or particle migration and coalescence.
4. Determine the extent to which the electron beam, which is utilized for the *in-situ* TEM/STEM heating experiments, influences the measured mass transport rates.

1.3.2 Main Contributions

The main contributions of this dissertation are as follows:

1. *In-situ* TEM/STEM heating of silver and platinum nanoparticles to monitor coalescence and sintering in nanoparticles. The TEM experiments were performed on larger nanoparticles (greater than 5 nm in diameter) using phase contrast imaging while the STEM experiments were performed on smaller nanoparticles (less than 5 nm in diameter) using Z-contrast imaging. The STEM experiments were carried out in an aberration-corrected microscope, which provides sub-Angstrom resolution and thus allows single atomic columns to be clearly identified within each nanoparticle.

2. Development of a measurement procedure to make direct, real-time measurements of nanoparticle size, neck growth, dihedral angle and grain boundary motion during sintering. This is achieved by doing a least-square fitting of a circle on projections from nearly spherical nanoparticles so that a two particle sintering model can be used to obtain sintering parameters needed to calculate mass transport parameters like surface diffusion coefficient and grain boundary mobility as a function of particle size and temperature.

3. Development of a temperature calibration method for *in-situ* heating experiments in a TEM using a known solid-to-vapor phase transformation. The sublimation kinetics of silver nanoparticles is monitored by measuring the change of particle radius, due to sublimation, with time when heated at a fixed temperature, which is then compared to previous theoretical models [30] based on the Kelvin equation [31]. Because the sublimation rate is highly sensitive to temperature, this method can serve as an excellent calibration tool.

1.4 Organization of the Dissertation

The dissertation is organized as follows:

In chapter 2, the current state of understanding is presented. The chapter starts with an introduction to sintering by reviewing the literature on ceramic processing and powder metallurgy, where sintering of ceramics and high melting point metals are well understood. The fundamental global driving force for sintering - which is a reduction in energy of the system - is then discussed as is the rationale for enhanced driving force for nanoparticles. The local driving for sintering, sintering mechanisms and sintering models for the different stages of sintering are also discussed. Subsequently, the chapter focuses on the recent findings from the literature related to the sintering of nanoparticles.

In chapter 3, the experimental procedure used for this work is presented. In particular, the *in-situ* TEM/STEM heating experiment is explained with emphasis on the novel Protochips *in-situ* TEM heating holder used. The temperature calibration of the heating holder as well as the effect of electron beam heating on *in-situ* TEM experiments

is then presented. The measurement procedure used for the determination of particle radius, neck radius and dihedral angle during sintering is also discussed.

Chapter 4 presents the results of sintering in silver and platinum nanoparticles obtained from *in-situ* TEM/STEM heating experiments. The measured particle radius, neck radius and dihedral angle are then presented. Also, TEM/STEM images showing possible mechanisms for mass transfer in sintering of nanoparticles such as Ostwald ripening or particle migration and coalescence are also presented.

In chapter 5, the results obtained are analyzed, first by using the measurements of neck growth during sintering to calculate fundamental material transport parameters such as surface diffusion coefficient and grain boundary mobility. The effects of particle size, temperature and carbon surface coatings on sintering are then presented.

Lastly, chapter 6 presents the final conclusions from this study and provides some recommendations for future work.

Chapter 2: State of Understanding

2.1 Introduction

Sintering is traditionally used in ceramic processing and powder metallurgy as a processing technique for producing density-controlled materials and components from ceramic and metal powders. This processing technique typically starts with fine (1 – 2 μm) powder that is first formed into a porous "green" part, and then fired at high temperature in a furnace so that the particles in contact form a neck and bond together to give a dense part though the process of sintering. A typical relative density following sintering is greater than 95% of the theoretical density. Historically, sintering was used for ceramics and high melting point metals like tungsten and molybdenum because the very high temperatures required for processing these materials using conventional casting methods makes it too expensive to use conventional processing routes. The other major advantage is that sintering is a near-net shape process and therefore reduces the need for mechanical machining and increases material yield compared to conventional processing methods.

Sintering processes can be classified as either solid state sintering or liquid phase sintering. During solid state sintering, the powders do not melt but the joining together of the particles and the reduction in the porosity of the powder compact occurs by atomic diffusion in the solid state. Typical temperatures for solid state sintering are $0.5T_m < T < 0.9T_m$. Liquid phase sintering occurs when a liquid phase is present in the powder compact during sintering. For this dissertation, we will focus on solid state sintering.

2.2 Driving Force for Sintering

Sintering can be described using either the global driving force or the local driving force. The global driving force relates to the thermodynamics of the system, i.e. the lowest energy state of the system. Although the global driving force is a useful tool for understanding the evolution of the microstructure, descriptions of the kinetics of the sintering process usually utilize the local driving force.

2.2.1 Global Driving Force

In general, the possible global driving forces for sintering are: 1) a reduction in energy of the particles, 2) an externally applied pressure, or 3) a chemical reaction. For pressureless sintering of noble or semi-noble metallic nanoparticles, which are the foci of this dissertation, only the reduction in energy is considered. The reduction of the total surface free energy of the consolidated mass of particles is achieved by atomic diffusion processes that lead to densification, coarsening, or a combination of the two. Densification occurs by transport of matter from inside the grains into the pores, leading to shrinkage while coarsening occurs by rearrangement of matter between different parts of the pore surfaces without a decrease in the pore volume.

Mathematically, the total surface energy of a powder compact can be expressed as $\gamma \cdot A$, where γ is the specific surface energy and A is the total surface area of the compact. Therefore, the reduction of the total surface energy, $\Delta(\gamma \cdot A)$ can be expressed as:

$$\Delta(\gamma \cdot A) = (\Delta\gamma) \cdot A + \gamma \cdot (\Delta A) \tag{2.1}$$

where $\Delta\gamma$ is the change in surface energy per unit area and ΔA is the change in surface area. For coarsening, the reduction in energy is due to a decrease in surface area while for densification, the reduction in energy is due to the replacement of surfaces by grain boundaries, since the grain boundary energy is usually lower than the surface energy. The densification and coarsening processes occurring during sintering are shown schematically in Figure 2.1 and they both lead to an overall reduction in energy of the system. The change in energy becomes significant when the radius of curvature is less than a few microns (a 4 J/g decrease in free energy occurs on sintering 1 μm particles), which is one of the main reasons why fine powder particles are utilized for sintering of metallic or ceramic particles. For nanoparticles, which have particle diameters less than 100 nm, we expect an even larger effect since the global driving force for sintering is significantly greater than it is for micron-sized particles.

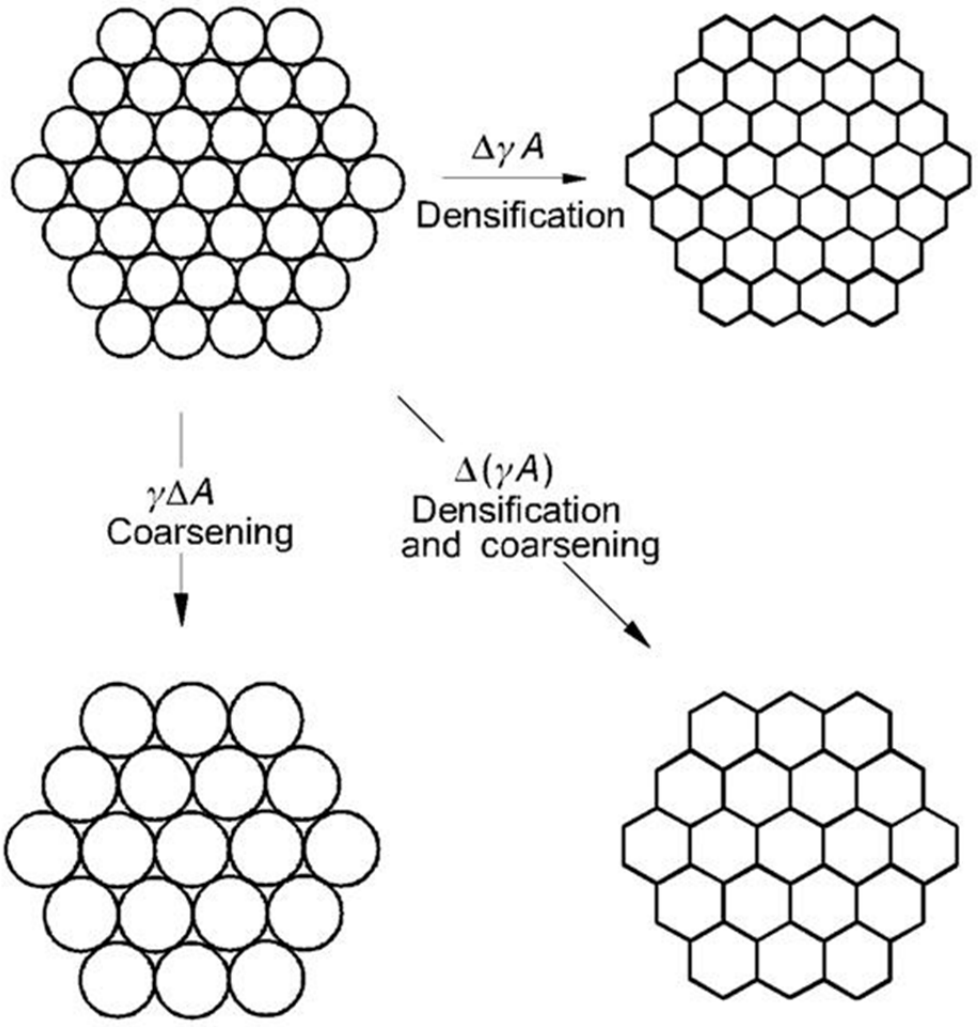

Figure 2.1: Schematic of the densification and coarsening processes occurring during sintering. Taken from ref. [32].

2.2.2 Local Driving Force

To accomplish the sintering process within a reasonable time, we must consider the kinetics of matter transport, which is dependent on the local or kinetic driving force for sintering. In its simplest form, matter transport can be analyzed in terms of Fick's first

law of diffusion by considering the flux of atoms or vacancies driven by gradients in the concentration. The flux of the diffusing species, J (number of atoms crossing unit area, normal to the direction of flux, per second) is proportional to the concentration gradient dC/dx and occurs in the direction of decreasing concentration. Mathematically, Fick's first law (in one dimension) is given by:

$$J_x = -D\frac{dC}{dx} \tag{2.2}$$

where the constant of proportionality D is called the diffusion coefficient or diffusivity (units of m^2/s or cm^2/s). The diffusion coefficient is a temperature-dependent material property that can be used to characterize the rate of diffusive mass transport.

Using a more general definition of local driving force, diffusion is said to be driven by gradients in chemical potential (molar Gibbs free energy) rather than gradients in concentration only. This is because the atoms can respond to other driving forces such as a gradient in pressure. The gradient in chemical potential can then be due to gradients in atom or vacancy concentration as well as bulk pressure or vapor pressure gradients.

The atoms and vacancies beneath a curved surface will have their chemical potentials altered by the curvature of the surface, and this difference in chemical potential drives the diffusional flux of atoms to reduce the free energy of the system. Thus, the curvature of the particle surfaces provides the main local driving force for sintering to occur and the chemical potential is related to the curvature by the following expression:

$$\Delta\mu = \gamma\Omega\Delta\kappa \tag{2.3}$$

where $\Delta\mu$ is the change in chemical potential due to a change in curvature $\Delta\kappa$, γ is surface energy and Ω is atomic volume.

Matter transport occurs predominantly by diffusion of atoms, or equivalently, the counter flow of vacancies from regions of higher chemical potential to regions of lower chemical potential. From Fick's law of diffusion, the diffusional flux of atoms, J_a or vacancies, J_v can then be rewritten as:

$$J_a = -J_v = -\frac{D_a C_a}{\Omega k T} \cdot \frac{d(\mu_a - \mu_v)}{dx} \tag{2.4}$$

where D_a is the atomic self diffusion coefficient, C_a is the fraction of lattice sites occupied by the atoms, Ω is atomic volume, k is Boltzmann constant, T is temperature, μ_a is the chemical potential of the atom and μ_v is the chemical potential of the vacancy.

Thus, in terms of kinetics, the differences in atom or vacancy concentration, bulk pressure and vapor pressure due to interface curvature induce material transport. If we consider a curved interface between a condensed phase and a dispersed phase (Figure 2.2), the pressure in region I with a convex surface (positive curvature) is higher than that in region II with a concave surface (negative curvature) according to the Young-Laplace equation [32]. In addition, because of the pressure difference, the vapor pressure above

region I is higher than that above region II. On the other hand, for a vacancy, which can be considered as a dispersed phase of vacuum, region I has a negative curvature and region II a positive curvature from the vacuum side. Thus, the equilibrium vacancy concentration in region II is higher than that in region I. The difference in vacancy concentration leads to a diffusional flux of vacancies from the concave region (neck) to the convex region (surface) or equivalently, a diffusional flux of atoms from the convex region to the concave region to reduce the free energy of the system. The curvature is inversely related to the radius; therefore for particles with smaller radius (or larger curvature), there is even a larger local driving force for sintering.

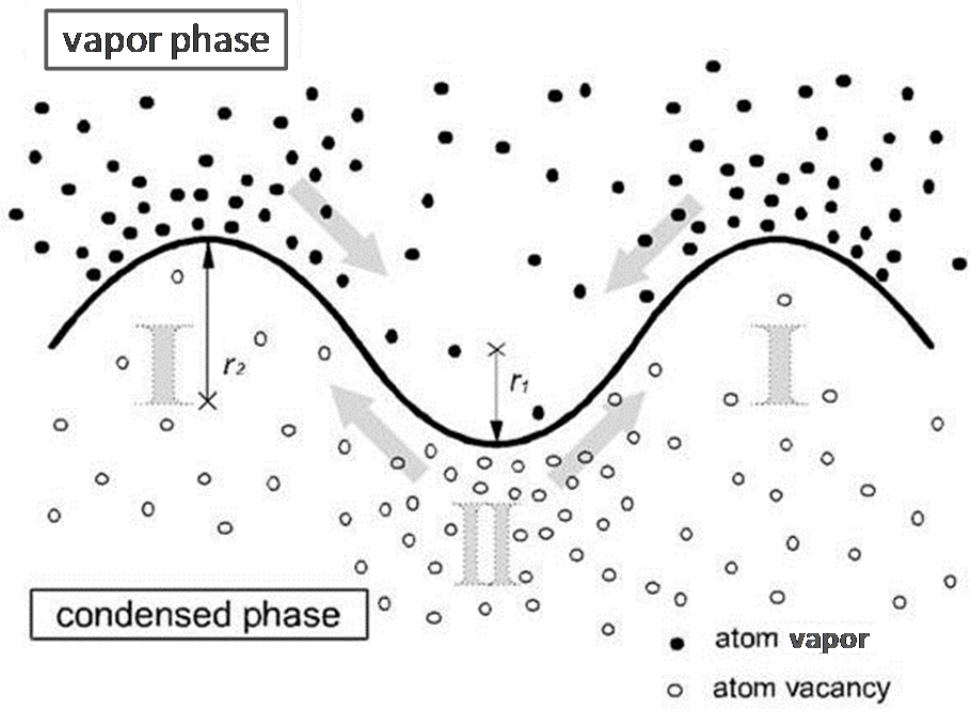

Figure 2.2: Schematic showing distribution of vacancies and vapor atoms near a curved interface. Taken from ref. [32].

2.3 Sintering Mechanisms

Sintering occurs by diffusion of atoms along definite paths in the microstructure that define the mechanisms of sintering. Matter is transported from regions of higher chemical potential (source) to regions of lower chemical potential (sink). The six sintering mechanisms in polycrystalline materials are described below and shown schematically in Figure 2.3.

1. Surface diffusion: diffusion of atoms along the surface of a particle.
2. Lattice or volume diffusion from the surface: atoms from the surface diffuse through the lattice.
3. Vapor transport: evaporation of atoms from the surface which condense on a different surface.
4. Grain boundary diffusion: atoms diffuse along the grain boundary.
5. Lattice diffusion from the grain boundary: atoms from grain boundary diffuse through lattice.
6. Plastic flow: dislocation motion causes flow of matter.

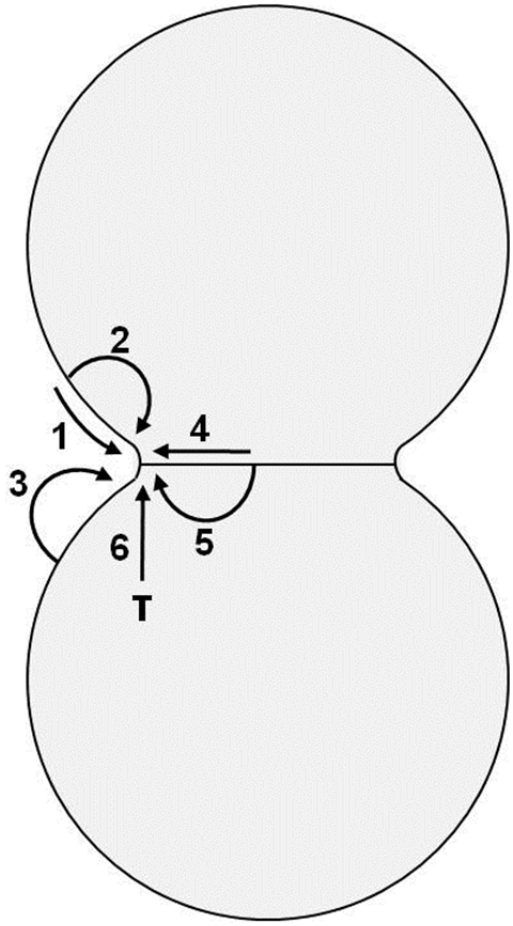

Figure 2.3: The six different sintering mechanisms in crystalline materials: (1) surface diffusion, (2) lattice diffusion from the surface, (3) vapor transport, (4) grain boundary diffusion, (5) lattice diffusion from the grain boundary, and (6) plastic flow.

The sintering mechanisms can also be classified as either densifying or non-densifying. Surface diffusion, lattice diffusion from the particle surfaces to the neck, and vapor transport lead to neck growth without densification and are referred to as non-densifying mechanisms. These mechanisms simply take atoms from the surface and rearrange them onto another surface without causing pore shrinkage. Therefore when

material is transported to the neck from the particle surface, interparticle distance is not reduced but the neck size is increased by redistribution of material. Grain boundary diffusion, lattice diffusion from the grain boundary to the pore and plastic flow by dislocation motion lead to neck growth and densification and are referred to as densifying mechanisms. Atoms are moved from the bulk to the surface of pores thereby eliminating porosity and increasing the density of the sample. The interparticle distance is reduced by material transport from the grain boundary via atomic diffusion. Therefore, the grain boundary is the source of material transport for densification and shrinkage in crystalline powder compacts.

In summary, Table 2.1 lists the six major sintering mechanisms as well as the corresponding material source and sink. In practice, material transport due to the difference in interface curvature can occur under the parallel actions of various sintering mechanisms, which can make sintering analysis difficult. The dominant mechanism can vary depending on particle size, neck radius, temperature and time for a given system.

Table 2.1 Sintering mechanisms in polycrystalline solids

Sintering mechanism	**Material source**	**Material sink**
1. Surface diffusion	Surface	Neck
2. Lattice diffusion	Surface	Neck
3. Vapor transport	Surface	Neck
4. Grain boundary diffusion	Grain boundary	Neck
5. Lattice diffusion	Grain boundary	Neck
6. Plastic flow	Dislocations	Neck

2.4 Stages of Sintering

Solid state sintering is usually divided into three stages - initial, intermediate and final. A stage represents an interval of time or density over which the microstructure is considered to be reasonably well defined. The initial stage is characterized by the formation of necks between particles. During the intermediate stage, considerable densification, up to about 90% of the relative density, occurs before isolation of the pores. The final stage involves densification from the isolated pore state to the final densification. For polycrystalline materials, the idealized geometrical structures that were suggested by Coble [33] as representative of the three sintering stages are shown in Figure 2.4.

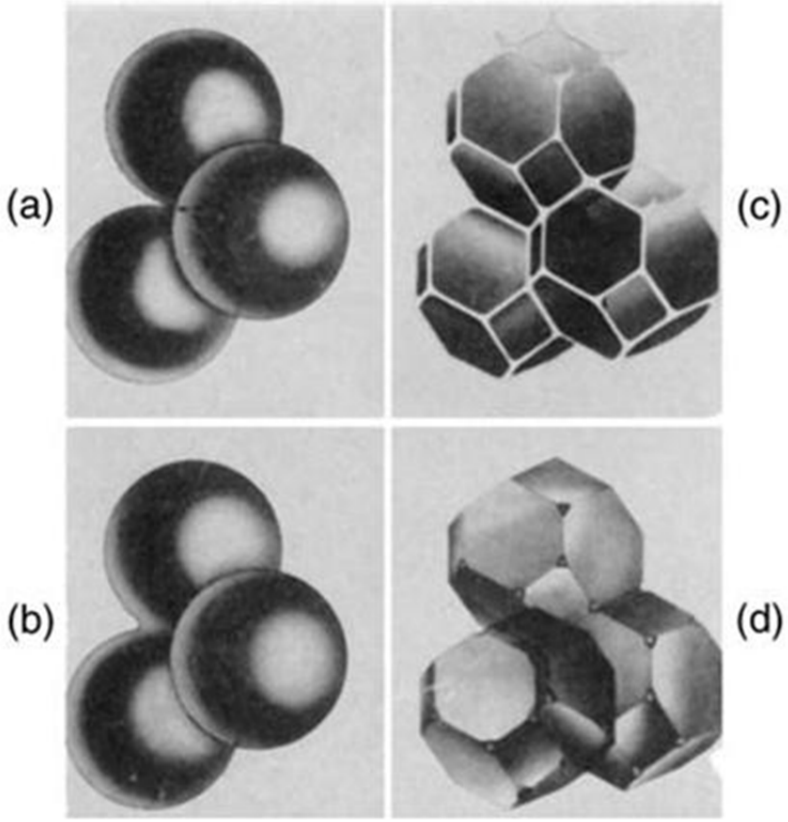

Figure 2.4: Idealized models for the three stages of sintering. (a) Initial stage: model structure represented by spheres in tangential contact. (b) Near the end of the initial stage: spheres have begun to coalesce and there is neck growth with shrinkage of about 4%. (c) Intermediate stage: dark grains have adopted the shape of a tetrakaidecahedron, enclosing white pore channels at the grain edges. (d) Final stage: pores are tetrahedral inclusions at the corners where four tetrakaidecahedra meet. Taken from ref [33].

2.4.1 Initial Stage Sintering

The initial stage is characterized by fairly rapid interparticle neck growth. During this stage, the large initial differences in surface curvature are removed and shrinkage

accompanies neck growth for the densifying mechanisms. For a system of spherical particles, the initial stage is represented as the transition between Figs. 2.4a and 2.4b. It is assumed to last until the neck radius reaches a value of about 0.4 - 0.5 of the initial particle radius. For a powder system with an initial density of 50% - 60% of the theoretical density, this corresponds to a linear shrinkage of 3 - 5% or an increase in density to about 65% of the theoretical density when the densifying mechanisms dominate.

2.4.2 Intermediate Stage Sintering

The intermediate stage begins when the pores have reached their equilibrium shapes as dictated by the balance between the surface and interfacial tensions at the point where the grain boundary intersects the pore, i.e. tension in the solid-vapor interface and tension in the grain boundary. The pore phase is still continuous and the structure is usually idealized in terms of a spaghetti-like array of porosity residing along the grain edges as illustrated in Figure 2.4c. Densification occurs as the pore diameter is reduced until the pores become unstable and pinch off, leaving isolated pores. The intermediate stage normally covers the major part of the sintering process, and it is assumed to last until the density reaches about 90% of the theoretical density.

2.4.3 Final Stage Sintering

The final stage begins when the pores pinch off and become isolated at the grain corners, as shown by the idealized structure in Fig. 2.4d. The pores are assumed to shrink

continuously and may disappear altogether when final densification is achieved. The typical density in the final stage is greater than 90% of the theoretical density and it approaches the theoretical density if all of the porosity can be removed.

In summary, the main parameters associated with the three stages of sintering are shown in Table 2.2, and examples of the microstructures from real powder compacts sintering in the initial, intermediate, and final stages are shown in Figure 2.5 [34]. The focus of this dissertation is on the initial stage of sintering, since the intermediate and final stages of sintering cannot be analyzed by a system of two particles with no pores between them. Also, from an application standpoint, the initial stage is most crucial because once the sintering process starts, rapid neck growth occurs and the property of the nanoparticles is already affected.

Table 2.2 Parameters associated with the stages of sintering for polycrystalline solids

Stage	**Typical microstructural feature**	**Relative density range**	**Idealized model**
Initial	Rapid inter-particle neck growth	Up to ~0.65	Two monosize spheres in contact
Intermediate	Equilibrium pore shape with continuous porosity	~0.65 ~ 0.90	Tetrakaidecahedron with cylindrical pores of the same radius along the edges
Final	Equilibrium pore shape with isolated porosity	Above ~0.90	Tetrakaidecahedron with spherical monosize pores at the corners

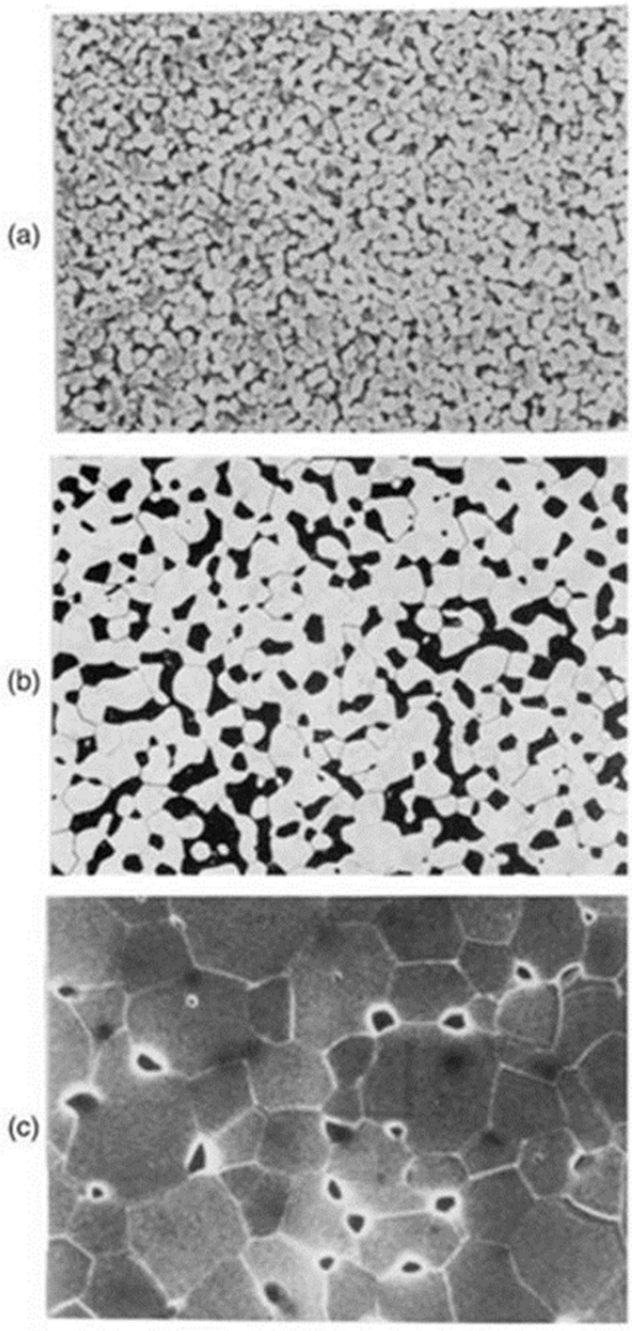

Figure 2.5: Examples of real microstructures for (a) initial stage sintering, (b) intermediate stage sintering, and (c) final stage sintering. Taken from ref. [34].

2.5 Solid State Sintering Models

A variety of theoretical approaches have been used to analyze sintering process in ceramic and metal powders including: scaling laws [23], analytical models [24-26, 33, 35-37], numerical simulations [38-41], topological models [42] and phenomenological models [43, 44]. For this dissertation, we will focus mainly on analytical models because of their relevance to understanding of sintering mechanisms and kinetics. We should note that these models only provide a qualitative description of sintering of larger masses of powder particles because the simplifications assumed in the models make them unsuitable for quantitatively predicting the sintering behavior of real powder systems. For, example, the models assume uniform packing of monosize spherical particles, the occurrence of a single mass transport mechanism and no grain growth. In spite of these shortcomings, these theoretical models provide valuable insight into the sintering processes for powder systems. In addition, the idealized geometries assumed in the models can be readily reproduced for model experiments.

2.5.1 Analytical Models

The analytical models provide a basis for understanding the sintering kinetics for each sintering mechanism by solving appropriate mass transport equations. The models assume that the initial powder compact consists of monosize, spherical particles that are uniformly packed. With these assumptions, a unit of the powder system, called the geometrical model, can be isolated and analyzed. With appropriate boundary conditions,

the remainder of the powder system is then considered as a continuum having the same macroscopic properties (e.g. shrinkage and densification rate) as the isolated unit.

In contrast to the idealized model, in real powder systems, the microstructure of the compact changes continuously during sintering, making it difficult to determine a single geometrical model that can adequately represent the entire process, yet still provide the degree of simplicity required for the mass transport equations to be solved analytically. Therefore, different simplified models are used for the three stages of sintering. For each stage, an idealized geometry that has a rough similarity with the microstructure of the powder system is assumed. A two-particle model is used for the initial stage; the channel pore model is used for the intermediate stage and the isolated pore model is used for the final stage.

2.5.1.1 Initial Stage Model

2.5.1.1.1 Geometrical Parameters

The initial stage two-particle model consists of two equal-sized spheres in contact. Figure 2.8 shows two geometrical models for two spherical particles: (a) without shrinkage (non-densifying mechanisms) and (b) with shrinkage (densifying mechanisms). In the model for the non-densifying mechanisms, the distance between the particles does not change but the neck size increases as the sintering time increases while the model for the densifying mechanisms accounts for interpenetration of the spheres (i.e. shrinkage) as well as neck growth.

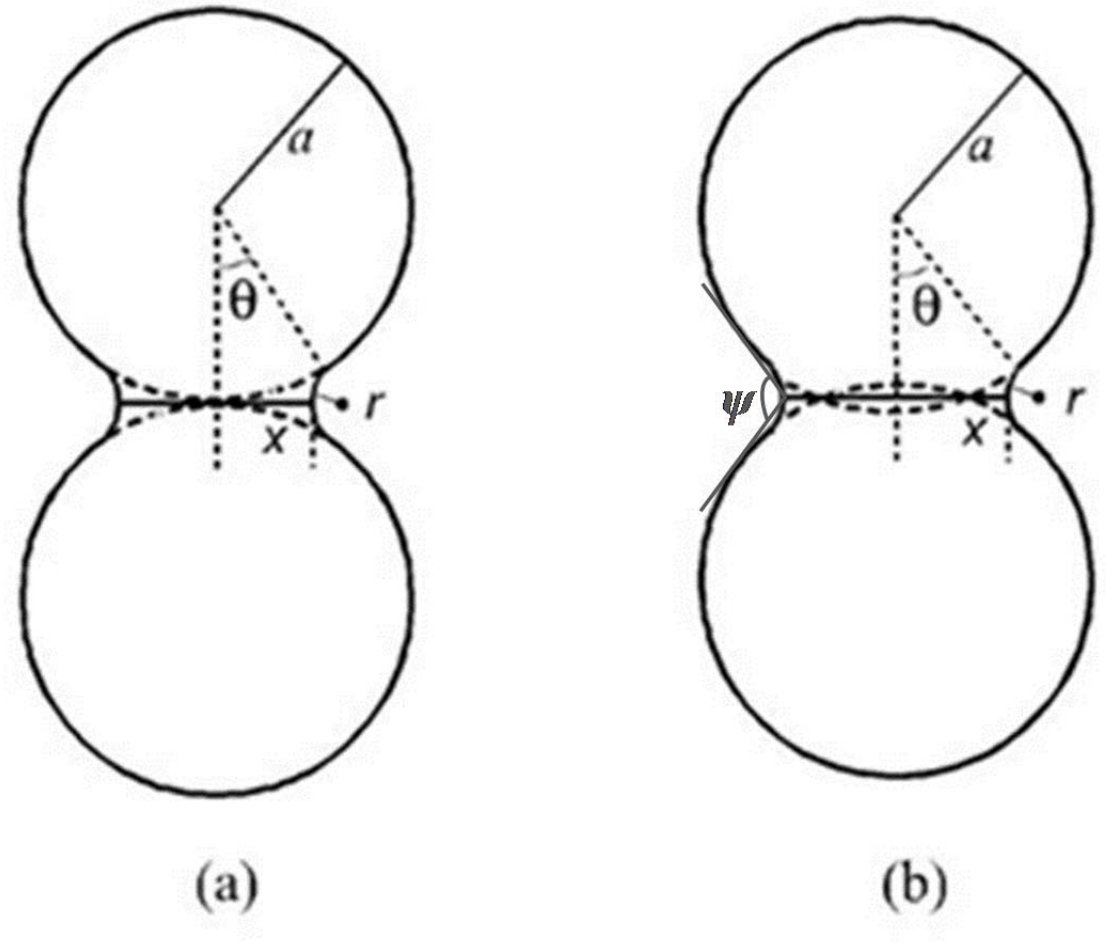

Figure 2.6: Two-particle model for initial stage sintering (a) without shrinkage and (b) with shrinkage [32].

The neck formed between the particles is assumed to be circular with a radius, x and a surface having a circular cross section of radius, r. If the dihedral angle, ψ between the particles is 180° and the grain size does not change during sintering, the main geometrical parameters of the model, which include: the radius of curvature of the neck surface r, the neck radius x, the area of the neck surface A, and the volume of material

transported into the neck V for the geometry without shrinkage [Figure 2.6(a)] are given by:

$$r \approx \frac{x^2}{2a} \tag{2.5}$$

$$A \approx 2\pi x 2r = \frac{2\pi x^3}{a} \tag{2.6}$$

$$V = \int A dx = \frac{\pi x^4}{2a} \tag{2.7}$$

where, a is the particle radius, and for the geometry with shrinkage [Figure 2.6(b)], the parameters are given by:

$$r \approx \frac{x^2}{4a} \tag{2.8}$$

$$A \approx \frac{\pi x^3}{a} \tag{2.9}$$

$$V \approx \frac{(\pi x^2 2r)}{2} = \frac{\pi x^4}{4a} \tag{2.10}$$

Comparing both set of equations, we see that the values of the parameters for the densifying model are one-half of those for the non-densifying model. If the dihedral angle is less than 180° as in real powder systems, the values of r are larger than those in equation (2.5) and equation (2.8). In the absence of shrinkage, r is calculated to be [45]:

$$r = \frac{x^2}{2a\left[1 - \left(\frac{x}{a}\right) sin\frac{\psi}{2} - cos\frac{\psi}{2}\right]}$$

$$\approx \frac{x^2}{2a\left(1 - cos\frac{\psi}{2}\right)} \quad \text{for } \left(\frac{x}{a} \ll 1\right) \tag{2.11}$$

2.5.1.1.2 Kinetic Equations

The sintering equations have been formulated by substituting the derived geometrical parameters in the mass transport equations for all six sintering mechanisms, which are then solved under appropriate boundary conditions [24-26, 35]. The equations for neck growth and shrinkage (for the densifying mechanisms) can be expressed in the general form:

$$\left(\frac{x}{a}\right)^m = \frac{H}{a^n} t \tag{2.12}$$

and

$$\left(\frac{\Delta L}{L_o}\right)^m = -\frac{H}{2^m a^n} t \tag{2.13}$$

where *m* and *n* are integer exponents that depend on the sintering mechanism, *H* is a function that contains the geometrical and material parameters of the powder system and the other variables have the same meaning as defined previously. Plausible values for the numerical constants *m*, *n*, and *H* for each mechanism are given in Table 2.3 [45]. For the non-densifying mechanisms, where there is no shrinkage, $\Delta L/L_0 = 0$.

Table 2.3 Plausible values for the numerical constants in equations (2.12) and (2.13).

Sintering Mechanism	***M***	***n***	***H***
Surface diffusion	7	4	$\frac{56D_s\delta_s\gamma_{sv}\Omega}{kT}$
Lattice diffusion from the surface	4	3	$\frac{20D_l\gamma_{sv}\Omega}{kT}$
Vapor transport	3	2	$\frac{3p_o\gamma_{sv}\Omega}{(2\pi mkT)^{1/2}kT}$
Grain boundary diffusion	6	4	$\frac{96D_{gb}\delta_{gb}\gamma_{sv}\Omega}{kT}$
Lattice diffusion from the grain boundary	5	3	$\frac{80\pi D_l\gamma_{sv}\Omega}{kT}$
Viscous flow	2	1	$\frac{3\gamma_{sv}}{2\eta}$

D_s, D_l and D_{gb} are the diffusion coefficients for surface, lattice, and grain boundary diffusion; δ_s, and δ_{gb} are the diffusion thickness for surface and grain boundary diffusion; γ_{sv} is the specific surface energy; p_0 is the vapor pressure over a flat surface; m is the mass of atom; k is the Boltzmann constant; T is the absolute temperature; η is the viscosity.

2.5.1.1.3 Application and Limitation of the Initial Stage Analytical Model

From equation (2.12), a plot of $\log(x/a)$ versus $\log t$ will yield a straight line with a slope equal to $1/m$, so by fitting the theoretical predictions to experimental data, the value of m can be found. A similar analysis can be applied to the case when shrinkage occurs by using both equations (2.12) and (2.13). Experimental data for validating the models are commonly obtained by measuring the neck growth in simple systems (e.g.

two spheres or a sphere on a plate) or the shrinkage in a compacted mass of spherical particles. Since *m* is dependent on the mechanism of sintering, in principle, the measurement of *m* allows the mechanism of sintering to be determined, assuming a single dominant mass transport mechanism. However, in real powder systems, it is possible to have more than one mechanism operating simultaneously and, when this occurs; the measured value of exponent is misleading. This is a major limitation of using the analytical model for predicting sintering mechanisms. Also, the assumption that the two-sphere geometry can be extended to real powder compacts is valid only if the particles are spheres of the same size arranged in a uniform pattern e.g., the uniform consolidation of monodisperse powders produced by colloidal methods [46]. The model also assumes that the dihedral angle is 180° or that the grain boundary energy is zero, which is not physically realistic. However, results from a sintering model which includes the dihedral angle [47] shows that the neglect of the grain boundary energy is insignificant if the dihedral angle is greater than 150°.

2.5.1.2 Intermediate Stage Model

Although the focus of this dissertation involves initial stage sintering, it is useful to also review later stage sintering models. Coble proposed a simple geometrical model called the channel pore model for the shape changes of pores during intermediate stage sintering [33]. The model is based on bcc-packed tetrakaidecahedral grains with cylindrical pores along the grain edges, as shown in Figure 2.7. This intermediate stage model assumes equal shrinkage of pores in a radial direction. Although the model is

limited in terms of describing real sintering, it allows the evaluation of the effect of sintering variables on sintering kinetics. Since the model assumes that the pore geometry is uniform, non-densifying mechanisms cannot operate and we can only consider the densifying mechanisms.

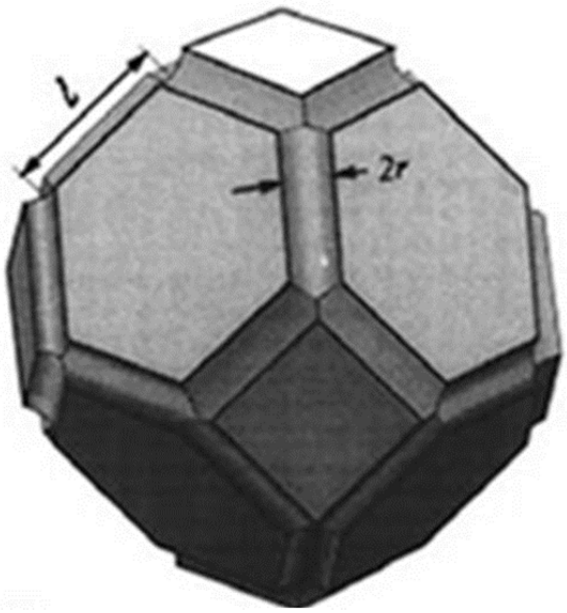

Figure 2.7: Coble's geometrical model for intermediate stage sintering. Taken from ref. [32].

The kinetic equations for sintering are commonly expressed in terms of the densification rate ($d\rho/dt$). For example, the densification rate during intermediate stage sintering, assuming that lattice diffusion and grain boundary diffusion are the dominant mass transport mechanisms are given respectively by:

$$\frac{d\rho}{dt} \approx \frac{10 D_l \gamma_{sv} \Omega}{G^3 kT} \tag{2.14}$$

and

$$\frac{d\rho}{dt} \approx \frac{4 D_{gb} \delta_{gb} \gamma_{sv} \Omega}{3(1-\rho)^{1/2} G^4 kT} \tag{2.15}$$

where G is the grain size, ρ is the density and all the other constants have the same meaning as before.

Therefore, from equation (2.14), the densification rate at a fixed density is predicted to depend inversely as the cube of the grain size for lattice diffusion, which is in agreement with the prediction from Herring's scaling law. From equation (2.15) for grain boundary diffusion, the densification rate at a fixed density is predicted to vary inversely as the fourth power of the grain size, as also predicted by the scaling law.

2.5.1.3 Final Stage Model

For the final stage of sintering, Coble proposed a geometrical model called the isolated pore model [33]. The model is based on tetrakaidecahedral grains with spherical pores of the same size at their corners, as shown in Figure 2.8. As in the intermediate stage, the uniform pore geometry assumed in these models precludes the consideration of non-densifying mechanisms. Therefore, final stage sintering models have been developed only for densifying mechanisms. The sintering equation for lattice diffusion is given by:

$$P_s = \frac{6\pi}{\sqrt{2}}\left(\frac{D_l \gamma_{sv} \Omega}{G^3 kT}\right)\left(t_f - t\right) \tag{2.16}$$

where P_s is the porosity at a time t, t_f is the time when the pore vanishes and all the other constants have the same meaning as before. This equation shows that the densification rate is inversely proportional to the cube of grain size, which is the same as that found for the dependence of neck growth and shrinkage on particle size in the initial stage model.

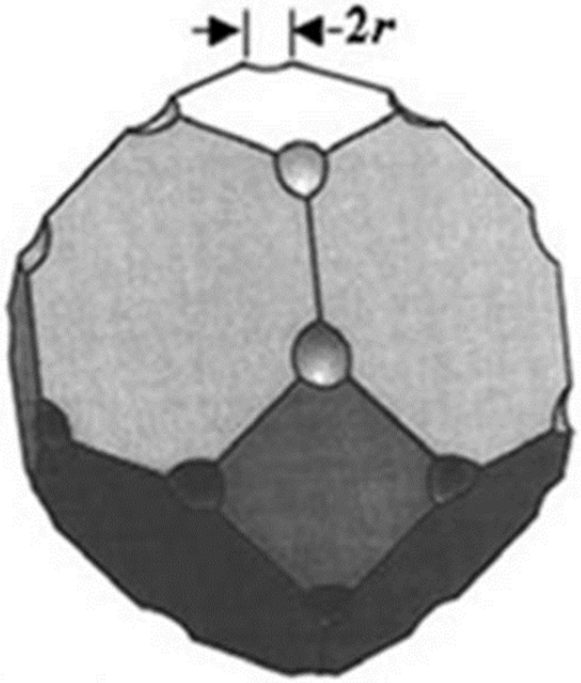

Figure 2.8: Coble's geometrical model for final stage sintering. Taken from ref. [32].

2.6 Sintering Variables

In order to prepare a material with a particular set of properties, it is important to understand which factors influence sintering and the resultant microstructure. The major variables which determine sinterability and the sintered microstructure of a powder compact can be classified as either material variables or process variables. The material variables include: particle size, particle shape, particle size distribution, degree of powder agglomeration, chemical composition, impurity, homogeneity, etc. The process variables on the other hand, are mostly thermodynamic variables related to the sintering conditions and they include: temperature, time, atmosphere, pressure, heating and cooling rate. For experimental studies, some variables such as the sintering temperature, applied pressure, average particle size, and sintering atmosphere, can be easily controlled with sufficient accuracy while other variables such as the powder agglomeration and particle packing are more difficult to control.

2.6.1 Effect of Sintering Variables on Sintering Kinetics

In general, the sintering (or densification) rate increases with decreased particle size and increased sintering temperature and pressure as shown schematically in Figure 2.9. This trend is in agreement with the theoretical predictions from the analytical models. The effects of some of the sintering variables on sintering kinetics are further discussed below.

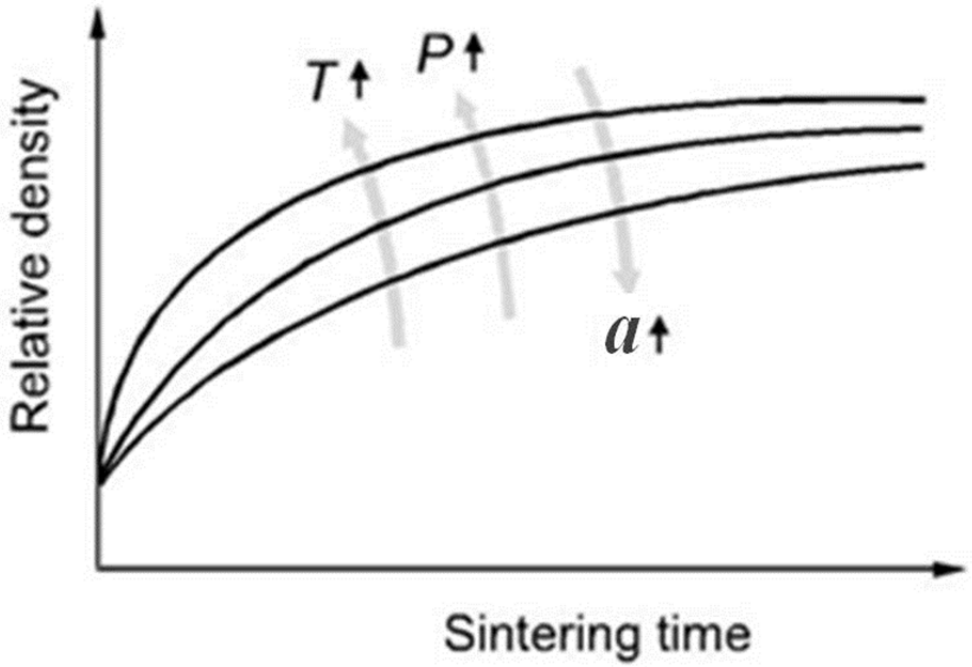

Figure 2.9: Effect of sintering variables: temperature (*T*), pressure (*P*) and particle size (*a*) on densification.

2.6.1.1 Particle Size

Herring's scaling law [23] can be used to explain the effect of changes in particle size on the sintering rate. When powders with different sizes but similar shapes are sintered under the same experimental conditions and by the same sintering mechanism, the scaling law predicts the relative time required to get the same degree of sintering. For the sintering of two powder systems with radii a_1 and a_2, where $a_2 = \lambda \cdot a_1$, the required sintering times t_2 and t_1 are given by:

$$t_2 = (\lambda)^{\alpha} t_1 \qquad (2.17)$$

where λ is the ratio of particles sizes a_2/a_1 and α is an exponent that depends on the dominant sintering mechanism. The values of α for the different sintering mechanisms are given in Table 2.4. Therefore, if a_2 is less than a_1, t_2 will be less than t_1, which implies that the sintering rate will increase with a decrease in particle size.

Table 2.4 Exponents for Herring's scaling laws described by equation (2.17).

Sintering Mechanism	**Exponent (α)**
Surface diffusion	4
Lattice diffusion	3
Vapor transport	2
Grain boundary diffusion	4
Plastic flow	1

The scaling law assumes that the same sintering mechanism is maintained during the sintering of the different powders and that the microstructure evolves with a self-similar shape. This requirement of similar shape changes is a key limitation of the scaling laws because it usually does not occur in sintering of real powder systems. Also, the sintering mechanism may change with the size of the particles during sintering. Nevertheless, Herring's scaling law demonstrates, in a simple way, the effect of particle

size on microstructural changes in powder compacts that are sintered under the same sintering condition.

2.6.1.2 Temperature

Like all thermally activated processes, the sintering rate increases with an increase in temperature. The effect of temperature on the sintering rate can also be predicted quantitatively from the kinetic equations in the analytical models. The equations contain some variables that are very sensitive to temperature such as diffusivity and viscosity, which are usually expressed by an Arrhenius-type exponential function of temperature. Therefore the sintering time will be inversely proportional to the sintering temperature, and the sintering rate will increase exponentially with temperature.

2.6.1.3 Pressure

The kinetic equations in the analytical models were derived for systems where the capillary pressure difference due to curvature difference was the main driving force for sintering. However, when an external pressure, P_{appl} is applied, the total sintering pressure P_t is the sum of the capillary and external pressures, given by:

$$P_t = \frac{\gamma_s}{r} + P_{appl.} f(\rho, geo) \tag{2.18}$$

where $f(\rho, geo)$ is a function of relative density and particle geometry.

Therefore, application of an external pressure to a powder compact provides an additional driving force for sintering and leads to an increase in the sintering rate. The pressure can be applied either unidirectionally or isostatically, generally known as hot pressing or hot isostatic pressing respectively. An example of hot pressing is spark plasma sintering while gas pressure sintering is an example of hot isostatic pressing.

2.7 Sintering of Nanoparticles

Nanoparticles that reside on a support surface, due to their excess surface free energy, are essentially in a metastable state and will inevitably tend to combine into larger structures, which represents a lower energy state, through the process of sintering [48-50]. The sintering of supported nanoparticles occurs by 1) a process similar to Ostwald ripening or 2) particle migration and coalescence [51, 52]. Traditional Ostwald ripening involves atomic migration by diffusion of atoms from smaller to larger particles through a solution phase that exists between the particles. In the case of separated particles sitting on a support, an analogous "surface ripening process" can be described in which individual atoms are removed from one particle surface, diffuse across the support surface, and then are re-deposited onto the second particle surface. The driving force for ripening comes from the higher chemical potential of the atoms in small particles as a consequence of their radius of curvature. This form of Ostwald ripening is favored for immobile particles that adhere strongly to the support and are well spaced apart.

Coalescence on the other hand, involves crystallite migration where by entire particles (crystallites) migrate along the surface and merge after making contact.

Coalescence is favored for a high density of nanoparticles, which adhere poorly to the surface, permitting them to diffuse easily and coalesce on contact. The driving force for the coalescence of two nanoparticles is a reduction of the total surface energy due to a reduction in the surface area, because the surface area of the new nanoparticle will be less than the sum of the surface areas of the two original nanoparticles. This driving force increases with decreasing particle size, since the surface area to volume ratio is inversely proportional to nanoparticle size. The coalescence process begins with initial contact of the particles followed by neck growth with or without shrinkage. Particle rotation or orientational alignment of coalescing planes at the interface between the particles then occurs, which leads to a lowering of the energy at the grain boundary, as shown by molecular dynamics simulations [53-56] and experimental observations [57-59].

2.7.1 Theoretical Analysis of Nanoparticle Sintering

The sintering of powder compacts with complex-shaped particles of different sizes cannot be explained in a simple manner. However, if spherical particles of the same size are assumed, an idealized model can be considered consisting of two particles, as shown in Figure 2.10, known as the two-particle sintering model.

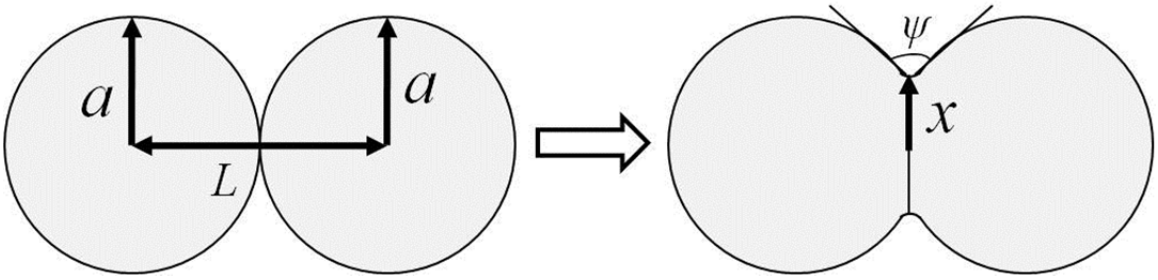

Figure 2.10: Two particle model of sintering between two spherical nanoparticles of radius a, with an interparticle distance, L. x is the neck radius and ψ is the dihedral angle.

During the early stages of sintering, neck growth occurs to reduce the large chemical potential at the particle contact points where the neck radius is very small. Possible mass transport mechanisms for neck growth include grain boundary diffusion, surface diffusion, lattice diffusion, as well as deformation. For nanoparticles, the diffusion mechanisms are more likely to dominate the sintering behavior. Indeed, it is unlikely that dislocation-driven plastic flow would contribute significantly to neck growth in face centered cubic (FCC) nanoparticles given the large stresses required for plastic flow in a nanoparticulate system [60]. Surface diffusion mechanism will be predominant at lower temperatures especially for small particles which have larger surface atom-to-volume atom ratios, as shown by the experiments of Kuczynski [25]. Also, at lower temperatures, the surface diffusivity for FCC metals is at least many orders of magnitude larger than the other diffusivities [61].

For surface diffusion, the change in neck radius, x with time, t for a given particle radius, a and temperature, T is given by the following expression [24, 25]

$$x^7 = \frac{56\Omega a^3 \gamma_s D_s \delta_s t}{kT} \tag{2.19}$$

where Ω is the atomic volume, γ_s the surface energy, D_s the surface diffusivity, δ_s the surface diffusive width and k the Boltzmann's constant. Therefore, surface diffusivity for nanoparticles can be calculated from equation (2.19) if the neck radius and particle radius are measured with time at a given temperature.

Whereas surface diffusion dominates the early stages of low temperature sintering of FCC nanoparticles, the latter stages of sintering are dominated by grain boundary-driven coarsening [62]. The measurement of the dihedral angle, ψ allows us to determine the onset of particle coarsening. At equilibrium, the dihedral angle can be obtained from the following expression:

$$\gamma_{gb} = 2\gamma_s \cos\frac{\psi}{2} \tag{2.20}$$

where γ_{gb} is the grain boundary energy and γ_s is the surface energy. Neck growth is dominant when $\psi < \psi_{eq}$, whereas coarsening due to grain boundary motion is expected to dominate as the equilibrium dihedral angle is approached, which occurs during the latter stages of sintering. For curvature-driven grain boundary motion, the velocity of the grain boundary, v is given by the expression:

$$v = M\left(\frac{\Delta G}{V_m} - \frac{\gamma_{gb} \cdot dA}{V_m}\right) \tag{2.21}$$

where M is the mobility, $\Delta G/V_m$ is the driving force, V_m is the molar volume and ΔG is given by:

$$\Delta G = \frac{2\gamma_{gb} \cdot V_m}{a} \tag{2.22}$$

where γ_{gb} is the grain boundary energy and a is the radius of the nanoparticle. The additional term ($\gamma_{gb} \cdot \mathrm{d}A/V_m$) in equation (2.21) is due to the increase in grain boundary area, dA, as the boundary moves from point A to point B (Figure 2.11). On this basis, equation (2.21) can be rewritten as:

$$v = M\left(\frac{2\gamma_{gb}}{a} - \frac{\gamma_{gb} . dA}{V_m}\right) \tag{2.23}$$

Therefore, from measurements of the boundary velocity and the increase in grain boundary area, the grain boundary mobility, M, which is a measure of the ease with which atoms can transition from one grain to another, can be determined. The boundary velocity can be calculated from the ratio of distance traveled by the boundary to the time taken for the boundary motion. The increase in grain boundary area, dA is calculated from the difference in boundary area assuming a circular boundary. This is a reasonable assumption for spherical particles as the boundary between two spheres is a circle. Thus, dA is given by:

$$dA = \frac{\pi}{4}\left(G_f^2 - G_i^2\right) \tag{2.24}$$

where G_i and G_f are the initial and final grain boundary diameters.

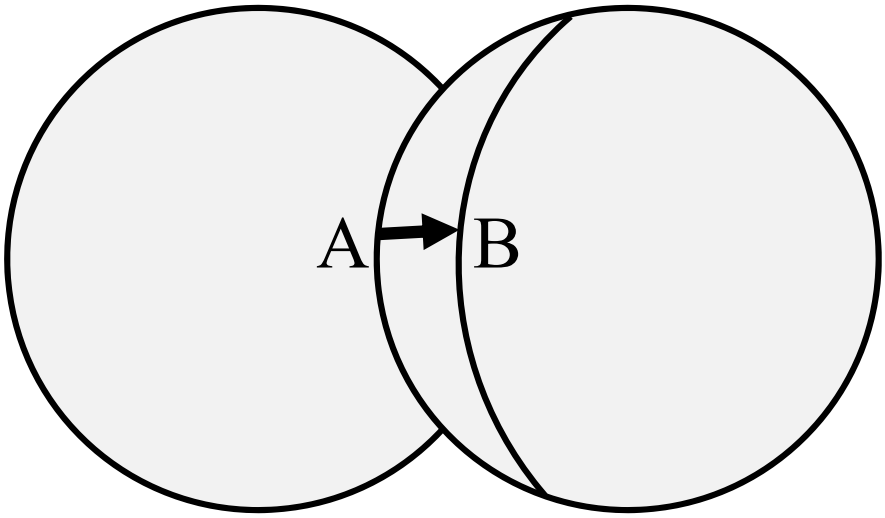

Figure 2.11: Schematic showing curvature-driven boundary motion during the later stages of sintering. Atoms move across the boundary from the particle on the right to the left particle, resulting in a boundary motion from point A to B.

2.7.2 Experimental Study of Nanoparticles Sintering

The sintering models have traditionally been evaluated by comparing with experimental observations of sintering in powder ensembles containing a distribution of particle sizes, obtained by *post-mortem* characterization [50, 63-69]. However, deviations of the experimental observations from the model predictions have spurred much debate on the use of indirect observations to study the sintering process [65, 69]. The use of *in-situ* techniques, which are capable of monitoring dynamic processes in individual

nanoparticles in real time, can help to resolve some of the uncertainties that arise in *post-mortem* experiments. For example, *in-situ* scanning tunneling microscopy (STM) [70-74] and *in-situ* transmission electron microscopy (TEM) [57, 58, 75-83] have been used to monitor the sintering of nanoparticles while heating inside the microscope. However, surface diffusivities and grain boundary mobilities have not been directly measured from sintering experiments. Also, the effects of nanoparticle size, temperature organic capping layer on nanoparticles have not been correlated with neck growth rates during sintering. For this dissertation, the *in-situ* TEM/STEM heating technique is used because of its high resolution capability and its ability to observe grain boundaries and particle orientation, which makes it ideal for studying sintering of small nanoparticles.

2.7.2.1 *In-situ* Transmission Electron Microscopy (TEM) Heating Study of Nanoparticles Sintering

In-situ transmission electron microscopy (TEM) allows us to study the dynamic response of a material to an externally applied stimulus. Thus, the electron microscope can be utilized as a 'nanolaboratory' for carrying out experiments on a small spatial scale. The *in-situ* TEM instrumentation typically requires specially designed specimen stages for performing experiments such as heating, cooling, electrical probing, straining, or indentation of the specimen. Due to recent advancements in miniaturization techniques, specimen stages small enough to fit into the narrow gap of the objective pole pieces are now commercially available for high resolution microscopy [84].

In-situ transmission electron microscopy (TEM) heating is a powerful tool for studying temperature effects on nanomaterials. During *in-situ* TEM heating experiments, the specimen temperature is varied by resistive heating of the holder, as shown schematically in Figure 2.12. Modern heating stages allow imaging with lattice resolution at specimen temperatures up to 1200 °C and can be used for direct observation of the dynamics of reactions such as phase transformations (solid-solid, solid-liquid and solid-gas), morphological changes, crystal growth etc. [85, 86]. *In-situ* microscopy studies of thermal effects is particularly interesting in nanomaterials because macroscopic characterization tools do not provide the information needed for understanding morphological changes and phase transformations in small particles, which have dimensions that are only accessible by techniques of high resolution microscopy. With *in-situ* TEM heating, the sintering process can be observed on the atomic scale in real-time.

Previous *in-situ* TEM heating experiments used a miniature furnace with a heating coil to indirectly heat the sample, while temperature measurements were done with an attached thermocouple. This results in substantial thermal drift during heating, making it difficult to perform these experiments at high magnifications needed to observe small nanoparticles. In addition, these heating stages takes several minutes to ramp up the heater to desired temperatures, during which some of the sintering process might have already occurred. Also, some sintering experiments have been done by heating the sample with a focused electron beam in the TEM, and the temperatures were estimated from the beam current density and irradiation time. The problem with this is that the

sintering temperatures cannot be accurately determined in these experiments. To address the aforementioned issues, we use a novel Aduro^{TM} heating stage which provides very stable heating operation with minimal thermal drift for high resolution imaging.

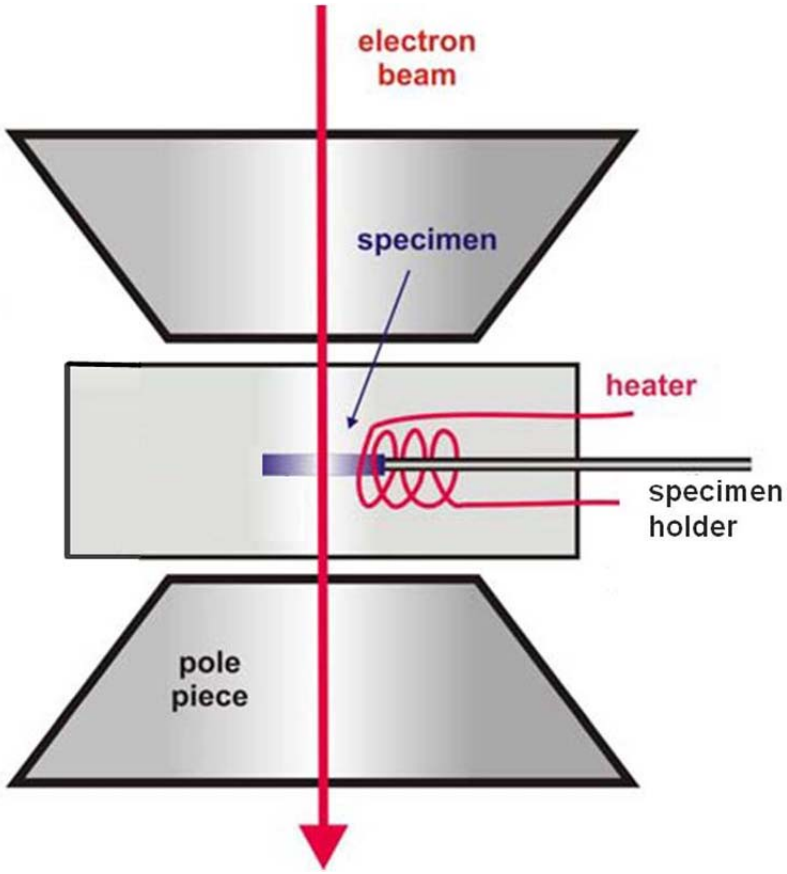

Figure 2.12: Schematic of *in-situ* transmission electron microscopy (TEM) heating [84].

Chapter 3: Experimental Procedure

3.1 Materials and TEM Sample Preparation

Four different sets of samples were used for the *in-situ* TEM/STEM heating experiments, using two different materials. Silver nanoparticles with nominal sizes of 15 nm and 40 nm were obtained from Nanotechnologies Inc. The nanoparticles were synthesized by a pulsed plasma dry synthesis method (Figure 3.1) and a carbon additive was added during the manufacturing process to prevent agglomeration of the nanoparticles by physically separating them. Platinum nanoparticles with nominal sizes of 2 nm and 6 nm on strongly adhering carbon (Ketjen) support, obtained from Johnson Matthey Technology Centre (JMTC) and platinum nanoparticles with a nominal size of 2.8 nm on weakly adhering carbon (Vulcan) support, from Tanaka Kikinzoku Kogyo (TKK) were also used. For TEM observation, the as-received nanoparticles were first dispersed in ethanol and placed in an ultrasonic bath for ten minutes to reduce particle agglomeration. The nanoparticles in solution were then deposited onto an Aduro^{TM} heater chip which was later placed in a Protochips heating holder for *in-situ* TEM experiments. In addition, silver nanoparticles produced by a novel laser ablation of microparticle aerosol (LAMA) technique [87] were also used (Figure 3.2). The nanoparticles were collected directly on the Aduro^{TM} heater chip, in order to study the intrinsic sintering behavior of nanoparticles without any carbon surface coatings or other additives. Lastly, some samples were prepared where the LAMA-produced nanoparticles were deposited onto a bare silver wire in order to minimize the presence of carbon on the sample.

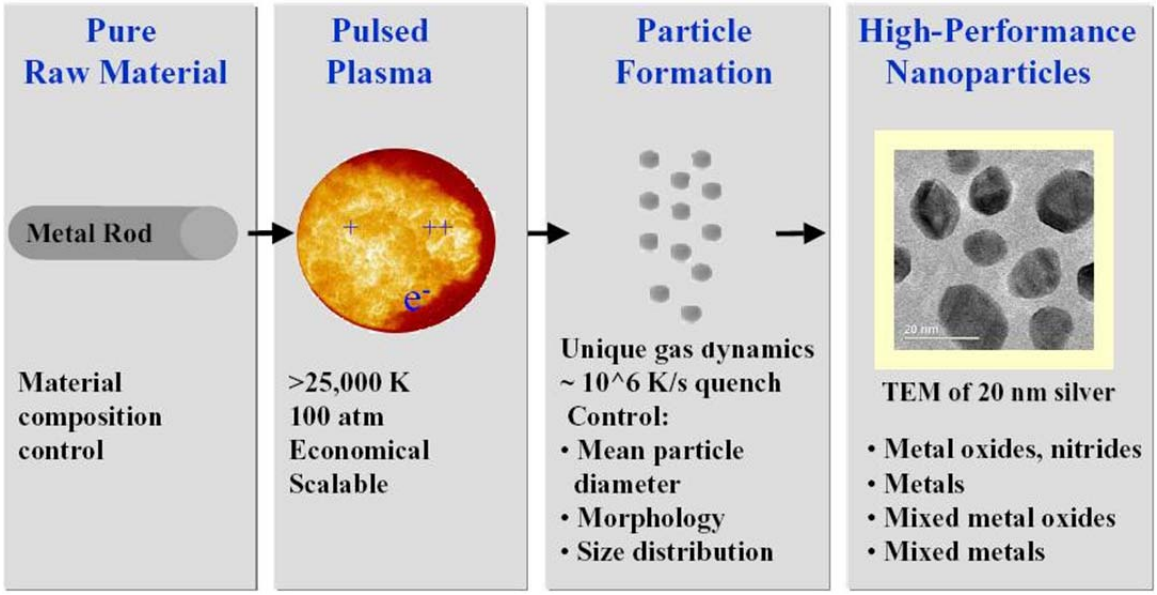

Figure 3.1: Synthesis of silver nanoparticles by the pulsed plasma dry synthesis method (courtesy of Nanotechnologies Inc.).

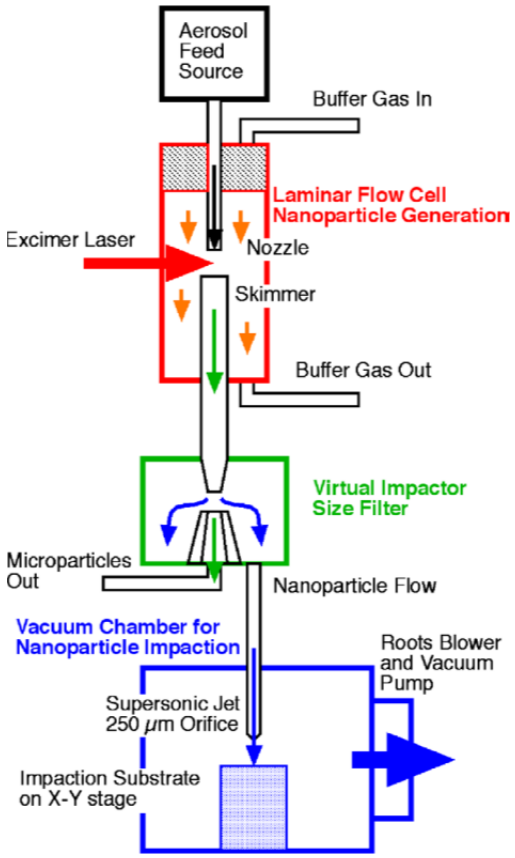

Figure 3.2: Schematic of the laser ablation of microparticle aerosol (LAMA) process [87].

3.2 *In-situ* TEM/STEM heating

In-situ heating experiments were performed in both conventional bright field (BF) transmission electron microscopy (TEM) mode using phase contrast imaging and in high angle annular dark field (HAADF) scanning transmission electron microscopy (STEM) mode using Z-contrast imaging. The TEM experiments were performed in a JEOL 2010F TEM while the STEM experiments were carried out in a state-of-the-art aberration-corrected JEOL 2200FS STEM/TEM microscope located at Oak Ridge National

Laboratory's High Temperature Materials Laboratory or the JEOL JEM-ARM 200F Atomic Resolution Analytical Microscope at The University of Texas at San Antonio's Advanced Microscopy Laboratory. The aberration-corrected HAADF STEM capability is ideal for imaging very small nanoparticles, atomic clusters and even single atoms supported on a carbon substrate, which are not observable in a conventional TEM due to poor contrast from the carbon support. The recorded high angle annular dark field (HAADF) or "Z-contrast" images show a pure mass-thickness contrast and zero diffraction contrast, which is a powerful technique for observing the coalescence process, particularly the development of the neck region due to variations in thickness in that region.

The TEM experiments were performed on nanoparticles with diameters greater than 5 nm (silver nanoparticles from Nanotechnologies Inc., silver nanoparticles from LAMA, and 6 nm platinum nanoparticles from JMTC) while the STEM experiments were performed on nanoparticles with diameters less than 5 nm (platinum nanoparticles from TKK and 2 nm platinum nanoparticles from JMTC).

The nanoparticles were heated *in-situ* using a novel Aduro^{TM} heating stage [88] (Protochips Inc., Raleigh, NC). The heating stage uses a disposable micro-electro-mechanical system (MEMS) device that serves both as the heating element and the specimen support grid and the holder have electrical feed-throughs that connect to an external power supply (Figure 3.3a). The MEMS device is a 150 nm thick, 500 μm × 500 μm, free standing membrane made from a conductive ceramic material that is suspended on a 4 mm × 6 mm silicon chip. For electron transparency, the ceramic membrane is

patterned with a series of 6 μm diameter holes, which are subsequently overlaid with a holey carbon film, which support the nanoparticles (Figures 3.3b and 3.3c). Joule heating occurs when electrical current is forced through the ceramic membrane and the current is used to control the temperature. The current versus temperature response of the heating device was calibrated at the factory using an imaging pyrometer in a vacuum probe station (at a pressure similar to what is used in a TEM column). This heating stage enables very fast heating rates (10^6 °C/s) with an extremely low thermal drift even at high temperatures due to its low thermal mass, unlike conventional heating holders. This allows for isothermal experiments to be carried out in the TEM as desired temperatures can be achieved nearly instantaneously.

The *in-situ* heating experiments were performed on silver and platinum nanoparticles with diameters ranging from 2 - 40 nm and temperatures from 25 - 500 °C in order to investigate the effects of size and temperature on sintering of nanoparticles. The size and temperatures for each experiment were chosen such that the sintering process can be observed *in-situ* in the microscope within a reasonable time frame.

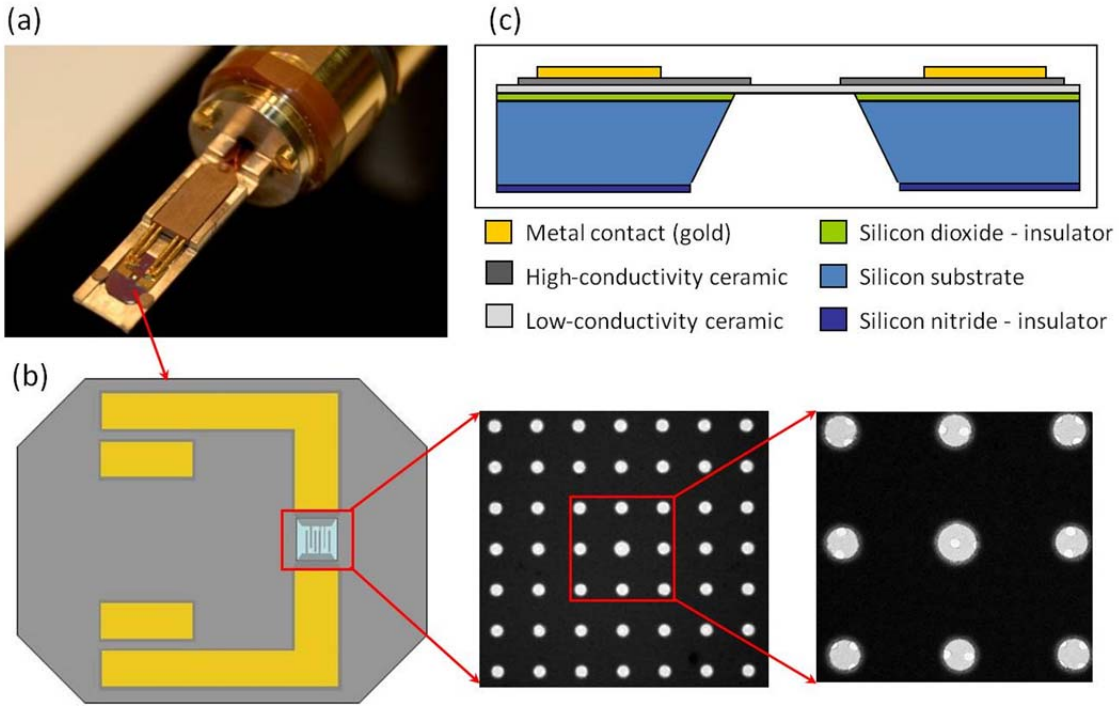

Figure 3.3: (a) Tip of Protochips specimen holder showing heater chip clamped into place, with electrical leads connected. (b) Top view schematic of Protochips heater chip. The insets are low magnification TEM images of the central region of the chip showing the pattern of holes in the low-conductivity ceramic membrane and holey carbon support film overlaying the holes in the ceramic membrane. (c) Cross-section view of chip (courtesy of Protochips Inc.).

3.3 Temperature Calibration of Heater Chips

The as-received heater chips were further checked for accuracy in our laboratory using a known solid-to-vapor phase transformation to determine their accuracy for temperature measurements. The sublimation of silver nanoparticles using *in-situ* TEM

heating has been studied previously [30, 89, 90] and was shown to be a powerful method for measuring temperature in a TEM. Sambles *et al.* [30] derived a model, based on the Kelvin equation [31], to predict the time, t it takes for a nanoparticle of a given radius, r to transform from solid to vapor at a given temperature, given by the following expression:

$$t = \frac{B}{A}\left\{E_0\left(\frac{B}{r}\right) - E_1\left(\frac{B}{r}\right)\right\} \tag{3.1}$$

with the constants A, B, $E_0(x)$ and $E_1(x)$ defined as:

$$A = \alpha\left(\frac{M_r}{2\pi R\rho^2}\right)^{1/2}\frac{P_\infty}{T^{1/2}} \tag{3.2}$$

$$B = \frac{2M_r\gamma}{\rho RT} \tag{3.3}$$

$$E_0(x) = \frac{exp(-x)}{x} \tag{3.4}$$

$$E_1(x) = \int_x^\infty \frac{exp(-y)}{y}dy \tag{3.5}$$

where M_r is molecular weight, R is gas constant, ρ is density, T is the temperature, P_∞ is equilibrium vapor pressure of the sublimating species over a flat surface, γ is the surface energy.

They also performed *in-situ* TEM heating experiments on silver nanoparticles by measuring the change in particle radius with time at a fixed temperature and confirmed the model for particles as small as approximately 20 nm (the resolution limit of their equipment). Because the sublimation rate is highly sensitive to temperature, this method can serve as an excellent calibration tool.

To determine if this experiment could be used to calibrate temperature at low temperatures and using smaller nanoparticles, we performed a series of experiments that are shown in Figure 3.4 as a sequence of TEM images from an *in-situ* heating experiment. The figure shows the sublimation of a 20 nm diameter silver nanoparticle over a period of 15 minutes. The sublimation process starts on the surface of the nanoparticles and continues gradually until the entire nanoparticle vaporizes. The TEM images also show some distinct facets forming on the surface during sublimation, as the nanoparticles continue to shrink in size. The FFTs of the images in Figure 3.4, shows that the facets form typically on low index {100} and {111} planes.

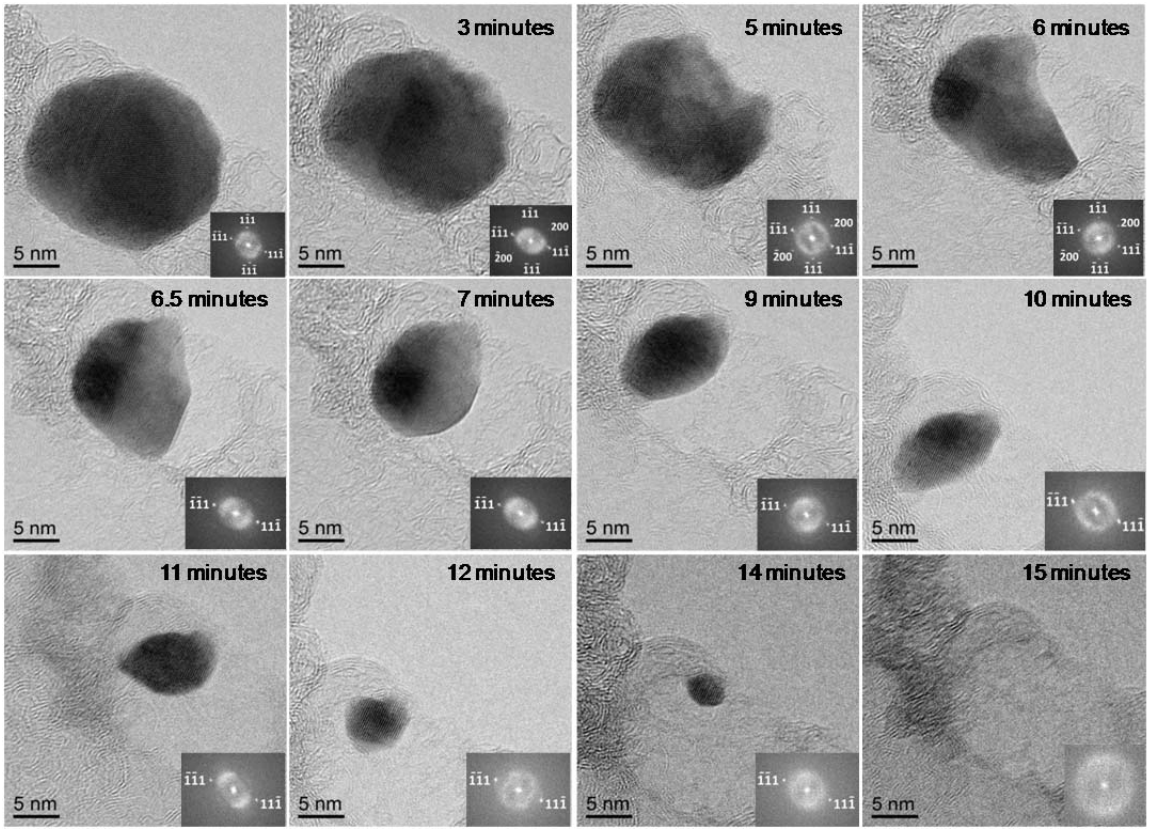

Figure 3.4: Sequence of TEM images during isothermal experiment at 580 °C, showing sublimation of a 20 nm silver nanoparticle. The insets are the fast Fourier transforms (FFTs) of the TEM images.

The actual temperature of a nanoparticle can thus be determined by monitoring the kinetics of the sublimation of a nanoparticle at a particular temperature and measuring the change of particle radius with time, as described by Sambles *et al.* [30]. Figure 3.5 shows a plot of particle radius with time from an isothermal experiment on a 28 nm nanoparticle at 600 °C and the plot is compared to theoretical predictions for particles of the same size and at the same temperature. The plot shows that there is a discrepancy

between the experimentally determined rate of sublimation and that predicted from theory. Examination of the theoretical predictions and the experimental data shows that the discrepancy most likely results from a difference between the apparent sample temperature and actual temperature because this is the only parameter where variations are consistent with the observed curvature in particle radius versus time. Figure 3.5 shows that if the apparent temperature was 58 °C cooler than that temperature determined from our sublimation experiments, there is a good match between the experiments and theory.

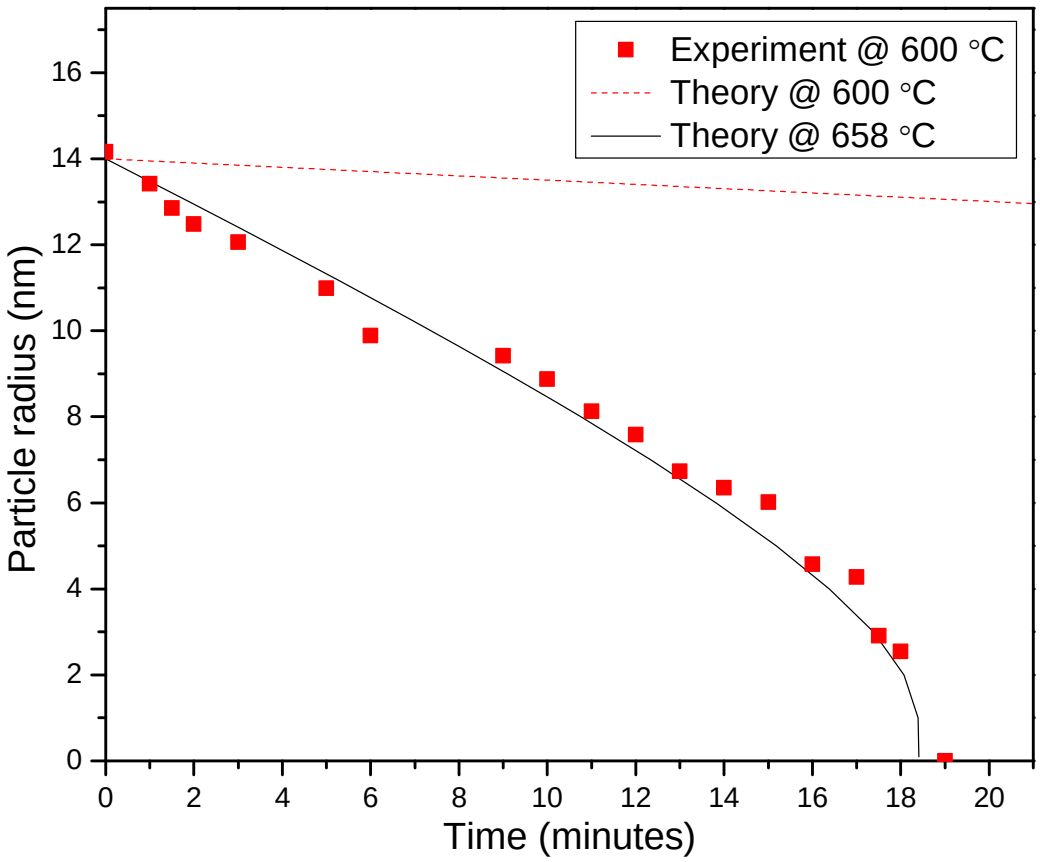

Figure 3.5: Plot of particle radius versus time during an isothermal heating experiment on a 28 nm nanoparticle for an experiment at a nominal temperature of 600 °C, based on the calibrated value for this device. The dashed and solid lines are obtained from theoretical predictions of the sublimation rate at 600 °C and 658 °C, respectively. These results suggest that the effective temperature with the TEM beam on is about 58 ˚C hotter than indicated by the heating stage.

The calibrated temperatures of the heating stage only account for resistive heating of the specimen holder from the power supply so any heating from the electron beam is not accounted for. Calculations by Hobbs [91] suggest that for thin film specimens of metals and other good conductors, beam heating is negligible under standard TEM conditions. However, Gryaznov *et al.* [92] have shown that the average temperature of nanoparticles under electron beam irradiation in the TEM can increase by several hundred degrees, depending on contact conditions with the substrate, the intensity of the beam and size of the nanoparticles. This larger temperature increases can arise because the dimensions of the contact area with the substrate are usually smaller than the nanoparticle radius, so heat flux through the contact is impeded, leading to a larger average temperature in the nanoparticle compared to the substrate. For a given beam current density, the temperature increase on the nanoparticle was shown to be proportional to the square of the particle radius. The total beam current under typical operating conditions in our microscope was measured with a Faraday cup holder as 4.565 nA and the current density was determined to be about 1.6×10^3 A/m^2. Using the model of Gryaznov *et al*., this corresponds to a predicted temperature increase from beam heating of about 96 °C for a 28 nm nanoparticle, assuming a small contact angle of about 3° (Figure 3.6), which is slightly higher than our measured temperature difference of 58 °C. However, this calculation can only be used as a guide because the predicted and actual rate of heat dissipation depends strongly on the contact area between the particle and substrate. In practice this contact area cannot be easily determined and varies from particle-to-particle since it depends on the contact geometry between the particle and

substrate. The actual amount of beam heating will decrease with an increase in the contact angle or decrease in the current density.

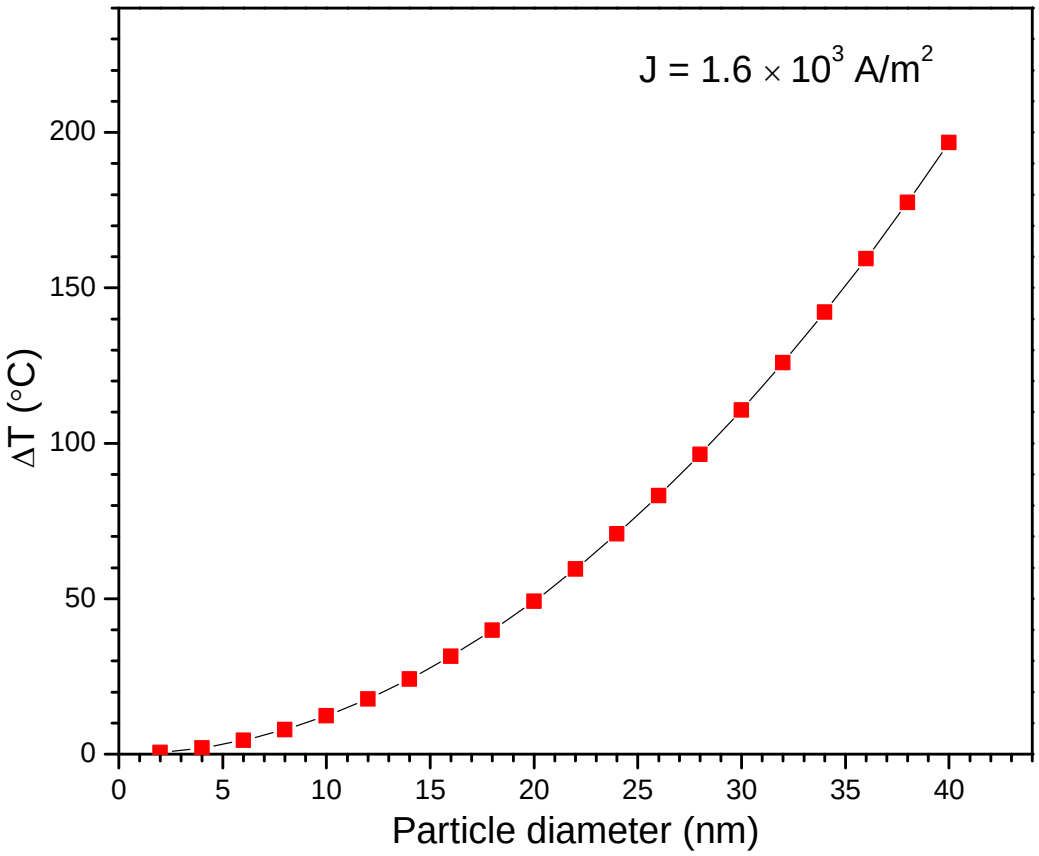

Figure 3.6: Size dependence of the temperature increase on a nanoparticle due to electron beam heating.

By comparing the change of particle radius with time from several *in-situ* TEM heating experiments with theory, we confirm that the temperature difference between theory and experiments can vary from particle-to-particle. For example we find that the temperature discrepancy for a 35 nm nanoparticle can range from about 20 °C to 150 °C

(Figure 3.7), which agrees well with the theoretical predictions from Gryaznov *et al.* of about 150 °C (Figure 3.6). Also, we see a better match between the measured and theoretical sublimation temperatures when the electron beam is on for a small fraction of the annealing time (less than ~ 20%) compared to when the beam is on all the time. These experiments show that for nanoparticles, electron beam heating contributes to the actual temperature rise experienced by the nanoparticles and is likely a major cause of the discrepancy between the observed and apparent temperatures during *in situ* TEM experiments. It is also possible that there may be additional errors in the calibration of the TEM specimen holders themselves since this calibration is performed independently of other measurements. Additional heating experiments were performed on silicon nitride-coated grids to determine if there were differences compared to the standard carbon-coated grids. However, our results were similar to those obtained with the carbon-coated grids. In conclusion, our sublimation experiments show that the overall accuracy of the measurements of temperature using the Protochips holder due to these combined effects and during realistic conditions for measurement is between 20 °C - 150 °C.

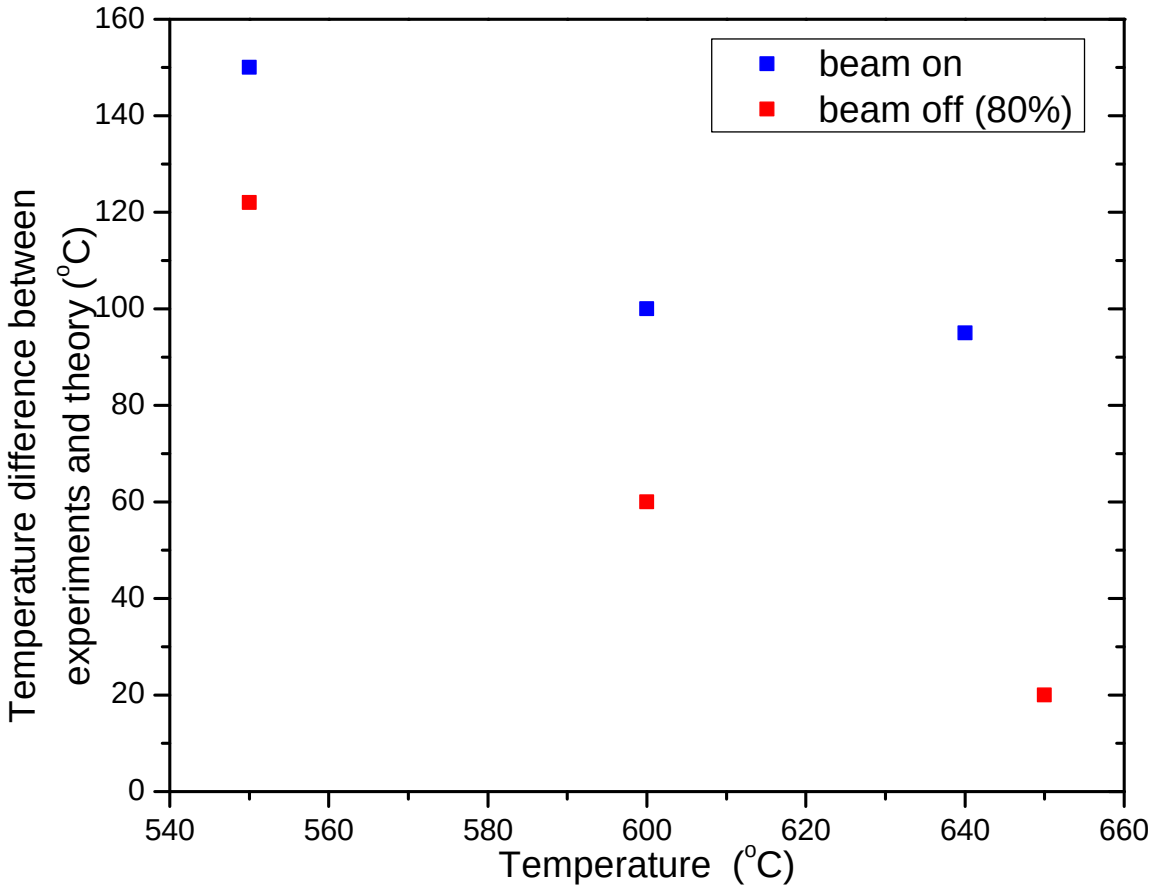

Figure 3.7: Plot of temperature difference between experiment and theory as a function of temperature during *in-situ* TEM heating of a 35 nm silver nanoparticle, with electron beam on all through and electron beam off for about 80% of the duration of the heating experiment.

3.4 Determination of Sintering Parameters

The measurements of the particle geometry relevant to coalescence and sintering such as particle radius, neck radius, dihedral angle and grain boundary motion were performed using DigitalMicrograph™ software (Version 1.71.38, Gatan Inc. Pleasanton,

CA). For the measurements, we selected nanoparticles that were nearly spherical (i.e. the major and minor axes were within 5% of each other), so that the two-particle sintering model could be used. To measure the particle radius (a), the software is first used to clearly detect the edges of the nanoparticles in the TEM images. Subsequently, a circle was fitted to each nanoparticle (see section 4.3) using a Matlab® program (Appendix A) [93] that computes a least-square fit of a circle for a set of (x, y) coordinates selected on the edges of the nanoparticle. The area of the fitted circle is then used to obtain an equivalent particle radius for a spherical nanoparticle. The neck radius, x was calculated as one-half the length of the line drawn perpendicular to the intersection of the two particles. The dihedral angle, ψ was obtained by measuring the angle between the grain boundary and the tangents to the surface of the nanoparticles in the neck region. When the grain boundary begins to move, the increase in grain boundary area, dA is calculated from the initial and final boundary diameters, assuming a circular boundary and the grain boundary velocity, v is obtained from the ratio of the distance moved by the grain boundary to the time it takes for the motion. The largest error is in the measurement of particle radius, which is estimated to be approximately 5%. This error results from fitting a circle to the projections of the nanoparticles that may not be perfectly spherical.

Chapter 4: Experimental Results

4.1 Sintering of Silver Nanoparticles

Effect of Size on Sintering of Mono-size Nanoparticles

First, to determine the effect of particle size on sintering, *in-situ* TEM heating experiments were conducted on different nanoparticles of the same size held at the same temperature. Figure 4.1 shows a sequence of TEM images for two 40 nm silver nanoparticles sintering at 400 °C. The two nanoparticles, initially in contact, form a neck and sintering occurs by rapid growth of the neck region after 3 minutes. The neck growth then slows down as the nanoparticles are monitored over a period of 15 minutes. Note that there is clearly some carbon present on the surface of the nanoparticles (added during synthesis) that is most apparent in the first frame (see arrows in image) but is difficult to resolve completely at this magnification in the other frames. Some bright and dark contrast changes are also apparent in the nanoparticles from frame-to-frame; for example, the particle on the left which is initially bright at 0 minute appears dark after 3 minutes and then changes to bright after 8 minutes. This type of contrast changes can be due to relative rotation of the nanoparticles or movement of the carbon support. However, it is highly unlikely that the contrast changes are due to motion of the relatively flat carbon substrates, which suggests that the nanoparticles undergo some rotation during sintering. In addition, we see an unusual bright contrast around the edges of the nanoparticle on the left. This type of contrast may be due to the presence of a liquid phase on the surface or slight variations in thickness around the edge of the sample. However, it is very unlikely

that the contrast is due to surface melting because the sintering temperature here is lower than the melting temperature of silver, even if melting point depression due to particle size effects is considered.

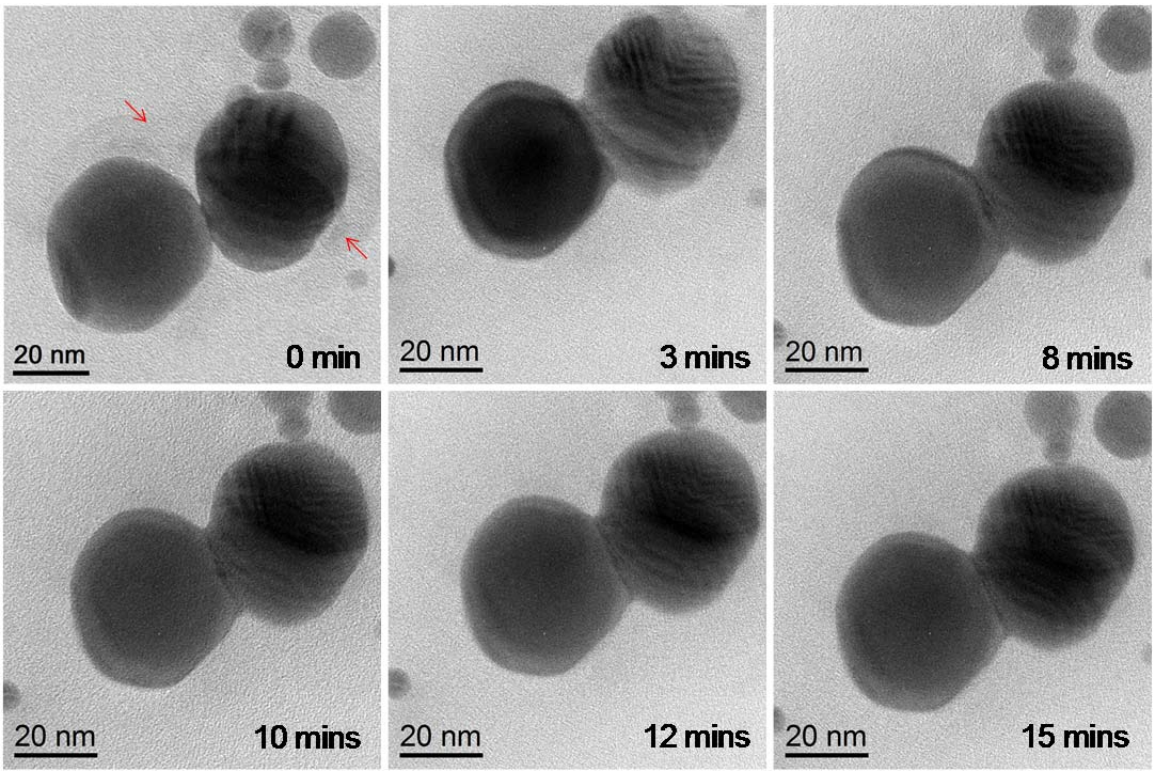

Figure 4.1: A sequence of *in-situ* TEM heating images showing sintering of two 40 nm silver nanoparticles at 400 °C. The arrows in the first frame indicate the carbon present on the surface of the nanoparticles.

A sequence of *in-situ* TEM images showing sintering of two 15 nm nanoparticles at 400 °C are shown in Figure 4.2. These nanoparticles made from the LAMA process are deposited directly onto a carbon support. We expect the nanoparticles to be free of carbon

coating due to the manner in which they were produced. However, since the nanoparticles are sitting on a carbon substrate, it is difficult to clearly distinguish between the carbon support and any adsorbed hydrocarbons that may be present on the surface from atmospheric contamination. It is also possible that carbon from the support can be deposited on the nanoparticle surface during impaction of the nanoparticles on the substrate. The nanoparticles sinter by first making contact followed by rapid neck growth after 4 minutes. The mechanism for initial contact of the nanoparticles is not clear from these images but three possible mechanisms include: 1) movement of the nanoparticles on the substrate until they make contact 2) mass transfer from small clusters on the support towards the neck region, which then forms a bridge between the nanoparticles 3) a van der Waals attraction between the nanoparticles, which can cause them to make contact if they are close enough. It is difficult to specifically say which mechanism is in operation from this experiment but it is expected that one or all of these mechanisms can initiate particle contact, as discussed later. Comparing the images taken after 3 minutes in Figures 4.1 and 4.2, the ratio of the neck radius to particle size for the 15 nm nanoparticles (~ 0.5) is slightly higher than that for the 40 nm nanoparticles (~ 0.45), which suggest that sintering tends to occur faster for smaller size nanoparticles. This is expected because the smaller nanoparticles have a larger driving force (curvature) and shorter diffusion distances and should therefore sinter faster than the larger ones at the same temperature.

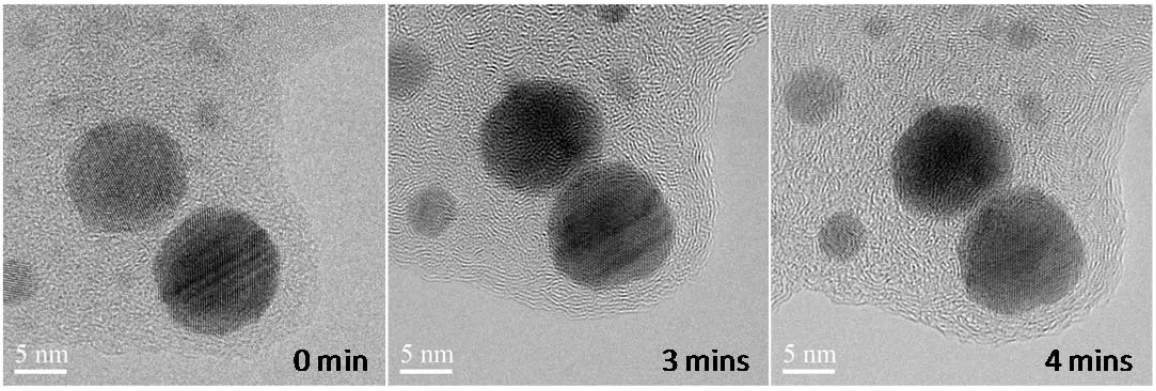

Figure 4.2: A sequence of *in-situ* TEM heating images showing sintering of two 15 nm LAMA-produced silver nanoparticles at 400 °C.

Effect of Temperature on Sintering of Mono-size Nanoparticles

Secondly, to determine the effect of temperature on sintering, *in-situ* TEM heating experiments were conducted on nanoparticles of the same size at different temperatures. *In-situ* TEM heating images showing sintering of two 15 nm silver nanoparticles at 300 °C are shown in Figure 4.3. Here we see that the two nanoparticles are initially not in contact but eventually do make contact after some time, and we see a development of the neck region after about 4 minutes. From Figure 4.2 and 4.3, the ratio of the neck radius to particle size after 4 minutes at 300 °C (~ 0.3) is lower than that at 400 °C (~ 0.5) for the same size nanoparticles, which shows that neck growth occurs slower at lower temperatures. This is expected since sintering, as a thermally activated process, will occur faster at higher temperatures for same size particles.

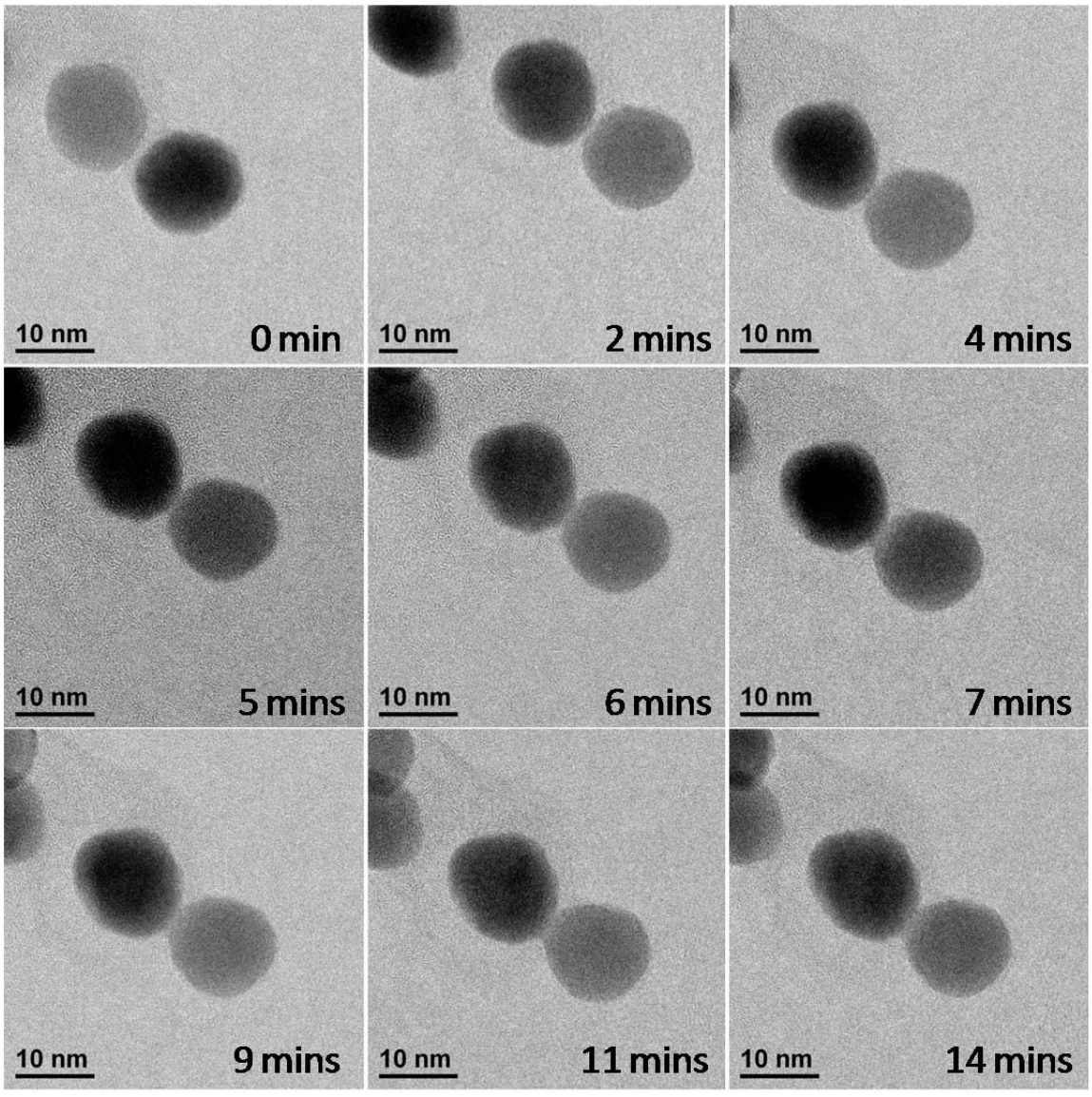

Figure 4.3: A sequence of *in-situ* TEM heating images showing sintering of two 15 nm silver nanoparticles at 300 °C.

Another sequence of *in-situ* TEM images from a heating experiment on two 15 nm silver nanoparticles at 200 °C is shown in Figure 4.4. In this case, contact between the nanoparticles is initiated by a third particle and sintering occurs by rapid neck growth

afterwards, as seen in the image taken at two minutes. The nanoparticles are monitored for about 30 minutes and we see that the neck grows until the dihedral angle approaches the equilibrium value, after approximately 15 minutes. For silver, γ_{gb}/γ_s = 0.33 [94], which gives ψ_{eq} = 161° from equation (2.20). The boundary region between the particles then begins to move afterwards. The smaller nanoparticle at the bottom of the frame appears to move towards the two nanoparticles sintering in the middle of the frame and eventually coalesces with the larger nanoparticles after some time. This suggests that either there is some mobility of the nanoparticles on the carbon or that mass transfer is occurring between particles by diffusion of atoms or small clusters of atoms that are below the resolution of these micrographs. We also observe some contrast changes in the nanoparticles from frame-to-frame, which is consistent with our previous observations in other samples. The FFTs taken from the particle on the left (Figure 4.5), shows that the diffraction spots changes from frame-to-frame, suggesting particle rotation during sintering. For example the particle goes from a near two beam condition at 4 minutes to a near zone axis condition at 7 minutes, and similar changes are observed with time. Such rotations are typically within a few degrees since we are always in the same zone axis. In addition, there are twin defects in the nanoparticles, as seen from the multiple spots in the FFT of the image taken at 30 minutes (Figure 4.6 (a)) and inverse FFT of the selected twin spots (Figures 4.6 (b)), but it is unclear how these defects might affect the sintering behavior of nanoparticles. This can be explored further in the future by performing sintering experiments on nanoparticles with a range of defect densities.

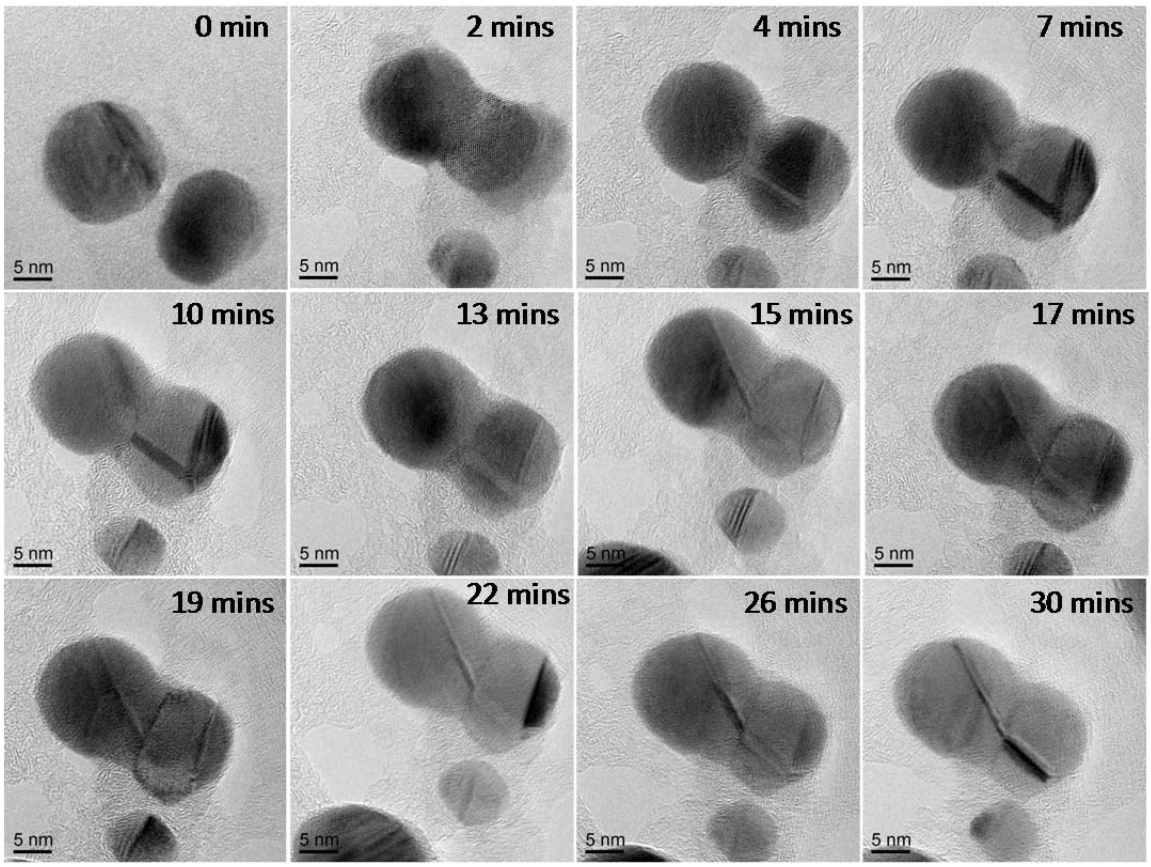

Figure 4.4: A sequence of *in-situ* TEM heating images showing sintering of two 15 nm silver nanoparticles at 200 °C.

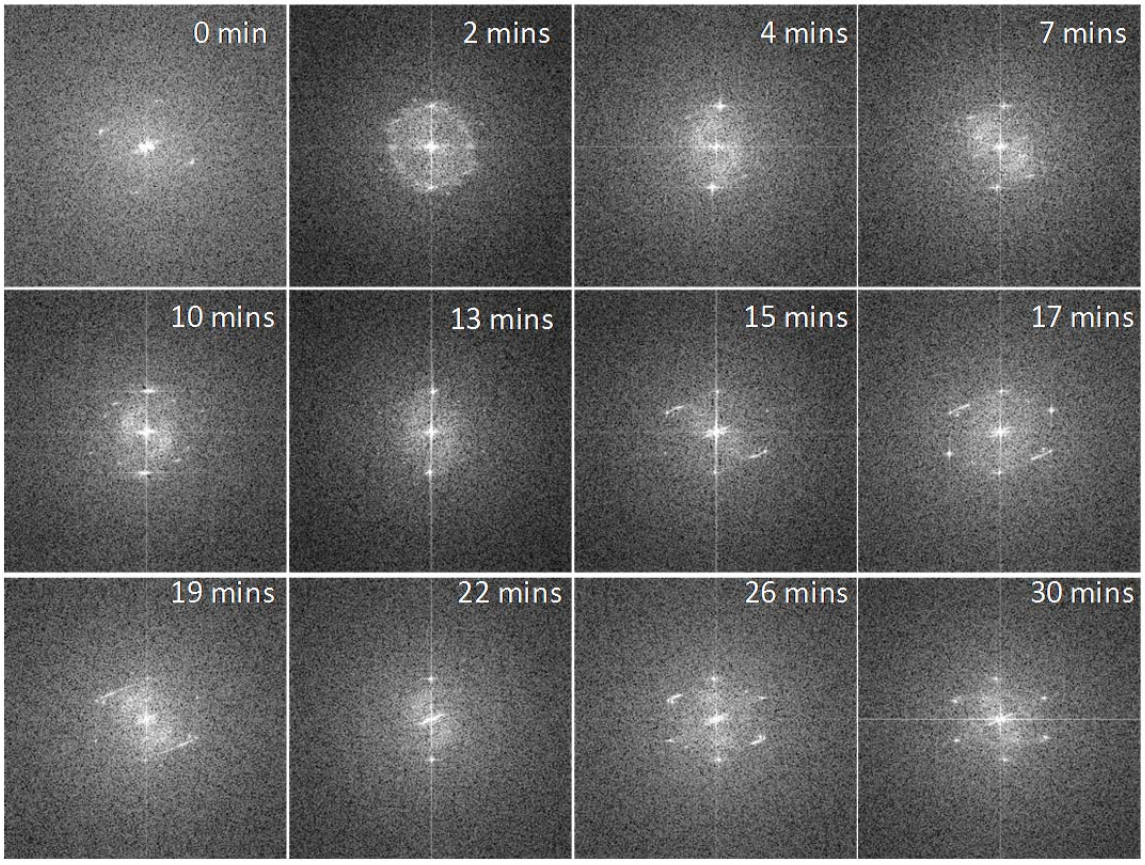

Figure 4.5: A sequence of FFTs taken from the nanoparticle on the left in Figure 4.4, showing that the diffraction spots changes from frame to frame, indicating particle rotations of a few degrees occur during sintering.

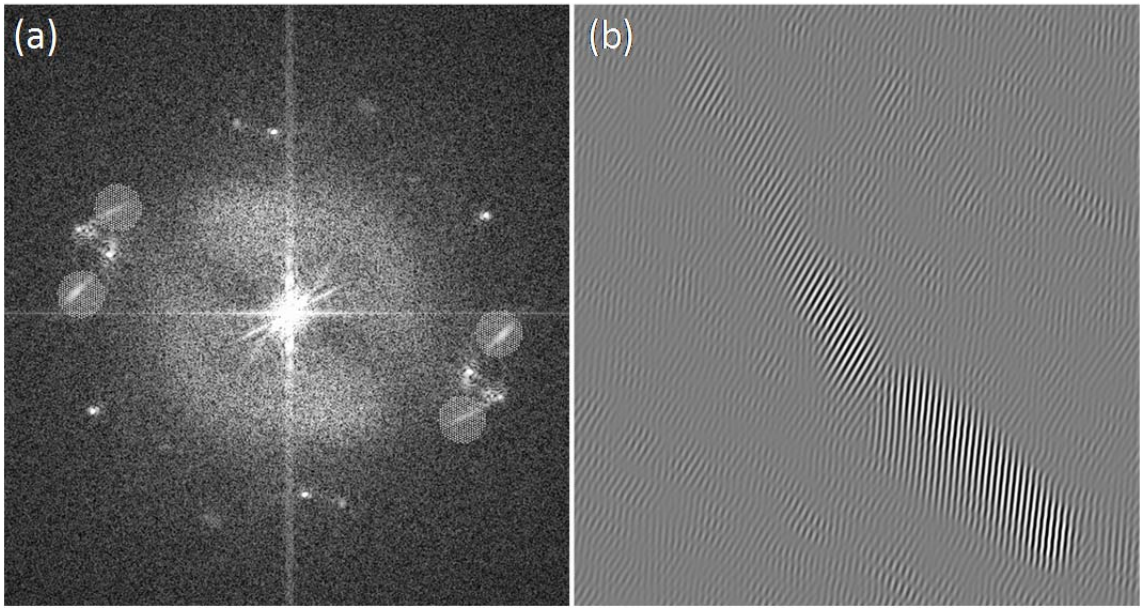

Figure 4.6: (a) FFT of the image in Figure 4.4 at 30 minutes, with multiple spots confirming the presence of twin defects in the nanoparticles. (b) Inverse FFT of the selected diffraction spots in (a), clearly shows that the spots are from the twin defects in the nanoparticles.

Sintering of Non-uniform Sized Particles

Thirdly, *in-situ* TEM heating experiments were conducted on nanoparticles with different sizes at different temperatures to determine sintering mechanisms in systems with non-uniform sized particles. Figure 4.7 shows sintering of 15 nm and 20 nm nanoparticles at 100 °C. The nanoparticles are monitored for about 11 minutes and here we see similar contrast changes in the nanoparticles as before. The growth of the neck seems to be aided by the presence of some silver material in the neck region (indicated with the arrow in the first frame) which contributes to matter transport to the neck.

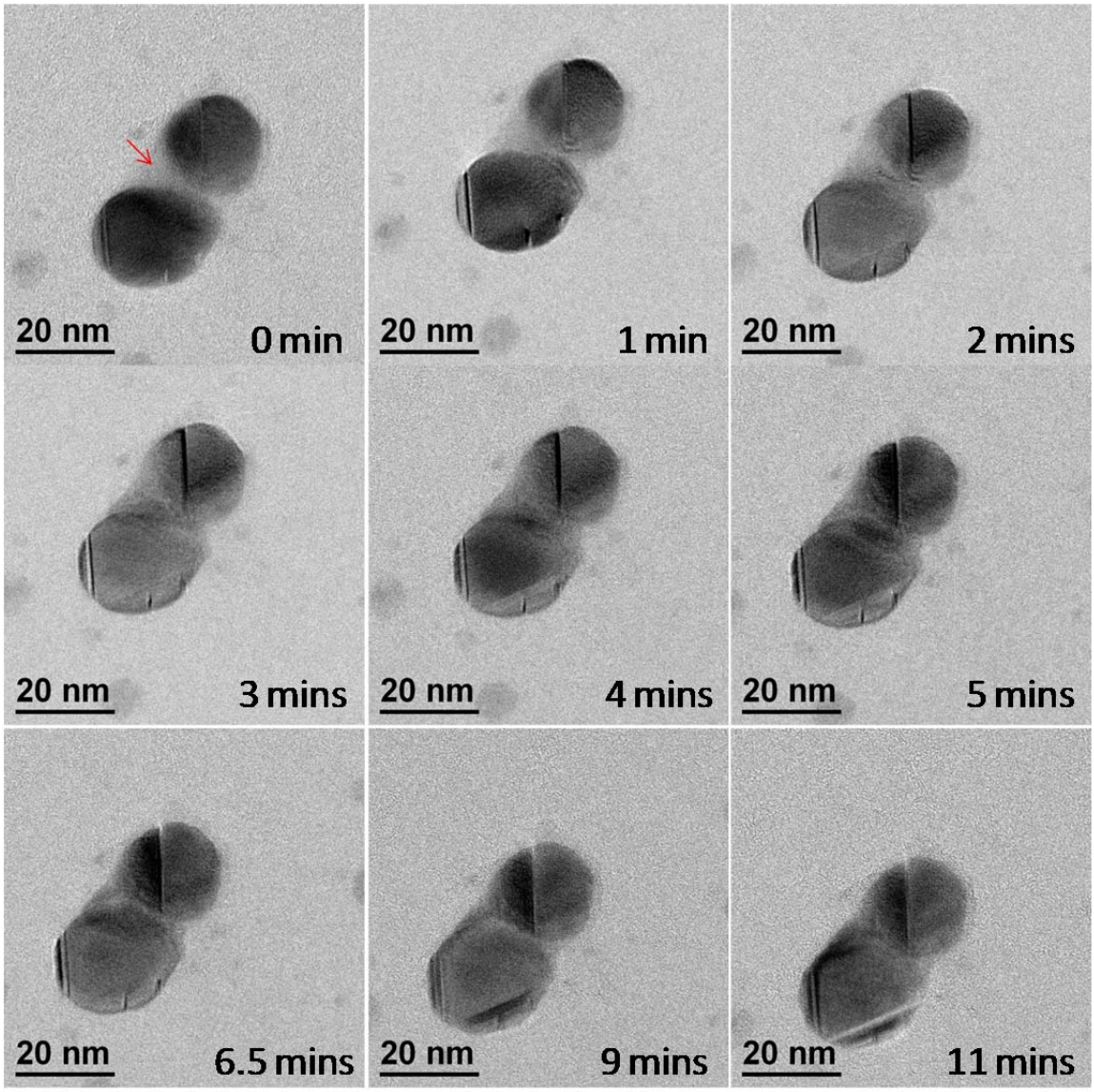

Figure 4.7: A sequence of *in-situ* TEM heating images showing sintering of 15 nm and 20 nm LAMA silver nanoparticles at 100 °C.

A sequence of *in-situ* TEM images showing sintering of 15 nm and 18 nm nanoparticles at 200 °C is shown in Figure 4.8. Here we see that, sintering occurs by a

neck growth process after the particles come in contact, similar to that observed for sintering of mono-size nanoparticles.

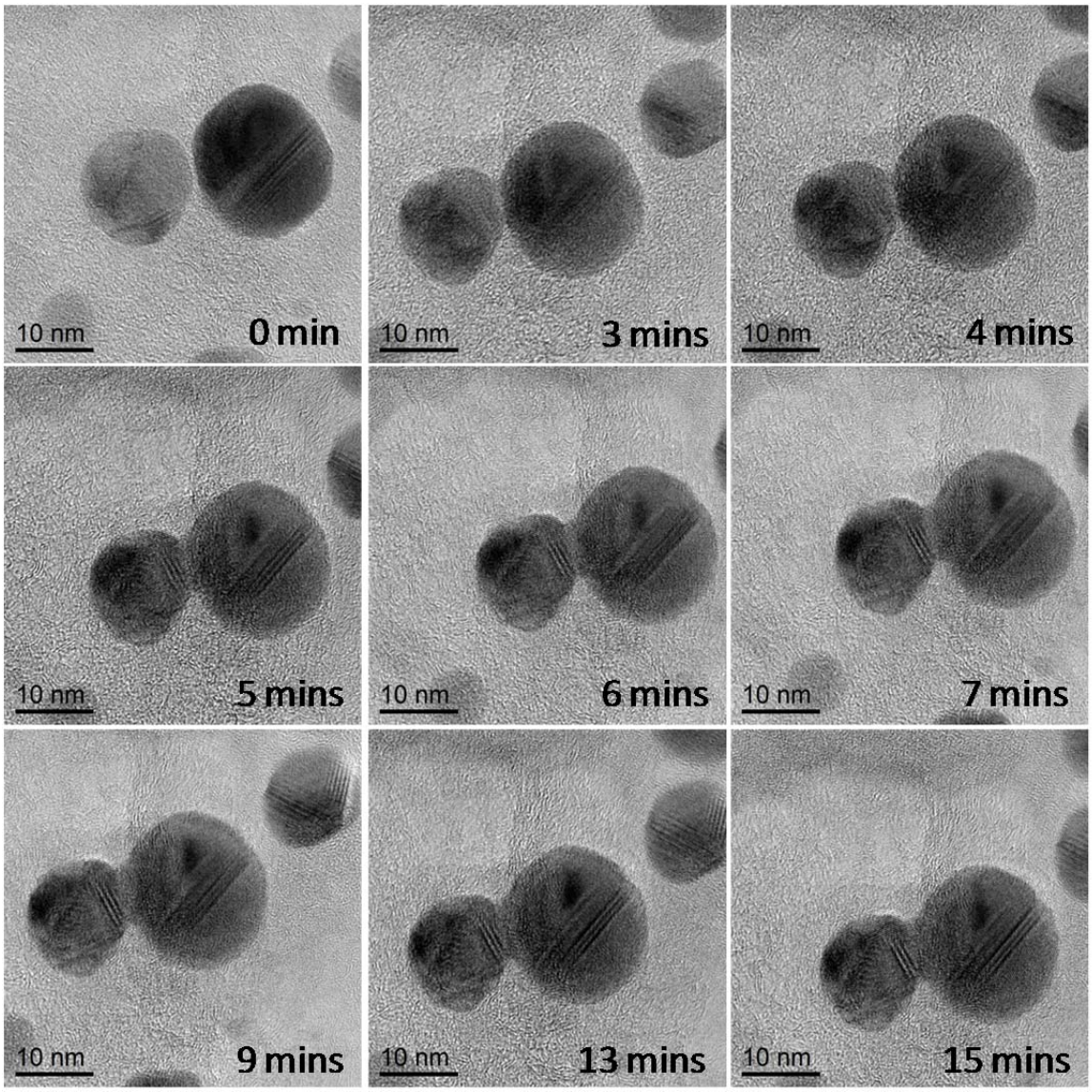

Figure 4.8: A sequence of *in-situ* TEM heating images showing sintering of 15 nm and 18 nm silver nanoparticles placed on a carbon support and heated at 200 °C.

Two of the images taken during *in-situ* TEM heating and obtained at the beginning and end of a video sequence taken to monitor the sintering of 15 nm and 10 nm nanoparticles at 400 °C are shown in Figure 4.9. There are only two images in this sequence because the software used for acquiring TEM images and recording videos does not allow simultaneous video recording and image capture. However, frames can be obtained from the video, though with a poorer resolution because of the reduced bin size used for video capture. These images confirm that a neck developed between the particles at the beginning of the heating experiment grows with time. These results show that similar sintering mechanisms operate in mono-size and non-uniform two nanoparticle systems.

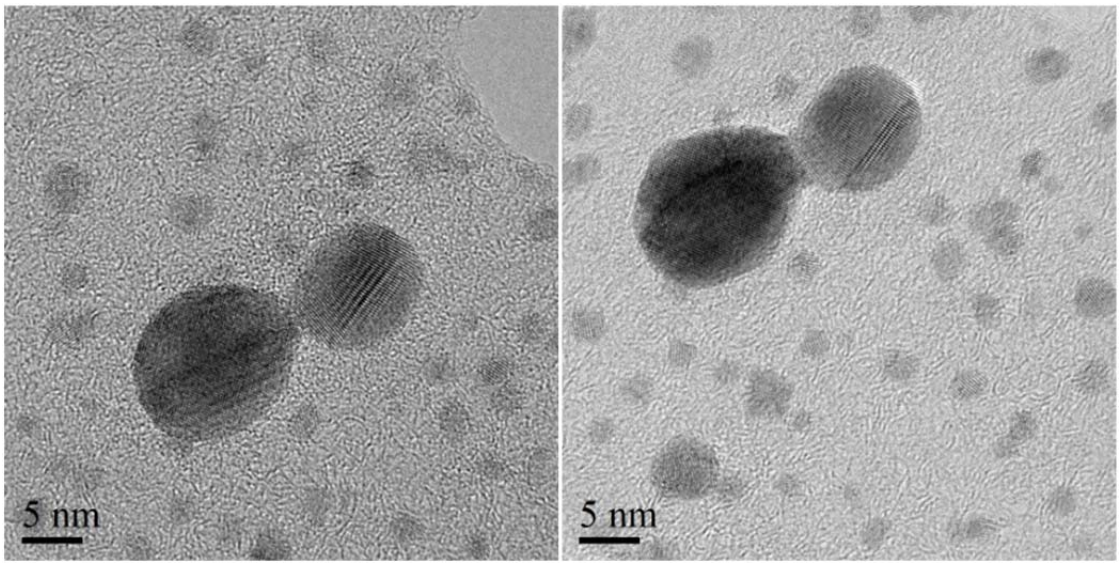

Figure 4.9: *In-situ* TEM heating images showing sintering of 15 nm and 10 nm LAMA silver nanoparticles at 400 °C. The images were recorded at the beginning and end of a 5 minutes video sequence.

Effect of Carbon Surface Coating on Sintering of Nanoparticles

Lastly, to assess the effect of carbon surface coating on sintering of nanoparticles, *in-situ* heating experiments were conducted on nanoparticles where we clearly see carbon coating on the surface. Figure 4.10 shows sintering of 40 nm and 30 nm nanoparticles at 300 °C and we see more carbon residue on the top of the nanoparticles compared to the bottom (indicated with arrow in second frame). We observe that the neck grows more from the bottom of the image than at the top and this is believed to be due to the carbon coating acting as a stearic barrier to sintering of the nanoparticles from the top of the image.

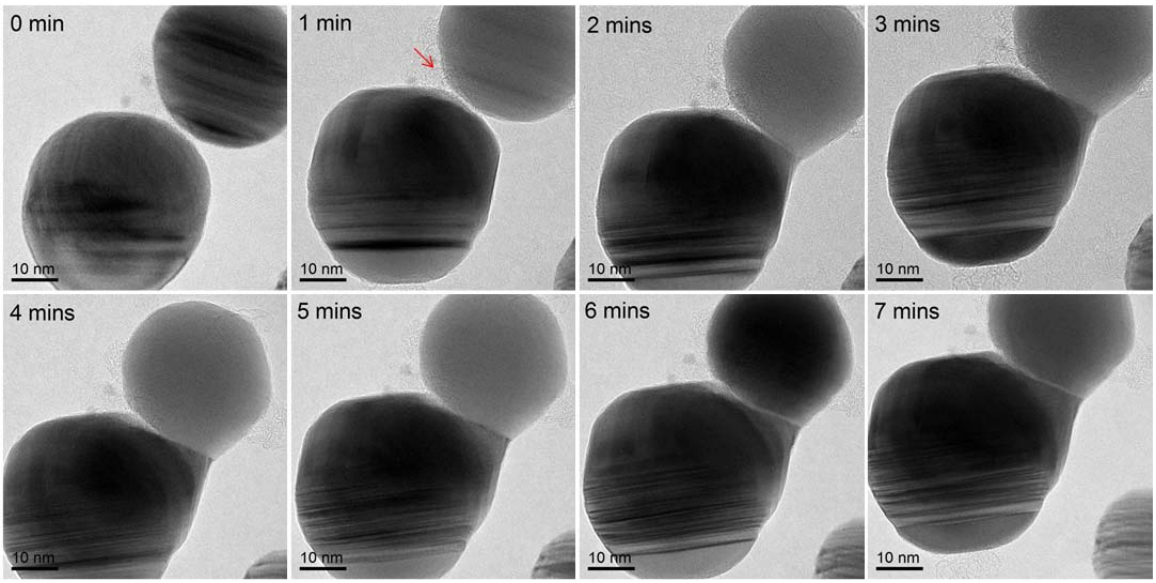

Figure 4.10: A sequence of *in-situ* TEM heating images of 40 nm and 30 nm silver nanoparticles at 300 °C showing that carbon residue on the surface of nanoparticles can prevent neck growth.

Figure 4.11 shows another example of two 15 nm silver nanoparticles with carbon on the surface, sintering at 300 °C. In this case, the carbon seems to cover the neck region and therefore prevents further neck growth after about 20 minutes. The neck region then starts to shrink as the nanoparticle on the right begins to shrink and the nanoparticle on the left grows larger after approximately 18 minutes, possibly by mass transfer through the constrained neck region.

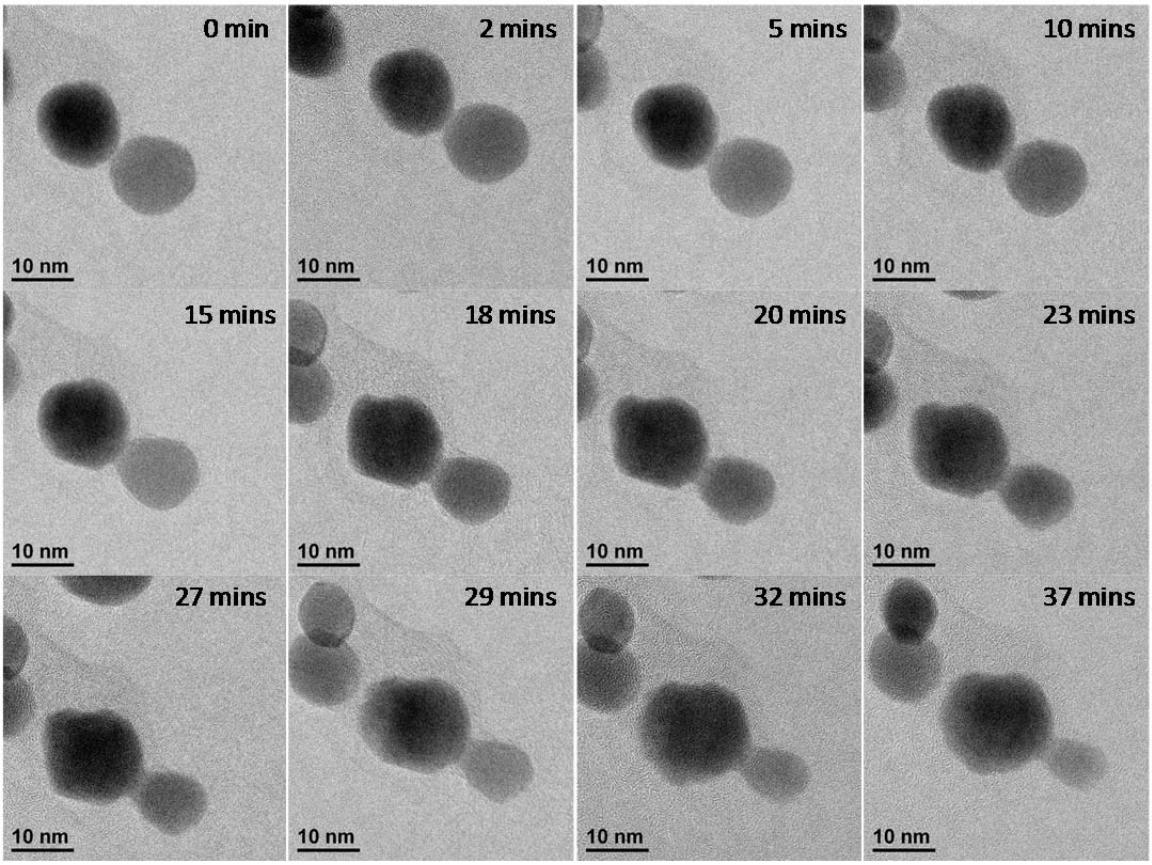

Figure 4.11: *In-situ* TEM heating images of two 15 nm silver nanoparticles at 300 °C shows that carbon coatings on the surface of nanoparticles can slow down neck growth.

4.2 Sintering of Platinum Nanoparticles

To determine the effect of the electron beam on sintering, *in-situ* STEM heating experiments were conducted on 2 nm platinum nanoparticles with the beam turned off intermittently and with beam on throughout the experiment. A sequence of aberration-corrected HAADF STEM images showing the coalescence and sintering of 2 nm platinum nanoparticles under the influence of the electron beam at ambient temperature is shown in Figure 4.12. The images (a) to (c) were recorded at intervals of 20 seconds. However, as the STEM scanning coils take approximately 15 seconds to scan an image, the absolute time between acquiring successive images was approximately 35 seconds. To minimize the influence of the electron beam on the sintering process, the beam was turned off after each image was taken. In Figures 4.12 (a) and (b), sintering occurred mainly by neck growth while in Figure 4.12 (c), grain boundary-driven coarsening is the dominant sintering mechanism. Since the sample is not heated by a heating holder, it is very likely that the sintering of the nanoparticles is initiated by the electron beam either by beam heating or ionization of the sample. We also observe orientation changes in the lattice fringes in the nanoparticles, which confirm that particle rotation accompanies sintering, and agrees with the bright and dark contrast changes observed in the TEM images shown earlier. In addition to the platinum nanoparticles, individual atoms and clusters of platinum can also be observed on the carbon support, which appear to coalesce and sinter with the larger nanoparticles.

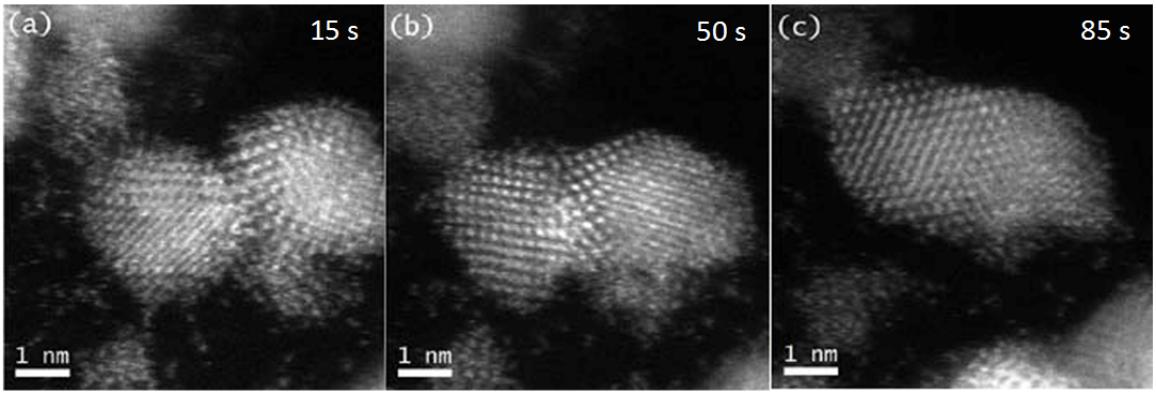

Figure 4.12: A sequence of STEM HAADF images showing the coalescence and sintering of 2 nm platinum nanoparticles after (a) 15 seconds (b) 50 seconds (c) 85 seconds with the electron beam shut off in between images (images courtesy of Prof. Paulo Ferreira and Dr. Larry Allard at Oak Ridge National Laboratory).

Subsequently, a similar experiment was performed to monitor the coalescence and sintering of platinum nanoparticles at ambient temperature but with the beam left on in between images (Figure 4.13). The two nanoparticles start sintering first by making contact followed by neck growth until the two nanoparticles sinter into a single particle. Also, the smaller nanoparticles around the two nanoparticles seem to be mobile on the carbon support and coalescence with the larger nanoparticles after some time. Sintering where the electron beam was turned off intermittently seems to occur faster than in the experiment with the beam left on, which was not expected. Since the electron beam initiates the sintering of the nanoparticles, possibly by beam heating, the sintering process should be faster when the beam is left on compared to when turned off. It is possible that the primary effect of the beam is to activate the sintering process by creating a neck

between the particles (this will be discussed in more detail in section 4.4). Sintering can then proceed at lower temperatures.

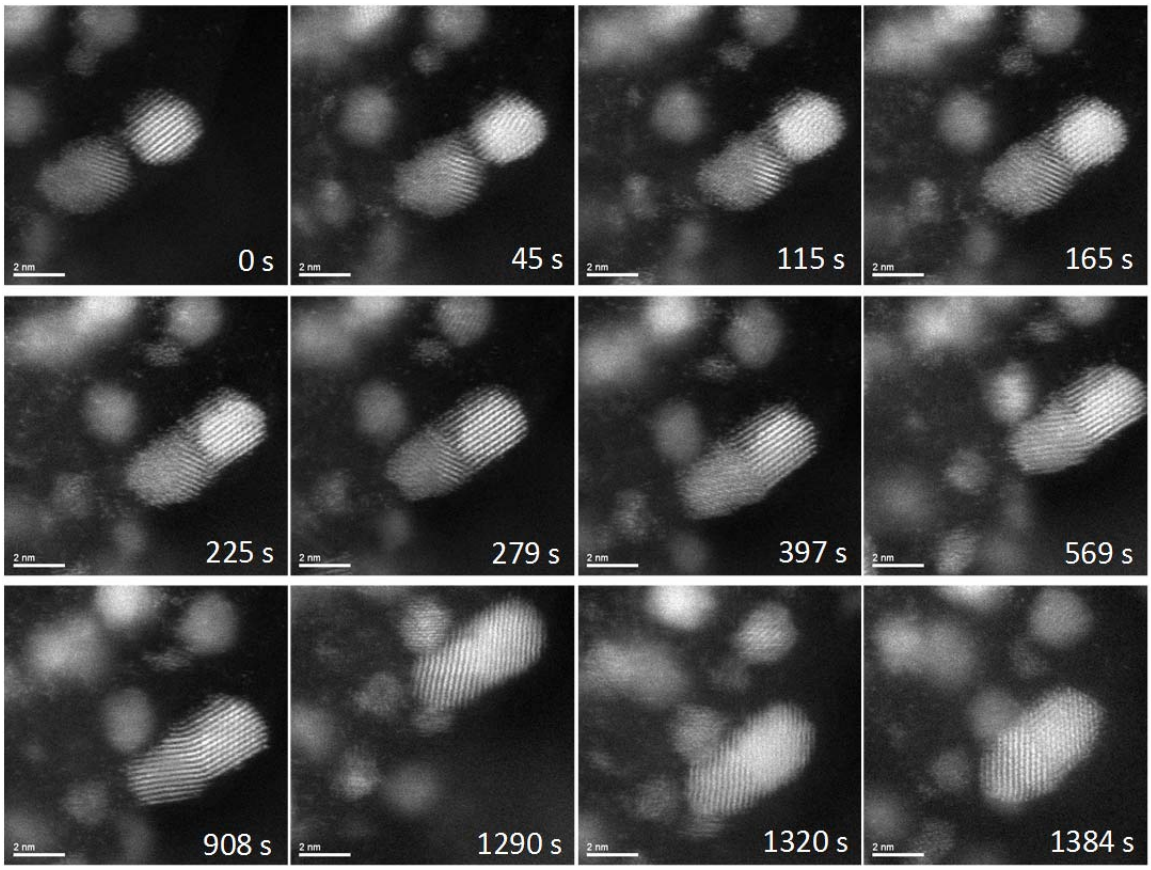

Figure 4.13: A sequence of STEM HAADF images showing the coalescence of platinum nanoparticles. During this sequence, the electron beam was left on between images (images courtesy of Prof. Paulo Ferreira and Dr. Larry Allard at Oak Ridge National Laboratory).

4.3 Fundamental Sintering Parameters Measured as a Function of Temperature and Time

For initial stage sintering, the measured values of particle radius, neck radius and dihedral angle from the *in-situ* TEM images, using the procedure described in section 3.4, are presented below. Note that particles of nearly equal size are chosen for these measurements in order to use the two-particle sintering model, which assumes sintering of uniform sized particles. Figure 4.14 shows an example of the measurements of particle radius, neck radius and dihedral angle from the *in-situ* TEM heating images of silver nanoparticles from Fig. 4.1 after 3 minutes. Similar measurements were done on the entire sequence of TEM/STEM images to obtain the particle radius, neck radius and dihedral angle.

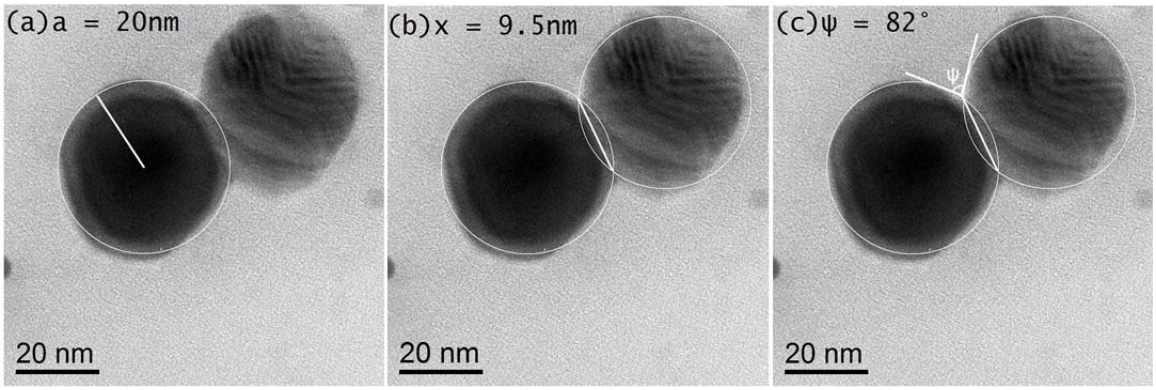

Figure 4.14: *In-situ* TEM heating images of silver nanoparticles showing measurements of (a) particle radius (b) neck radius and (c) dihedral angle.

For the later stages of sintering, the measured dihedral angle for the platinum nanoparticles from Figure 4.12b is shown in Figure 4.15 and as this value approaches the equilibrium dihedral angle, grain boundary motion is expected to initiate, leading to grain coarsening after this point. The particle radius and increase in grain boundary diameter measured from the HAADF STEM images in Figures 4.12 is shown in Figure 4.16.

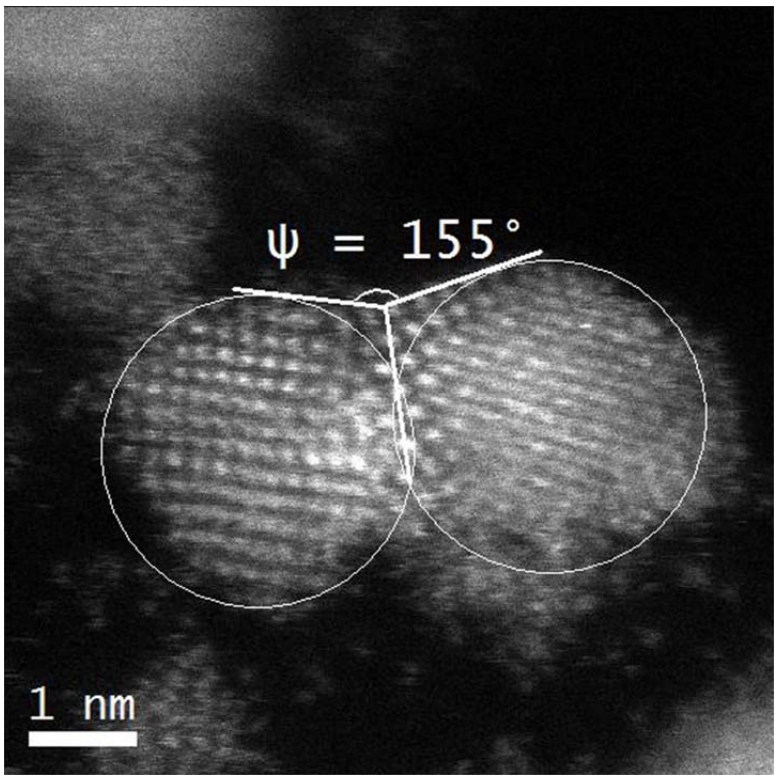

Figure 4.15: Measurement of the dihedral angle between two platinum nanoparticles from Figure 4.12b.

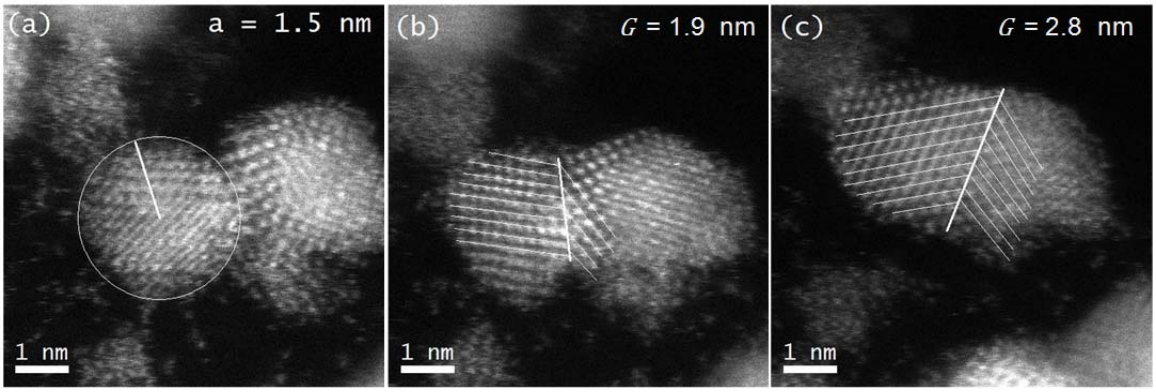

Figure 4.16: *In-situ* STEM images showing the measurements of (a) particle radius (b) and (c) grain boundary diameter.

4.4 Mass Transfer Mechanisms in Sintering of Nanoparticles

The results presented so far have mostly been on sintering between two nanoparticles but it is important to study systems with more than two nanoparticles, since in realistic applications, sintering occurs between many nanoparticles. To investigate the sintering mechanism in such systems, heating experiments have been performed on arrays of nanoparticles, as shown below. Figure 4.17 shows a sequence of *in-situ* TEM images of 6 nm platinum nanoparticles at 100 °C. The particles have been labeled A - D, so as to able to keep track of particle motion. Particles B and C are initially in contact with one another while particles A and D are isolated. After 5 minutes, particle A appears to migrate towards particle B while particle D migrates towards particle C. The particles are monitored for 16 minutes and we observe very little neck growth between particles A and B after the initial contact and particle overlap between particles D and C. Particles B and C also appear to move apart after 9 minutes. There are at least two possible

explanations for the observed behaviors: 1) The nanoparticles may be mobile on the support, moving until they either coalesce when they make contact or, if they are not in the same plane, they may simply overlap (recall that we are observing the projections of three dimensional objects) or 2) It is possible that the carbon support (indicated with arrows) is moving due to differential heating and not the nanoparticles. It is not possible to definitively conclude from these images which of these behaviors are actually occurring, but in Chapter 6, suggestions are provided for tomography experiments that could be used to determine this.

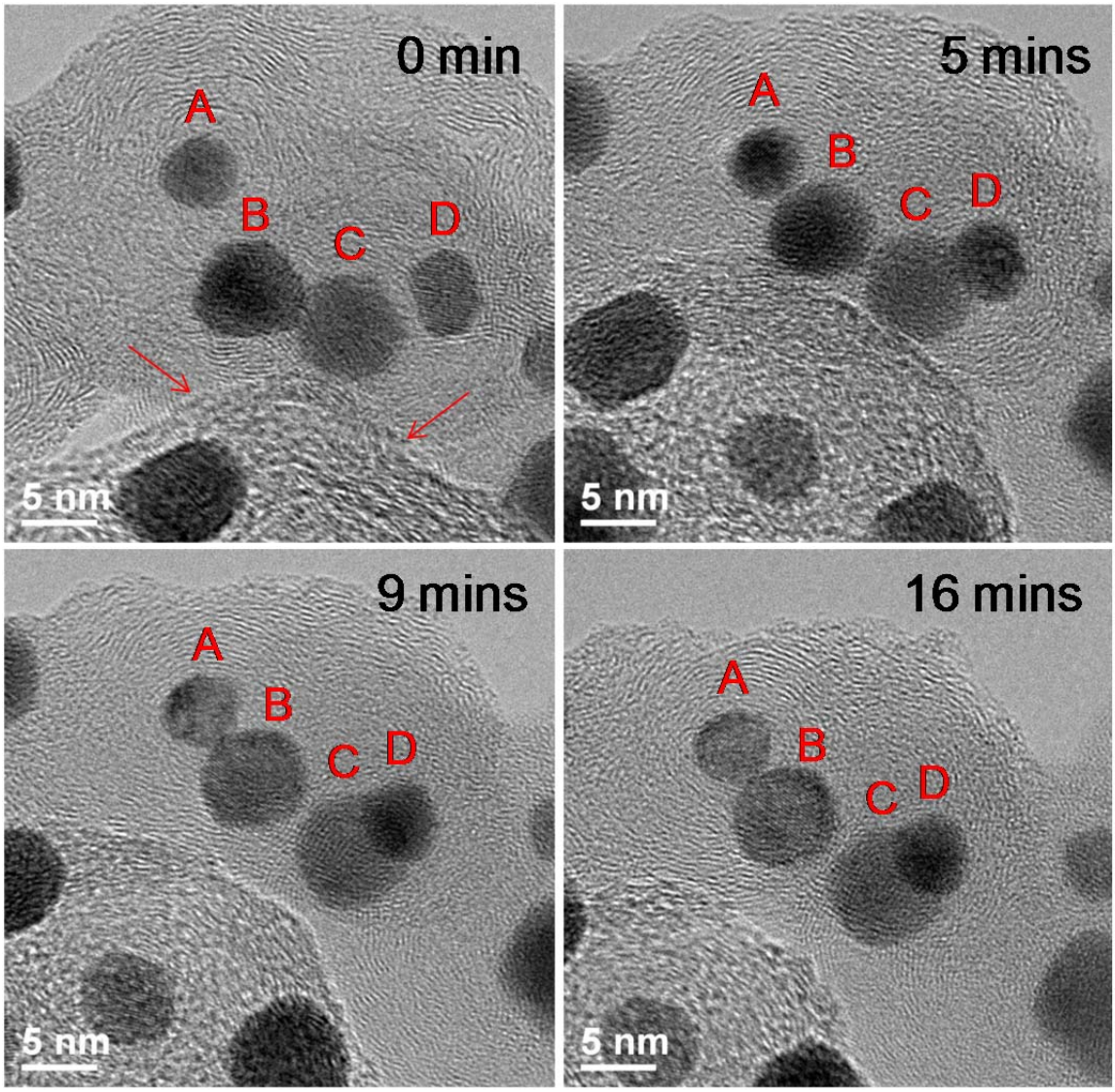

Figure 4.17: A sequence of *in-situ* TEM heating images of 6 nm platinum nanoparticles on a carbon support at 100 °C, showing particle migration and/or motion of the carbon support.

Figure 4.18 is a sequence of HAADF STEM images showing sintering of 2 nm platinum nanoparticles at 500 °C. The particles seem to be mobile on the support, as seen

from the relative positions of the particles labeled 1 – 11 with time. For example, we see that particles 5 and 6 move toward each other and coalesce while particles 9 and 10 drift apart. Also, particles 9 and 11 disappear from the support, and this is likely due to dissolution of the particle onto the carbon support. This suggests that a combination of both coalescence and Ostwald ripening mechanisms can occur during sintering of nanoparticles. However, we do not see the larger nanoparticles growing bigger from Ostwald ripening probably because the relative increase in the volume of the large nanoparticles is small. Also, it is very unlikely that substrate motion is responsible for the apparent relative motion between particles since the motion of the particles occur in a completely random manner. Coalescence is believed to occur when the nanoparticles are mobile on the carbon support and therefore sinter by particle migration after making contact, while Ostwald ripening occurs for small nanoparticles that are immobile on the carbon support but can dissolve in the substrate, diffuse across the substrate and then recondense on larger nanoparticles. These experiments indicate that for many particle systems, Ostwald ripening as well as coalescence can be observed, unlike in two particles sintering, where we mostly observe neck growth due to coalescence. Also, a comparison of the results at 100 °C and 500 °C suggest that Ostwald ripening is more likely to occur at higher temperatures. This is reasonable if the nanoparticle dissolution onto the substrate is increased at higher temperatures.

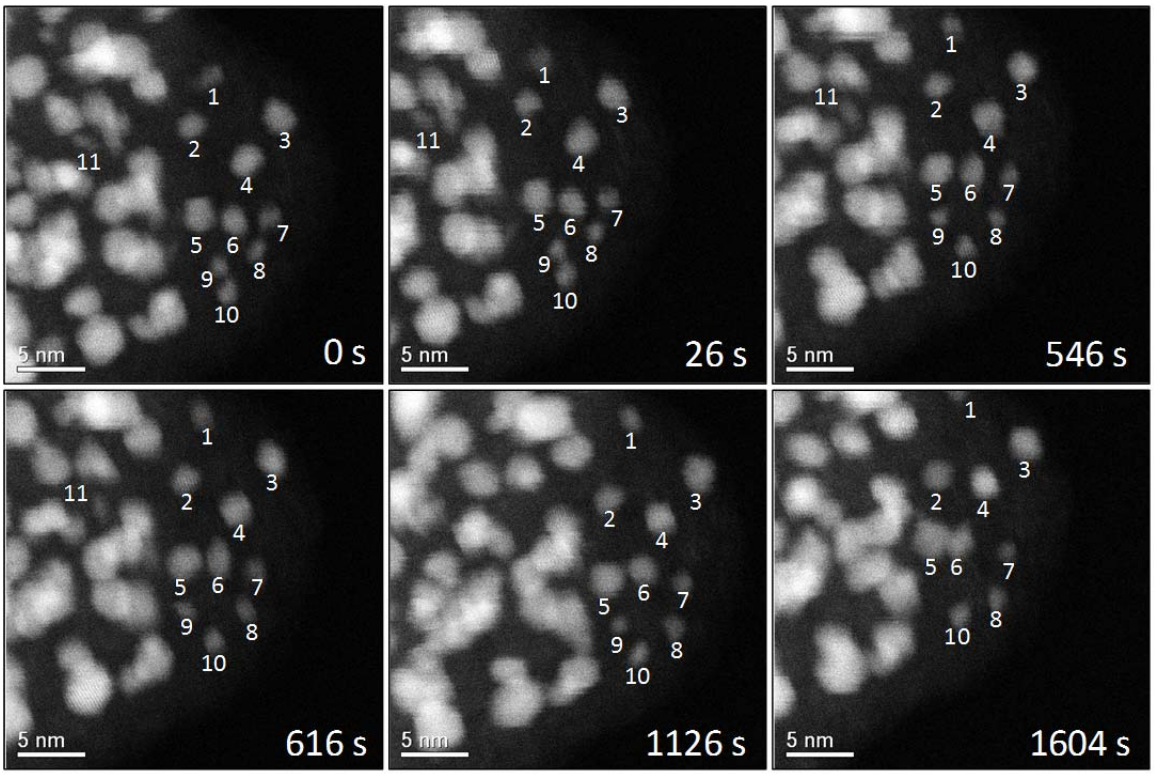

Figure 4.18: *In-situ* STEM heating images of 2 nm platinum nanoparticles at 500 °C, showing that sintering can occur by both particle migration and coalescence as well as Ostwald ripening.

The mechanism for sintering of nanoparticles initially not in contact with each other is investigated further by performing additional *in-situ* heating experiments on 2 nm platinum nanoparticles at 300 °C (Figure 4.19). The nanoparticles are completely separated from each other at the beginning of the experiment and after about 20 minutes, they make contact and sinter together via neck growth. Single atoms and small clusters of platinum seen in these images tend to move on the substrate and aggregate around the larger nanoparticles, possibly by some form of random walk diffusion process. This leads

to the formation of a bridge between the nanoparticles and once contact is made, the neck begins to grow. The motion of the clusters on the substrate is believed to be due to thermal activation of the sample when temperature is increased or some form of electrostatic interaction between the electron beam and the nanoparticles. Batson *et al.* [95, 96] have shown that for small clusters and high beam current densities, forces arise between the particles due to the interactions between the electron beam and the nanoparticles that result in a polarization of the nanoparticles by the electron beam. Although this work is preliminary, it shows a new mechanism for sintering of nanoparticles where small clusters on the substrate can play a major role in sintering of nanoparticles. This opens up a new area of discussion in sintering of nanoparticles and needs to be explored further in the future.

Another significant observation is that, on occasion, nanoparticles are observed to sinter and then de-sinter, as seen in the image taken at 26 minutes. This type of behavior has been shown previously to occur in MgO particles [97]. However, we should point out that these nanoparticles are sitting on a carbon substrate that is not completely flat, as seen from the images acquired at different tilt angles (Figure 4.20) from an FEI Tecnai Spirit TEM with a ±70° tilt tomography holder. Thus, since the nanoparticles are actually embedded in a three-dimensional carbon network, it is possible that the nanoparticles that seem to de-sinter or move apart may actually not be in contact, but instead may be in different planes. This result shows the importance of careful analysis of TEM and STEM images to determine the three-dimensional locations of nanoparticles. This level of analysis has not been performed in previous analyses of nanoparticle sintering.

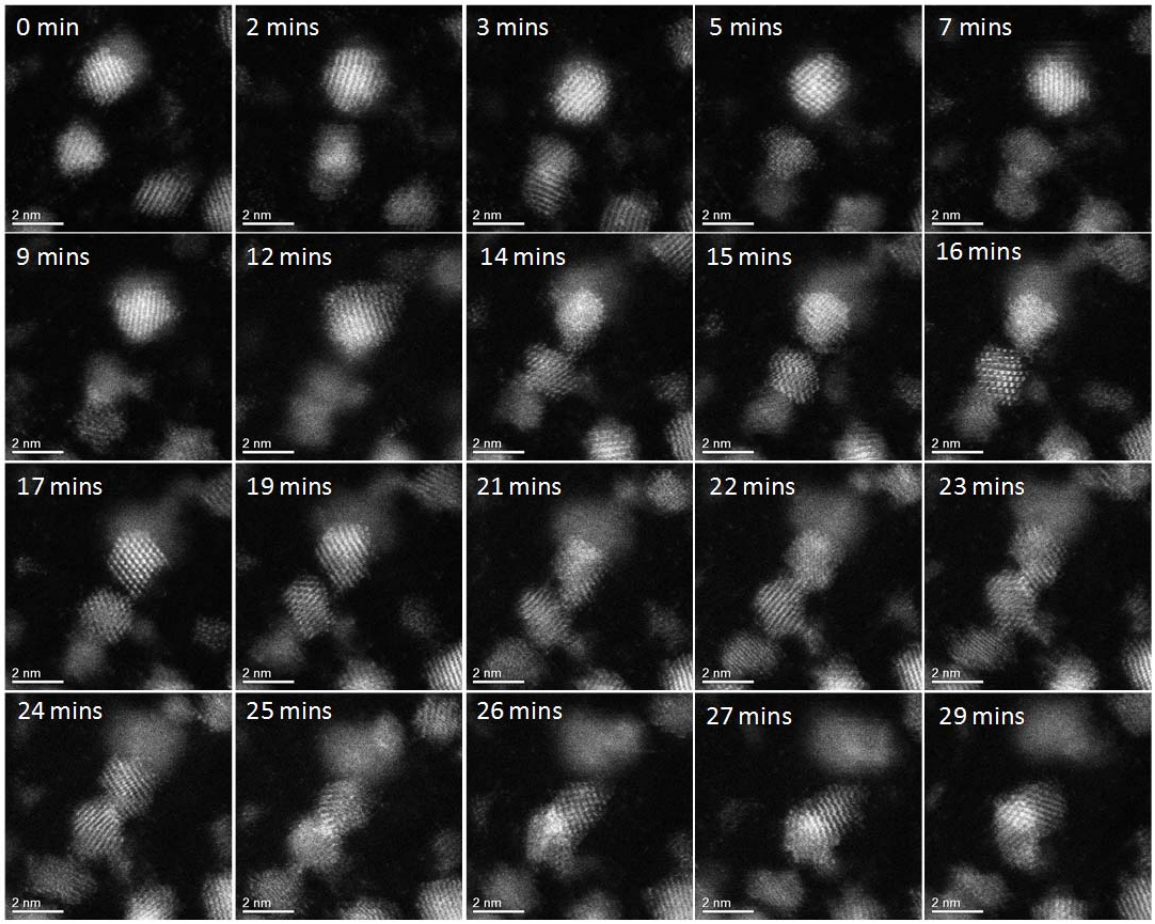

Figure 4.19: *In-situ* STEM heating images of 2 nm platinum nanoparticles at 300 °C, showing that initial contact between nanoparticles during sintering can be achieved by migration of single atoms and small clusters on the substrate towards the neck region.

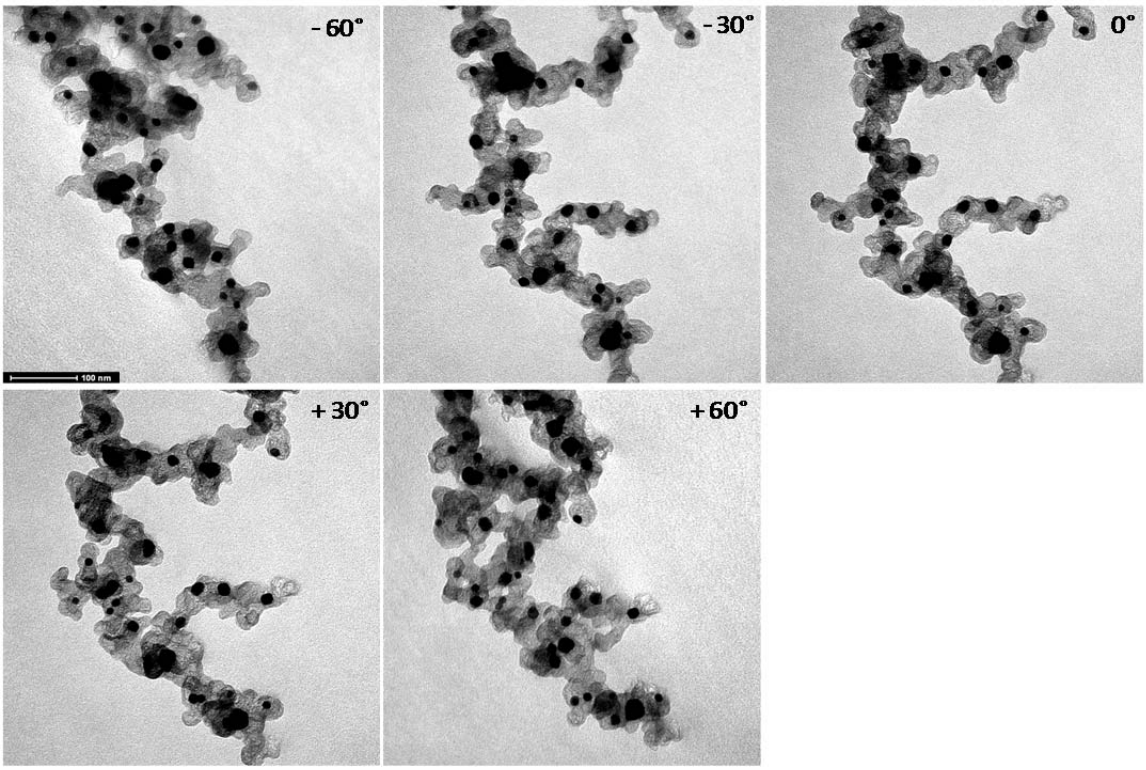

Figure 4.20: TEM tomography images of platinum nanoparticles on a carbon support, obtained over a wide range of tilt angles, shows that the nanoparticles are embedded in a three-dimensional carbon network and may not be co-planar.

Chapter 5: Discussion of Results

5.1 Surface Diffusion Coefficient of Silver and Platinum Nanoparticles

The measured values of neck growth with time between two mono-size nanoparticles undergoing coalescence at a particular temperature is used to calculate the surface diffusivity (equation 2.19) using the methods described in Chapter 3 and assuming surface diffusion is the dominant sintering mechanism. This is a reasonable assumption because, surface diffusion is expected to dominate since the surface diffusivity is at least many orders of magnitude faster than other diffusivities and the surface areas also much larger for nanoparticles compared to bulk materials [61, 98-100]. Note that the surface diffusivity values are calculated with a measurement error bar of ±5% in particle radius and neck radius as described in Chapter 3.

The surface diffusion coefficient, D_s of silver nanoparticles, 12 nm - 40 nm in diameter at temperatures of 200 °C - 400 °C is shown in Figure 5.1. The values of D_s were found to be in the range 4.2×10^{-16} cm^2/s - 1.1×10^{-20} cm^2/s. These samples contain a carbon coating, added during synthesis and may also contain some adsorbed species or oxides on the surface due to exposure to the atmosphere. Figure 5.1 also shows other reported values of surface diffusivities for bulk silver and thin films of silver obtained under different conditions and at different temperatures. It should be noted that there is a large scatter in the reported values of surface diffusivities for bulk silver at high temperatures (400 °C – 900 °C) and in different environments (vacuum, air, hydrogen and nitrogen) [101]. Thus, the values from Guy [61] only represents an estimate. Also,

bulk surface diffusivities are typically measured at temperatures above 0.5 T_m, because sintering is too slow to observe experimentally in micro-scale materials at lower temperatures, using conventional methods for measuring diffusivity. In addition, extrapolations to temperatures below 0.5 T_m using the Arrhenius relationship of diffusivity with temperature may not be valid because the fundamental mechanism of diffusion can change with temperature regime and small uncertainties in the high temperature data can lead to large errors when extrapolated to low temperatures. Therefore, we must be cautious in making quantitative comparisons between our results and previous values. Nevertheless, it is clear that our measured surface diffusivities are several orders of magnitude lower than reported bulk values. Also, surface diffusivities have been measured previously on thin films of silver at room temperature and in ultra-high vacuum using scanning tunneling microscopy (STM). These values (10^{-15} - 10^{-18} cm^2/s) [102-104] are also significantly lower than the values obtained from bulk silver at high temperatures and extrapolated to room temperature (10^{-13} cm^2/s). Our values when extrapolated to room temperatures will be slightly lower than the values from the STM experiments, possibly because of the differences in sample surface condition and microscope vacuum levels. These results suggest that the values of surface diffusivities for silver can be very sensitive to the surface conditions and atmospheric contamination. In fact, the activation energy for surface diffusion, E_D on thin films of silver obtained from scanning tunneling microscopy (STM) [105] and Spot-Profile Analysis of Low-Energy Electron Diffraction (SPA-LEED) [106] experiments performed in ultra high vacuum, are significantly lower than E_D values obtained from resistivity measurements

on thin, (111) oriented films of silver in air [107]. Therefore the sintering environment plays a major role in the sintering process and presence of oxides or other adsorbed species on the surface of the nanoparticles can possibly retard the sintering of the nanoparticles. Thus, our measured values of diffusivities, due to the presence of carbon or adsorbed species on the surface of our nanoparticles, do not represent the intrinsic surface diffusivities of silver but an effective diffusivity of silver nanoparticles under realistic conditions. This is a very important point, since most commercially available nanoparticles usually contain some form of hydrocarbon added to prevent particle agglomeration. These hydrocarbons pyrolyze during sintering, resulting in carbon residue as well as gas evolution. In fact values of diffusion coefficients significantly lower than the surface diffusivity for bulk silver has been previously reported for silver in pyrolytically deposited carbon, from helium scattering experiments [108]. These values of diffusivity in Ag/C system (10^{-16} – 10^{-12} cm^2/s in the temperature range of 450 - 800 °C), when extrapolated to low temperatures, agree well with our measurements (Figure 5.1).

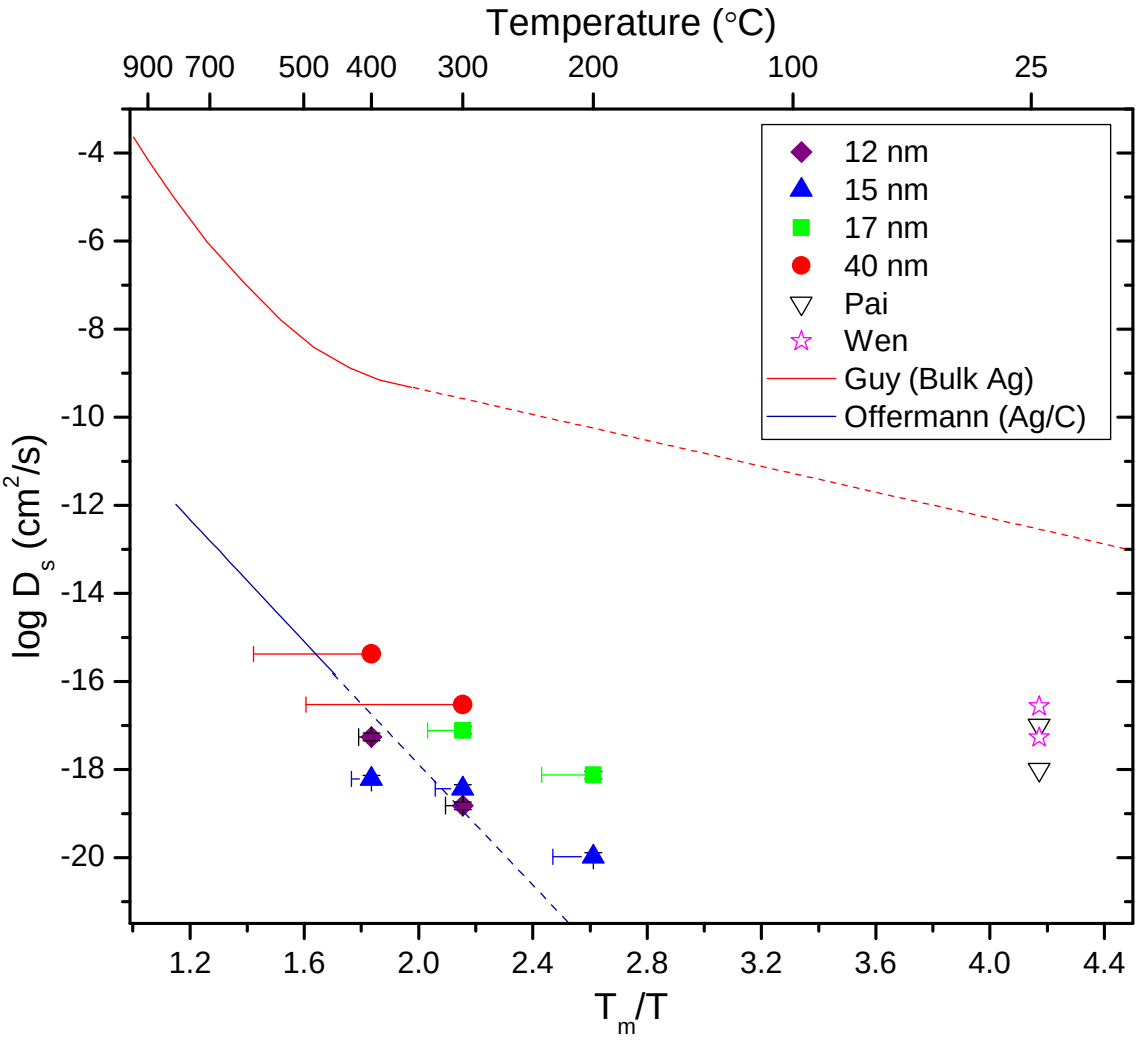

Figure 5.1: Plot of surface diffusivity versus temperature for silver. The filled symbols are for the current results while the open symbols are the previously reported values. The solid line represents estimated values of surface diffusivities for bulk silver and silver on carbon at high temperatures and the dashed line is the corresponding extrapolation to low temperatures.

The surface diffusion coefficient, D_s for 2 nm platinum nanoparticles at room temperature was calculated to be in the range 1.5×10^{-20} - 6.5×10^{-20} cm^2/s based on our observed sintering rates. Figure 5.2 shows a comparison of our values with measurements from other experiments at or near ambient temperature on 300 nm thick platinum nanosheets on graphite (10^{-15} - 10^{-16} cm^2/s) [109], platinum single atoms on platinum (110) surfaces (3.16×10^{-19} cm^2/s) [110] and columnar structured platinum electrodes (1.13×10^{-19} cm^2/s) [111]. Also shown on this plot is data obtained from bulk platinum [99] at high temperature with the corresponding exponential extrapolations to room temperature. This plot shows that our diffusivity values are in general agreement with the diffusivities obtained from previous work. Our calculations also show that the electron beam does not seem to have a significant effect on the surface diffusivity, since we obtained similar values from both experiments where the beam was left on and turned off during the time between when images were captured. However, as stated earlier, we believe the beam possibly activates the sintering of the nanoparticles at room temperature, though we expect very little beam heating for 2 nm nanoparticles.

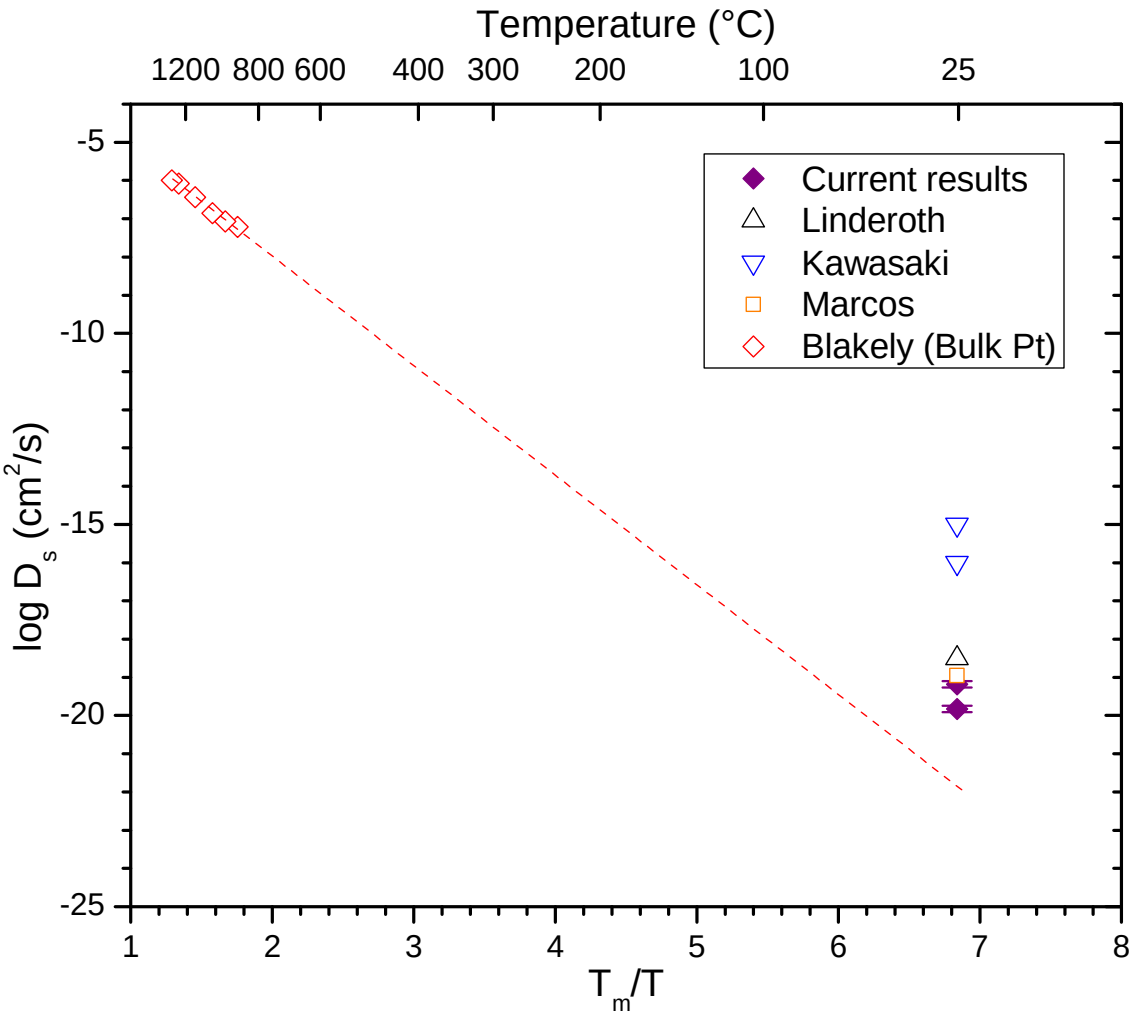

Figure 5.2: Plot of surface diffusivity versus temperature for platinum. The dashed line is obtained from extrapolation of bulk platinum measurements from high temperature.

5.2 Grain Boundary Mobility of Silver and Platinum Nanoparticles

For the later stages of sintering, the measured values of particle radius, grain boundary velocity and increase in boundary diameter during coarsening are used to calculate the grain boundary mobility (equation 2.23) using the methods discussed in

Chapter 3. The equilibrium dihedral angle, ψ is about 161° for silver and 163° for platinum (from equation 2.20). The dihedral angle measured from Figure 4.11b is quite close to the equilibrium angle for platinum (Figure 4.14), therefore grain boundary motion is expected to initiate at this point and cause grain coarsening after this point. To calculate the grain boundary mobility, the particle radius is first measured (Figure 4.15a). Subsequently, the grain boundary is identified at the region where there is a distinct change in the orientation of the crystal lattice which is readily apparent in the micrographs (Figures 4.11b and 4.11c). The increase in grain boundary area, dA as the grain boundary advances is calculated from equation (2.24) and from the differences in boundary area assuming a circular boundary. The grain boundary velocity, v is obtained by measuring the distance moved by the grain boundary from Figure 4.11b to 4.11c using the DigitalMicrograph software and then dividing by the time between which the two images were taken. From equation (2.23), the mobility, M for platinum nanoparticles is calculated to be in the range 2.5×10^{-20} - 3.1×10^{-20} $m^4s^{-1}J^{-1}$ and for silver nanoparticles $M = 8.2 \times 10^{-20} - 9.1 \times 10^{-20}$ $m^4s^{-1}J^{-1}$. Grain boundary mobility values for silver and platinum were not found in the literature but our values are lower than reported grain boundary mobility values for other FCC metals like copper (6.31×10^{-16} $m^4s^{-1}J^{-1}$) [112] and aluminum (10^{-15} $m^4s^{-1}J^{-1}$) [113] at higher temperatures. The grain boundary mobility will also depend on the grain boundary type and misorientation angle between the two nanoparticles, and this needs to be explored further in order to make more direct comparisons. For example, the grain boundary mobility has been shown to increase with

misorientation angle for aluminum [114] and similar results can also occur for silver and platinum.

5.3 Effect of Particle Size on Sintering of Nanoparticles

Figure 5.1 shows that the surface diffusivity of silver nanoparticles slightly increases with size at a given temperature for the size range studied, which is unexpected. However, if we consider the error bars in temperature, it is not possible to conclude that this effect is statistically significant. Also, our values of surface diffusivities for silver nanoparticles are significantly lower than bulk silver values extrapolated from high temperatures. Nanoparticles have a larger kinetic driving force for sintering to occur due to their enhanced curvature compared to bulk, and will therefore have an increased atomic flux. Thus, the diffusivity of nanoparticles is expected to be either similar or larger than bulk diffusivity and not smaller. As mentioned before, this is probably due to the presence of carbon or other surface impurities on the surface of the nanoparticles, leading to a lower effective diffusivity. However, in the case of platinum (Figure 5.2), our values of surface diffusivities are in close agreement with bulk values extrapolated from high temperatures.

5.4 Effect of Temperature on Sintering of Nanoparticles

Figure 5.1 shows that surface diffusivity generally increases with increasing temperature for nanoparticles of similar sizes. This is expected since sintering is a thermally activated process and therefore surface diffusion should increase with

temperature. From equation (5.1), the activation energy for surface diffusion can be obtained from the slope of a plot of ln D_s versus 1/T (Figure 5.3).

$$D = D_o exp\left(\frac{-E_D}{kT}\right) \qquad (5.1)$$

where D_o is the diffusivity prefactor, E_D is the activation energy for diffusion and k is the Boltzmann constant. However, the large error bars in temperature and the relatively poor fit of the data, make it impossible to obtain accurate activation energy for surface diffusion, E_D from our experiments. Also, this data is obtained from nanoparticles with sizes ranging from 12 nm – 40 nm, and size effects might also account for some of the observed large scatter.

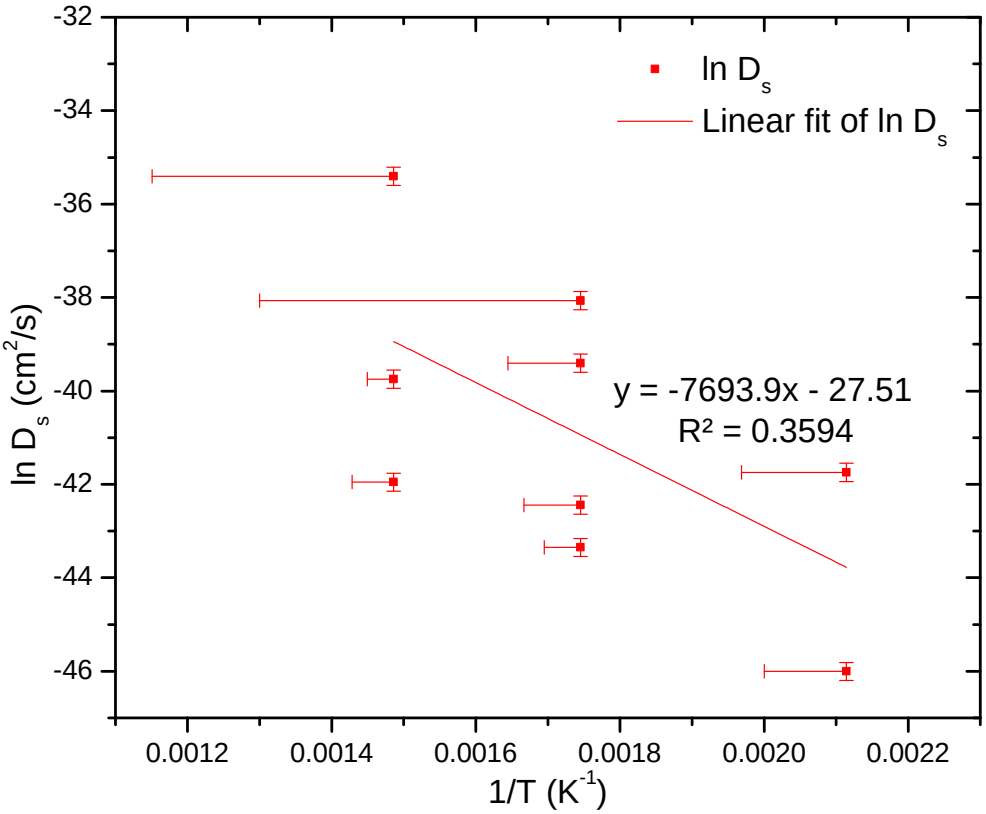

Figure 5.3: Plot of ln D_s versus 1/T for silver nanoparticles.

Because of the uncertainty in the temperature measurements during our sintering experiments discussed in chapter 3, it is useful to put a bound on the influence of this uncertainty on our calculated values of D_s. Equation 5.1 can be used to determine how sensitive the surface diffusion coefficient is to temperature changes by plotting $\Delta \log D_s$ versus ΔT for the range of temperatures used in our experiments (Figure 5.4). For these calculations, we use the previously reported values of diffusivity prefactor, D_o (1.6×10^{-3} cm^2/s) and activation energy for surface diffusion, E_D (0.4 eV) obtained from STM measurements on silver (100) surfaces [115]. We see that for a temperature variation of

up to 150 °C, the diffusivity values changes by an order of magnitude or less, which is relatively minor compared to the variations in diffusivity that has been reported in the literature. Therefore, the temperature uncertainty due to electron beam heating should not significantly affect the measured values of surface diffusivity.

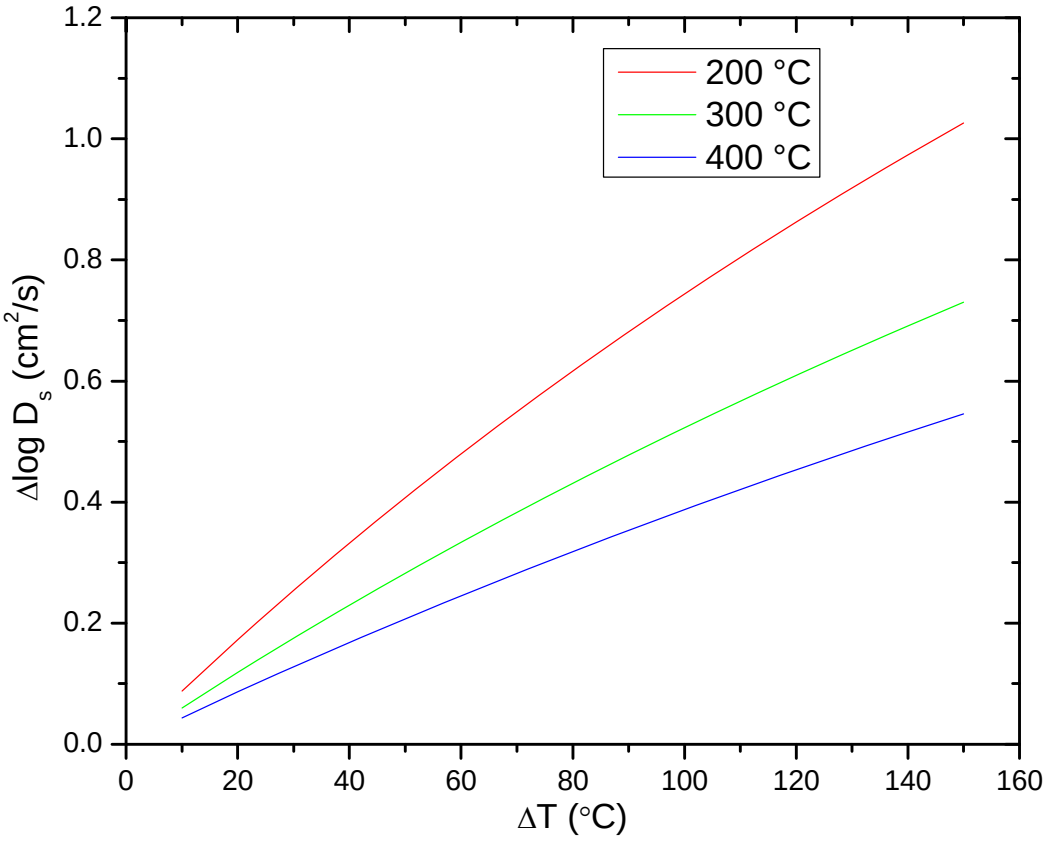

Figure 5.4: Plot of $\Delta \log D_s$ versus ΔT, showing the effect of a change in temperature on surface diffusion coefficient.

5.5 Effect of Carbon Surface Coating on Sintering of Nanoparticles

As shown in Figures 4.9 and 4.10, the carbon that typically resides on the surface of nanoparticles, either because it was intentionally added or because it is a remnant of the process used to produce and stabilize the nanoparticulate colloid during processing, can serve as a barrier to sintering of nanoparticles. To further investigate the effect of carbon, sintering experiments were conducted on LAMA silver nanoparticles deposited directly on a thin silver wire, which was then placed on special Protochips heater grid that did not contain the typical holey carbon. Figure 5.5 is a sequence of *in-situ* TEM images showing sintering of a 40 nm LAMA silver nanoparticle with a 35 μm silver wire at 400 °C. We see that the silver nanoparticle formed a neck with the silver wire by the time the first image could be captured in 3 minutes. Subsequent observations did not reveal significant additional neck growth during heating for 11 minutes. Although the amount of surface contamination on the wire and nanoparticle surface was reduced compared to nanoparticle experiments on carbon supports, there is still some contamination that is visible. This contamination could have occurred during atmospheric exposure when transferring the wire to the grid. Raman spectra of LAMA-produced silver nanoparticles also show some extra peaks due to some C-H species present in the sample after exposure to atmospheric conditions [116], suggesting that the nanoparticles can easily absorb some gases or hydrocarbons when exposed to the atmosphere.

The sphere-on-plate sintering geometry derived by Kuczynski [25] is used to calculate the surface diffusivity from our measured values of particle radius and neck radius with time. For a 40 nm nanoparticle at 400 °C, the surface diffusivity was

determined to be $1.2 \times 10^{-14} - 1.8 \times 10^{-14}$ cm^2/s, which is two orders of magnitude greater than the value obtained previously for the same size particles with carbon surface coating and at the same temperature. It should be noted that this calculation only gives a lower bound of the surface diffusivity value since the neck growth is first measured after 3 minutes, and it is possible that sintering occurred earlier but could not be captured fast enough. However, these results confirm our hypothesis that, the carbon surface coating significantly slows sintering in nanoparticles.

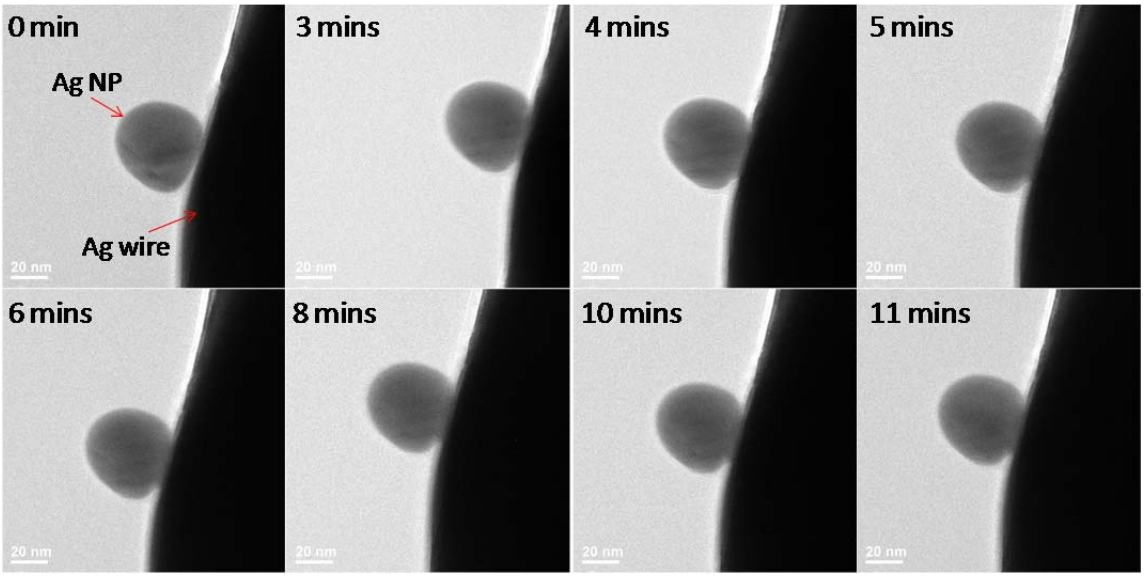

Figure 5.5: *In-situ* TEM images showing sintering of a 40 nm LAMA silver nanoparticle with a 35 μm diameter silver wire at 400 °C.

From these experiments, we can propose a qualitative model for the influence of carbon on sintering. When the surface of the silver nanoparticle is covered with carbon,

as shown schematically in Figure 5.6, diffusion of atoms from the surface to the neck occurs through the carbon. As the neck grows, the carbon surface coating is pushed outward from the neck region to drive further growth, but this process will be slower than surface diffusion of silver without any carbon, which results in the decrease in the observed diffusivity values in the presence of carbon. Also, our effective surface diffusivity values for silver nanoparticles due to interfacial diffusion of silver in carbon are in agreement with previously reported values for diffusion of silver in pyrolytically deposited carbon [108].

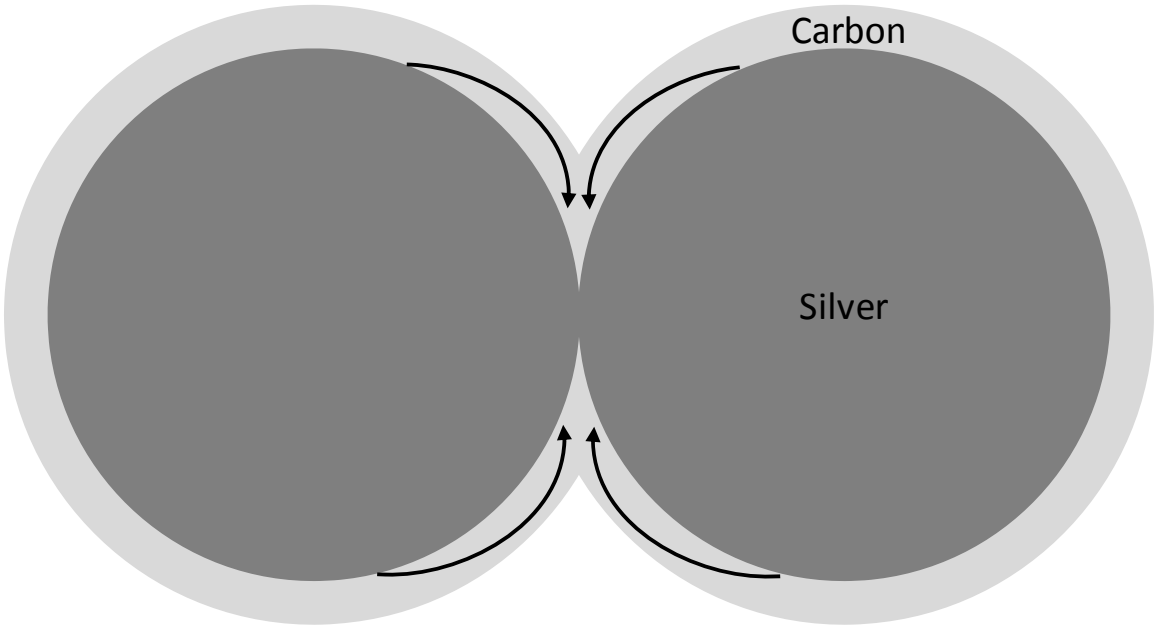

Figure 5.6: Schematic of sintering of two nanoparticles covered with a carbon surface coating, shows that for the neck to grow, atomic diffusion from the surface to the neck occurs through the carbon.

Chapter 6: Conclusions and Future Work

6.1 Conclusions

The low temperature sintering of silver and platinum nanoparticles have been studied using a novel Protochips Aduro^{TM} heating holder for *in-situ* TEM/STEM heating experiments. Prior to assessing sintering behavior, the temperature of the heating holder was first calibrated by measuring the sublimation kinetics of silver nanoparticles, a transformation with known kinetics and, that is highly sensitive to temperature. By measuring the change of particle radius with time and using other known properties of silver, the temperature could be accurately determined. These results agreed well with theoretical predictions and previous experiments, but only when the effects of the electron beam heating on the actual temperature of the nanoparticles were accounted for. These results showed that beam heating effects during *in-situ* heating experiments with small nanoparticles (< 40 nm) are significant and must be accounted for.

This *in-situ* TEM heating technique was combined with an analysis methodology in order to make direct, real-time measurements of nanoparticle size, neck growth, dihedral angle and grain boundary motion during sintering. Fundamental mass transport parameters such as surface diffusivity and grain boundary mobility that are important in understanding sintering at the nanoscale were then calculated from these measurements. Our calculated values of D_s (4.2×10^{-16} cm^2/s - 1.1×10^{-20} cm^2/s) for silver nanoparticles are significantly lower than previously reported values for bulk silver measured at high temperatures and extrapolated to lower temperatures and also are lower than the values

for thin silver films measured in ultra-high vacuum at room temperature using STM. Our experiments and previous measurement of surface diffusivity suggest that surface impurities present on the silver and/or carbon are a likely cause for this discrepancy. Our experiments showed that the presence of carbon on the surface of nanoparticles can significantly inhibit sintering in nanoparticles. For example, sintering experiments performed between a nominally bare silver nanoparticle and a silver wire showed at least a two orders of magnitude increase in surface diffusivity compared to carbon-capped nanoparticles. The effective diffusivities that were measured for silver nanoparticles with carbon surface coatings matches well with reported values of diffusivity of silver in pyrolytically deposited carbon.

In contrast to the results obtained for silver, the values of D_s measured for platinum are in close agreement with reported bulk values extrapolated from high temperatures and measurements performed at room temperature. This is believed to be due to the fact that platinum, being a more noble metal than silver, is less susceptible to atmospheric contamination and may also be less susceptible to impurity effects on surface diffusion.

The aforementioned electron beam heating effects result in a 20 °C – 150 °C increase in temperature over the temperature measured without the beam. The large range in temperatures caused by beam heating results from variations in beam current, nanoparticle size, and, most importantly, the contact area between the nanoparticle and the substrate upon which the nanoparticle rests. This range results in some uncertainty in the temperature during our experiments and a corresponding uncertainty in the surface

diffusivity, which was determined to be at most one order of magnitude. While this level of uncertainty is great enough that small variations in diffusivity cannot be determined using this technique, it is reasonably accurate compared to the large range in measured surface diffusivities that have been reported in the literature for silver. Within the accuracy of the measurements, we did not observe a statistically significant effect of particle size on the surface diffusivity of silver, which suggests that such an effect is relatively small over the range of nanoparticle sizes that were measured (12 - 40 nm).

Two mechanisms were observed for sintering in nanoparticles: a surface Ostwald ripening process in which mass dissolves onto the substrate and is transported and deposits on another particle, as well as more conventional particle migration and coalescence. We observed that the Ostwald ripening process was more likely to occur at higher temperatures. For coalescence, we observed that the initial contact between nanoparticles can be initiated by 1) movement of the particles towards each other, 2) migration of single atoms and small clusters on the support towards the neck region or 3) motion of the substrate due to differential heating caused by the electron beam. Atomic or cluster migration are mechanisms for sintering that have not been previously reported. This finding is important because it shows that the small clusters of atoms on the support may affect the sintering of larger nanoparticles by forming a bridge in between the nanoparticles, which then leads to subsequent neck growth.

6.2 Future Work

The sintering behavior of nanoparticles can be further understood by using other *in-situ* TEM techniques, as described below:

1) Investigation of the effect of sintering atmosphere on sintering of nanoparticles can be performed using an *in-situ* TEM/STEM environmental-cell heating holder to perform sintering experiments in different gas environments. For example, a reducing atmosphere of hydrogen can be used to remove any adsorbed species or oxides on the surface of silver nanoparticles and therefore allow us to study the intrinsic sintering behavior of the nanoparticles. Also, the effect of oxygen on the sintering behavior can be quantified by performing these experiments in environments with varying oxygen content, after exposure to a reducing atmosphere. These experiments can also answer the pertinent question of why the activation energy for surface diffusion of silver nanoparticles exposed to air is higher than previously reported values from measurements made in ultra high vacuum.

2) An *in-situ* TEM heating holder coupled with a tomography holder can be used for 3-D imaging of nanoparticles during sintering, to provide more insight into the sintering behavior of nanoparticles and also clearly distinguish particle overlap from actual particle contact. The neck and grain boundary regions can be reconstructed to give a three dimensional view of how neck growth and grain

boundary migration occurs. Preliminary results obtained using a tomography holder shows a three-dimensional view of the silver and platinum nanoparticles rotated through ± 60° in the microscope.

Appendix A: Matlab® program for least-square fitting of circles and ellipses

```
function [z, r, residual] = fitcircle(x, varargin)
%FITCIRCLE    least squares circle fit
%
%  [Z, R] = FITCIRCLE(X) fits a circle to the N points in X minimising
%  geometric error (sum of squared distances from the points to the fitted
%  circle) using nonlinear least squares (Gauss Newton)
%     Input
%        X : 2xN array of N 2D points, with N >= 3
%     Output
%        Z : center of the fitted circle
%        R : radius of the fitted circle
%
%  [Z, R] = FITCIRCLE(X, 'linear') fits a circle using linear least
%  squares minimising the algebraic error (residual from fitting system
%  of the form ax'x + b'x + c = 0)
%
%  [Z, R] = FITCIRCLE(X, Property, Value, ...) allows parameters to be
%  passed to the internal Gauss Newton method. Property names can be
%  supplied as any unambiguous contraction of the property name and are
%  case insensitive, e.g. FITCIRCLE(X, 't', 1e-4) is equivalent to
%  FITCIRCLE(X, 'tol', 1e-4). Valid properties are:
%
%     Property:               Value:
%     ------------------------------
%     maxits                  positive integer, default 100
%        Sets the maximum number of iterations of the Gauss Newton
%        method
%
%     tol                     positive constant, default 1e-5
%        Gauss Newton converges when the relative change in the solution
%        is less than tol
%
%  [X, R, RES] = fitcircle(...) returns the 2 norm of the residual from
%  the least squares fit
%
%  Example:
%     x = [1 2 5 7 9 3; 7 6 8 7 5 7];
%     % Get linear least squares fit
%     [zl, rl] = fitcircle(x, 'linear')
%     % Get true best fit
%     [z, r] = fitcircle(x)
```

```
%
%   Reference: "Least-squares fitting of circles and ellipses", W. Gander,
%   G. Golub, R. Strebel - BIT Numerical Mathematics, 1994, Springer

% This implementation copyright Richard Brown, 2007, but is freely
% available to copy, use, or modify as long as this line is maintained

error(nargchk(1, 5, nargin, 'struct'))

% Default parameters for Gauss Newton minimisation
params.maxits = 100;
params.tol    = 1e-5;

% Check x and get user supplied parameters
[x, fNonlinear, params] = parseinputs(x, params, varargin{:});

% Convenience variables
m  = size(x, 2);
x1 = x(1, :)';
x2 = x(2, :)';


% 1) Compute best fit w.r.t. algebraic error using linear least squares
%
% Circle is represented as a matrix quadratic form
%     ax'x + b'x + c = 0
% Linear least squares estimate found by minimising Bu = 0 s.t. norm(u) = 1
%     where u = [a; b; c]

% Form the coefficient matrix
B = [x1.^2 + x2.^2, x1, x2, ones(m, 1)];

% Least squares estimate is right singular vector corresp. to smallest
% singular value of B
[U, S, V] = svd(B);
u = V(:, 4);

% For clarity, set the quadratic form variables
a = u(1);
b = u(2:3);
c = u(4);

% Convert to centre/radius
```

```
z = -b / (2*a);
r = sqrt((norm(b)/(2*a))^2 - c/a);

% 2) Nonlinear refinement to minimize geometric error, and compute residual
if fNonlinear
   [z, r, residual] = fitcircle_geometric(x, z, r);
else
   residual = norm(B * u);
end

% END MAIN FUNCTION BODY

% NESTED FUNCTIONS
   function [z, r, residual] = fitcircle_geometric(x, z0, r0)
      % Use a simple Gauss Newton method to minimize the geometric error
      fConverged = false;

      % Set initial u
      u     = [z0; r0];

      % Delta is the norm of current step, scaled by the norm of u
      delta = inf;
      nIts  = 0;

      for nIts = 1:params.maxits
         % Find the function and Jacobian
         [f, J] = sys(u);

         % Solve for the step and update u
         h = -J \ f;
         u = u + h;

         % Check for convergence
         delta = norm(h, inf) / norm(u, inf);
         if delta < params.tol
            fConverged = true;
            break
         end
      end

      if ~fConverged
         warning('fitcircle:FailureToConverge', ...
            'Gauss Newton iteration failed to converge');
```

```
        end
        z = u(1:2);
        r = u(3);
        f = sys(u);
        residual = norm(f);


        function [f, J] = sys(u)
           %SYS   Nonlinear system to be minimised - the objective
           %function is the distance to each point from the fitted circle
           %contained in u

           % Objective function
           f = (sqrt(sum((repmat(u(1:2), 1, m) - x).^2)) - u(3))';

           % Jacobian
           denom = sqrt( (u(1) - x1).^2 + (u(2) - x2).^2 );
           J = [(u(1) - x1) ./ denom, (u(2) - x2) ./ denom, repmat(-1, m, 1)];
        end % sys

    end % fitcircle_geometric

% END NESTED FUNCTIONS

end % fitcircle




function [x, fNonlinear, params] = parseinputs(x, params, varargin)
% Make sure x is 2xN where N > 3
if size(x, 2) == 2
    x = x';
end

if size(x, 1) ~= 2
    error('fitcircle:InvalidDimension', ...
        'Input matrix must be two dimensional')
end

if size(x, 2) < 3
    error('fitcircle:InsufficientPoints', ...
```

```
        'At least 3 points required to compute fit')
end

% determine whether we are measuring geometric error (nonlinear), or
% algebraic error (linear)
fNonlinear = true;
switch length(varargin)
   % No arguments means a nonlinear least squares with default parameters
   case 0
      return

   % One argument can only be 'linear', specifying linear least squares
   case 1
      if strncmpi(varargin{1}, 'linear', length(varargin{1}))
         fNonlinear = false;
         return
      else
         error('fitcircle:UnknownOption', 'Unknown Option')
      end

   % Otherwise we're left with user supplied parameters for Gauss Newton
   otherwise
      if rem(length(varargin), 2) ~= 0
         error('fitcircle:propertyValueNotPair', ...
            'Additional arguments must take the form of Property/Value pairs');
      end

      % Cell array of valid property names
      properties = {'maxits', 'tol'};

      while length(varargin) ~= 0
         property = varargin{1};
         value    = varargin{2};

         % If the property has been supplied in a shortened form, lengthen it
         iProperty = find(strncmpi(property, properties, length(property)));
         if isempty(iProperty)
            error('fitcircle:UnkownProperty', 'Unknown Property');
         elseif length(iProperty) > 1
            error('fitcircle:AmbiguousProperty', ...
               'Supplied shortened property name is ambiguous');
         end
```

```
        % Expand property to its full name
        property = properties{iProperty};

        switch property
           case 'maxits'
              if value <= 0
                 error('fitcircle:InvalidMaxits', ...
                    'maxits must be an integer greater than 0')
              end
              params.maxits = value;
           case 'tol'
              if value <= 0
                 error('fitcircle:InvalidTol', ...
                    'tol must be a positive real number')
              end
              params.tol = value;
        end % switch property
        varargin(1:2) = [];
     end % while

end % switch length(varargin)

end %parseinputs
```

References

1. M. A. El-Sayed, *Some Interesting Properties of Metals Confined in Time and Nanometer Space of Different Shapes.* Accounts of Chemical Research, 2001. **34**(4): p. 257-264.

2. W. Eberhardt, *Clusters as new materials.* Surface Science, 2002. **500**(1-3): p. 242-270.

3. Alan S. Edelstein and R. C. Cammarata, *Nanomaterials: synthesis, properties, and applications*. 1998: Institute of Physics Publishing, Bristol, U.K.

4. P. Buffat and J. P. Borel, *Size effect on the melting temperature of gold particles.* Physical Review A, 1976. **13**(6): p. 2287.

5. P. R. Couchman and W. A. Jesser, *Thermodynamic Theory of Size Dependence of Melting Temperature in Metals.* Nature, 1977. **269**: p. 481-483.

6. Z. Tang and N. A. Kotov, *One-Dimensional Assemblies of Nanoparticles: Preparation, Properties, and Promise.* Advanced Materials, 2005. **17**(8): p. 951-962.

7. R. Shenhar, T. B. Norsten, and V. M. Rotello, *Polymer-Mediated Nanoparticle Assembly: Structural Control and Applications.* Advanced Materials, 2005. **17**(6): p. 657-669.

8. C. J. Murphy, T. K. Sau, A. M. Gole, C. J. Orendorff, J. Gao, L. Gou, S. E. Hunyadi, and T. Li, *Anisotropic Metal Nanoparticles: Synthesis, Assembly, and Optical Applications.* The Journal of Physical Chemistry B, 2005. **109**(29): p. 13857-13870.

9. H. K. Seung, P. Heng, P. G. Costas, K. L. Christine, M. J. F. Jean, and P. Dimos, *All-inkjet-printed flexible electronics fabrication on a polymer substrate by low-*

temperature high-resolution selective laser sintering of metal nanoparticles. Nanotechnology, 2007. **18**(34): p. 345202.

10. V. Subramanian, J. M. J. Frechet, P. C. Chang, D. C. Huang, J. B. Lee, S. E. Molesa, A. R. Murphy, D. R. Redinger, and S. K. Volkman, *Progress Toward Development of All-Printed RFID Tags: Materials, Processes, and Devices.* Proceedings of the IEEE, 2005. **93**(7): p. 1330-1338.

11. B. Crone, A. Dodabalapur, A. Gelperin, L. Torsi, H. E. Katz, A. J. Lovinger, and Z. Bao, *Electronic sensing of vapors with organic transistors.* Applied Physics Letters, 2001. **78**(15): p. 2229-2231.

12. S. P. Price, J. Henzie, and T. W. Odom, *Addressable, Large-Area Nanoscale Organic Light-Emitting Diodes.* Small, 2007. **3**(3): p. 372-374.

13. G. E. Moore, *Cramming more components onto integrated circuits.* Electronics, 1965. **38**(8).

14. *International Technology Roadmap for Semiconductors, http://public.itrs.net.*

15. M. C. Daniel and D. Astruc, *Gold nanoparticles: Assembly, supramolecular chemistry, quantum-size-related properties, and applications toward biology, catalysis, and nanotechnology.* Chemical Reviews, 2004. **104**(1): p. 293-346.

16. M. Valden, X. Lai, and D. W. Goodman, *Onset of Catalytic Activity of Gold Clusters on Titania with the Appearance of Nonmetallic Properties.* Science, 1998. **281**(5383): p. 1647-1650.

17. M. S. Chen and D. W. Goodman, *The Structure of Catalytically Active Gold on Titania.* Science, 2004. **306**(5694): p. 252-255.

18. P. J. Ferreira, G. J. la O, Y. Shao-Horn, D. Morgan, R. Makharia, S. Kocha, and H. A. Gasteiger, *Instability of Pt/C electrocatalysts in proton exchange membrane*

fuel cells - A mechanistic investigation. Journal of the Electrochemical Society, 2005. **152**(11): p. A2256-A2271.

19. Y. Shao-Horn, W. C. Sheng, S. Chen, P. J. Ferreira, E. F. Holby, and D. Morgan, *Instability of supported platinum nanoparticles in low-temperature fuel cells.* Topics in Catalysis, 2007. **46**(3-4): p. 285-305.

20. J. G. Bai, Z. Z. Zhang, J. N. Calata, and G. Q. Lu, *Low-temperature sintered nanoscale silver as a novel semiconductor device-metallized substrate interconnect material.* Ieee Transactions on Components and Packaging Technologies, 2006. **29**(3): p. 589-593.

21. M. Maruyama, R. Matsubayashi, H. Iwakuro, S. Isoda, and T. Komatsu, *Silver nanosintering: a lead-free alternative to soldering.* Applied Physics a-Materials Science & Processing, 2008. **93**(2): p. 467-470.

22. H. Ogura, M. Maruyama, R. Matsubayashi, T. Ogawa, S. Nakamura, T. Komatsu, H. Nagasawa, A. Ichimura, and S. Isoda, *Carboxylate-Passivated Silver Nanoparticles and Their Application to Sintered Interconnection: A Replacement for High Temperature Lead-Rich Solders.* Journal of Electronic Materials, 2010.

23. C. Herring, *Effect of Change of Scale on Sintering Phenomena.* Journal of Applied Physics, 1950. **21**(4): p. 301-303.

24. W. D. Kingery and M. Berg, *Study of the Initial Stages of Sintering Solids by Viscous Flow, Evaporation-Condensation, and Self-Diffusion.* Journal of Applied Physics, 1955. **26**(10): p. 1205-1212.

25. G. C. Kuczynski, *Self Diffusion in Sintering of Metallic Particles.* Trans. AIME, 1949. **185**: p. 169-178.

26. R. L. Coble, *Initial Sintering of Alumina and Hematite.* Journal of the American Ceramic Society, 1958. **41**(2): p. 55-62.

27. Y. Champion, F. Bernard, N. Guigue-Millot, and P. Perriat, *Sintering of copper nanopowers under hydrogen: an in situ X-ray diffraction analysis.* Materials Science and Engineering a-Structural Materials Properties Microstructure and Processing, 2003. **360**(1-2): p. 258-263.

28. J. R. Groza, *Nanosintering.* Nanostructured Materials, 1999. **12**(5-8): p. 987-992.

29. M. Yeadon, J. C. Yang, R. S. Averback, J. W. Bullard, and J. M. Gibson, *Sintering of silver and copper nanoparticles on (001) copper observed by in-situ ultrahigh vacuum transmission electron microscopy.* Nanostructured Materials, 1998. **10**(5): p. 731-739.

30. J. R. Sambles, L. M. Skinner, and N. D. Lisgarten, *An Electron Microscope Study of Evaporating Small Particles - Kelvin Equation for Liquid Lead and Mean Surface Energy of Solid Silver.* Proceedings of the Royal Society of London Series A, 1970. **318**(1535): p. 507-522.

31. W. Thomson, *On the equilibrium of vapour at a curved surface of liquid.* Philosophical Magazine, 1871. **42**(282): p. 448-452.

32. S.-J. L. Kang, *Sintering : Densification, Grain Growth and Microstructure*. 2005, Butterworth-Heinemann: Burlington.

33. R. L. Coble, *Sintering Crystalline Solids. I. Intermediate and Final State Diffusion Models.* Journal of Applied Physics, 1961. **32**(5): p. 787.

34. M. N. Rahaman, *Ceramic Processing and Sintering*. 2nd ed. 2003, New York, NY: Marcel Dekker.

35. D. L. Johnson and I. B. Cutler, *Diffusion Sintering: I, Initial Stage Sintering Models and Their Application to Shrinkage of Powder Compacts.* Journal of the American Ceramic Society, 1963. **46**(11): p. 541-545.

36. J. Frenkel *Viscous Flow of Crystalline Bodies Under the Action of Surface Tension.* Journal of Physics (U.S.S.R.), 1945. **9**: p. 385.

37. A. J. Shaler, *Seminar on the Kinetics of Sintering.* Metals Transactions, 1949. **185**: p. 796.

38. F. A. Nichols and W. W. Mullins, *Morphological Changes of a Surface of Revolution due to Capillarity-Induced Surface Diffusion.* Journal of Applied Physics, 1965. **36**(6): p. 1826-1835.

39. P. Bross and H. E. Exner, *Computer simulation of sintering processes.* Acta Metallurgica, 1979. **27**(6): p. 1013-1020.

40. D. L. Johnson, *New Method of Obtaining Volume, Grain-Boundary, and Surface Diffusion Coefficients from Sintering Data.* Journal of Applied Physics, 1969. **40**(1): p. 192.

41. J. Svoboda and H. Riedel, *New solutions describing the formation of interparticle necks in solid-state sintering.* Acta Metallurgica et Materialia, 1995. **43**(1): p. 1-10.

42. F. N. Rhines and R. T. DeHoff. *Channel Network Decay in Sintering*. in *Sintering and Heterogeneous Catalysis (Proceedings of the Sixth International Conference on Sintering and Related Phenomena).* 1984. Notre Dame, IL, USA: Plenum Press.

43. M. H. Tikkanen and S. A. Makipirtti, *New phenomenological sintering equation.* International Journal of Powder Metallurgy, 1965. **1**(1): p. 15-22.

44. V. A. Ivensen, *Densification of metal powders during sintering*. 1973, New York: Consultants Bureau.

45. W. S. Coblenz, J. M. Dynys, R. M. Cannon, and R. L. Coble, *Initial stage solid state sintering models. A critical analysis and assessment.* Materials Science Research, 1980. **13**: p. 141-157.

46. E. A. Barringer and H. K. Bowen, *Formation, Packing, and Sintering of Monodisperse TiO2 Powders.* Journal of the American Ceramic Society, 1982. **65**(12): p. C-199-C-201.

47. D. L. Johnson, *New Method of Obtaining Volume, Grain-Boundary, and Surface Diffusion Coefficients from Sintering Data.* Journal of Applied Physics, 1969. **40**(1): p. 192-200.

48. B. Calvin H, *Sintering and redispersion of supported metals: Perspectives from the literature of the past decade*, in *Studies in Surface Science and Catalysis*, C. H. Bartholomew and G. A. Fuentes, Editors. 1997, Elsevier. p. 585-592.

49. C. Charles T, *Ultrathin metal films and particles on oxide surfaces: structural, electronic and chemisorptive properties.* Surface Science Reports, 1997. **27**(1-3): p. 1-111.

50. P. Wynblatt and N. A. Gjostein, *Supported metal crystallites.* Progress in Solid State Chemistry, 1975. **9**: p. 21-58.

51. P. Wynblatt and N. A. Gjostein, *Particle growth in model supported metal catalysts—I. Theory.* Acta Metallurgica, 1976. **24**(12): p. 1165-1174.

52. S. A. Stevenson, J. A. Dumesic, R. T. Baker, and E. Ruckenstein, *Metal-support interactions in catalysis, sintering, and redispersion*. Van Nostrand Reinhold catalysis series. 1987, Van Nostrand Reinhold Co.: New York.

53. H. L. Zhu and R. S. Averback, *Sintering processes of two nanoparticles: A study by molecular-dynamics.* Philosophical Magazine Letters, 1996. **73**(1): p. 27-33.

54. P. Zeng, S. Zajac, P. C. Clapp, and J. A. Rifkin, *Nanoparticle sintering simulations.* Materials Science and Engineering a-Structural Materials Properties Microstructure and Processing, 1998. **252**(2): p. 301-306.

55. S. Arcidiacono, N. R. Bieri, D. Poulikakos, and C. P. Grigoropoulos, *On the coalescence of gold nanoparticles.* International Journal of Multiphase Flow, 2004. **30**(7-8): p. 979-994.

56. L. Ding, R. L. Davidchack, and J. Pan, *A molecular dynamics study of sintering between nanoparticles.* Computational Materials Science, 2009. **45**(2): p. 247-256.

57. R. Theissmann, M. Fendrich, R. Zinetullin, G. Guenther, G. Schierning, and D. E. Wolf, *Crystallographic reorientation and nanoparticle coalescence.* Physical Review B, 2008. **78**(20): p. 205413.

58. J. Rankin and B. W. Sheldon, *In situ TEM sintering of nano-sized ZrO2 particles.* Materials Science and Engineering: A, 1995. **204**(1-2): p. 48-53.

59. K. Hajmrle and R. Angers, *Observation of silver particle rotation by in situ electron microscopy.* Scripta Metallurgica, 1972. **6**(11): p. 1071-1073.

60. Z. W. Shan, R. K. Mishra, S. A. S. Asif, O. L. Warren, and A. M. Minor, *Mechanical annealing and source-limited deformation in submicrometre-diameter Ni crystals.* Nature Materials, 2008. **7**(2): p. 115-119.

61. A. G. Guy, *Essentials of Materials Science*. 1976, New York: McGraw-Hill.

62. C. Greskovich and K. W. Lay, *Grain Growth in Very Porous Al2O3 Compacts.* Journal of the American Ceramic Society, 1972. **55**(3): p. 142-146.

63. P. C. Flynn and S. E. Wanke, *A model of supported metal catalyst sintering: II. Application of model.* Journal of Catalysis, 1974. **34**(3): p. 400-410.

64. E. Ruckenstein and B. Pulvermacher, *Growth kinetics and the size distributions of supported metal crystallites.* Journal of Catalysis, 1973. **29**(2): p. 224-245.

65. C. G. Granqvist and R. A. Buhrman, *Size distributions for supported metal catalysts: Coalescence growth versus ostwald ripening.* Journal of Catalysis, 1976. **42**(3): p. 477-479.

66. P. J. F. Harris, *Growth and Structure of Supported Metal Catalyst Particles.* International Materials Reviews, 1995. **40**(3): p. 97-115.

67. C. T. Campbell, S. C. Parker, and D. E. Starr, *The Effect of Size-Dependent Nanoparticle Energetics on Catalyst Sintering.* Science, 2002. **298**(5594): p. 811-814.

68. J. Sehested, J. A. P. Gelten, I. N. Remediakis, H. Bengaard, and J. K. Nørskov, *Sintering of nickel steam-reforming catalysts: effects of temperature and steam and hydrogen pressures.* Journal of Catalysis, 2004. **223**(2): p. 432-443.

69. S. E. Wanke, *Comments on the sintering mechanism of supported metal catalysts.* Journal of Catalysis, 1977. **46**(2): p. 234-237.

70. T. R. Linderoth, S. Horch, L. Petersen, S. Helveg, E. Lægsgaard, I. Stensgaard, and F. Besenbacher, *Novel Mechanism for Diffusion of One-Dimensional Clusters: Pt/Pt(110)-(1×2).* Physical Review Letters, 1999. **82**(7): p. 1494-1497.

71. K. Morgenstern, G. Rosenfeld, and G. Comsa, *Local correlation during Ostwald ripening of two-dimensional islands on Ag(111).* Surface Science, 1999. **441**(2-3): p. 289-300.

72. M. J. J. Jak, C. Konstapel, A. van Kreuningen, J. Verhoeven, and J. W. M. Frenken, *Scanning tunnelling microscopy study of the growth of small palladium particles on TiO2(110).* Surface Science, 2000. **457**(3): p. 295-310.

73. F. Yang, M. S. Chen, and D. W. Goodman, *Sintering of Au Particles Supported on TiO2(110) during CO Oxidation.* The Journal of Physical Chemistry C, 2008. **113**(1): p. 254-260.

74. P. Stone, S. Poulston, R. A. Bennett, and M. Bowker, *Scanning tunnelling microscopy investigation of sintering in a model supported catalyst: nanoscale Pd on TiO2(110).* Chemical Communications, 1998(13): p. 1369-1370.

75. K. Heinemann and H. Poppa, *Direct observation of small cluster mobility and ripening.* Thin Solid Films, 1976. **33**(2): p. 237-251.

76. R. Anton and P. Kreutzer, *In situ TEM evaluation of the growth kinetics of Au particles on highly oriented pyrolithic graphite at elevated temperatures.* Physical Review B, 2000. **61**(23): p. 16077-16083.

77. R. J. Liu, P. A. Crozier, C. M. Smith, D. A. Hucul, J. Blackson, and G. Salaita, *Metal sintering mechanisms and regeneration of palladium/alumina hydrogenation catalysts.* Applied Catalysis A: General, 2005. **282**(1-2): p. 111-121.

78. S. B. Simonsen, I. Chorkendorff, S. Dahl, M. Skoglundh, J. Sehested, and S. Helveg, *Direct Observations of Oxygen-induced Platinum Nanoparticle Ripening Studied by In Situ TEM.* Journal of the American Chemical Society, 2010. **132**(23): p. 7968-7975.

79. M. Jose-Yacaman, C. Gutierrez-Wing, M. Miki, D. Q. Yang, K. N. Piyakis, and E. Sacher, *Surface diffusion and coalescence of mobile metal nanoparticles.* Journal of Physical Chemistry B, 2005. **109**(19): p. 9703-9711.

80. R. T. K. Baker, P. S. Harris, and R. B. Thomas, *Direct observation of particle mobility on a surface in a gaseous environment.* Surface Science, 1974. **46**(1): p. 311-316.

81. Y. Chen, R. E. Palmer, and J. P. Wilcoxon, *Sintering of passivated gold nanoparticles under the electron beam.* Langmuir, 2006. **22**(6): p. 2851-2855.

82. W. J. Zhang and D. E. Miser, *Coalescence of oxide nanoparticles: In situ HRTEM observation.* Journal of Nanoparticle Research, 2006. **8**(6): p. 1027-1032.

83. K. Hajmrle and R. Angers, *Sintering Study of Silver Particles by In Situ Electron Microscopy.* Metallurgical Transactions, 1974. **5**(4): p. 817-822.

84. F. Banhart, *In-situ Electron Microscopy at High Resolution*. 2008: World Scientific.

85. H. Saka, T. Kamino, S. Arai, and K. Sasaki, *In situ heating transmission electron microscopy.* MRS Bulletin, 2008. **33**(2): p. 93-100.

86. K. Takayanagi, K. Yagi, K. Kobayashi, and G. Honjo, *Techniques for routine UHV in situ electron microscopy of growth processes of epitaxial thin films.* Journal of Physics E: Scientific Instruments, 1978. **11**(5): p. 441.

87. W. T. Nichols, J. W. Keto, D. E. Henneke, J. R. Brock, G. Malyavanatham, M. F. Becker, and H. D. Glicksman, *Large-scale production of nanocrystals by laser ablation of microparticles in a flowing aerosol.* Applied Physics Letters, 2001. **78**(8): p. 1128-1130.

88. L. F. Allard, W. C. Bigelow, M. Jose-Yacaman, D. P. Nackashi, J. Damiano, and S. E. Mick, *A new MEMS-based system for ultra-high-resolution imaging at elevated temperatures.* Microscopy Research and Technique, 2009. **72**(3): p. 208-215.

89. Y. Ding, F. R. Fan, Z. Q. Tian, and Z. L. Wang, *Sublimation-Induced Shape Evolution of Silver Cubes.* Small, 2009. **5**(24): p. 2812-2815.

90. J. G. Lee, J. Lee, T. Tanaka, and H. Mori, *In situ HREM observation of crystalline-to-gas transition in nanometer-sized Ag particles.* Physical Review Letters, 2006. **96**(7): p. 075504.

91. L. W. Hobbs, *Introduction to analytical electron microscopy*, ed. J. J. Hren, J. I. Goldstein, and D. C. Joy. 1979, New York: Plenum Press.

92. V. G. Gryaznov, A. M. Kaprelov, and A. Y. Belov, *Real temperature of nanoparticles in electron microscope beams.* Philosophical Magazine Letters, 1991. **63**(5): p. 275-279.

93. W. Gander, G. H. Golub, and R. Strebel, *Least-Squares Fitting of Circles and Ellipses.* Bit, 1994. **34**(4): p. 558-578.

94. L. E. Murr, *Interfacial Phenomena in Metals and Alloys*. 1975, London: Addison-Wesley.

95. P. E. Batson, A. Reyes-Coronado, R. G. Barrera, A. Rivacoba, P. M. Echenique, and J. Aizpurua, *Plasmonic Nanobilliards: Controlling Nanoparticle Movement Using Forces Induced by Swift Electrons.* Nano Letters, 2011. **11**(8): p. 3388-3393.

96. P. E. Batson, *Motion of Gold Atoms on Carbon in the Aberration-Corrected STEM.* Microscopy and Microanalysis, 2008. **14**(01): p. 89-97.

97. J. Rankin and L. A. Boatner, *Unstable Neck Formation during Initial-Stage Sintering.* Journal of the American Ceramic Society, 1994. **77**(8): p. 1987-1990.

98. P. Shewmon, *Diffusion in Solids*. 2nd ed. 1989, Warrendale, Pennsylvania: The Minerals, Metals and Materials Society. p. 200.

99. J. M. Blakely and H. Mykura, *Surface self diffusion and surface energy measurements on platinum by the multiple scratch method.* Acta Metallurgica, 1962. **10**(5): p. 565-572.

100. N. L. Peterson, *Grain-Boundary Diffusion in Metals.* International Metals Reviews, 1983. **28**(2): p. 65-91.

101. G. E. Rhead, *Surface self-diffusion of silver in various atmospheres.* Acta Metallurgica, 1965. **13**(3): p. 223-226.

102. W. W. Pai, A. K. Swan, Z. Zhang, and J. F. Wendelken, *Island Diffusion and Coarsening on Metal (100) Surfaces.* Physical Review Letters, 1997. **79**(17): p. 3210-3213.

103. J. M. Wen, S. L. Chang, J. W. Burnett, J. W. Evans, and P. A. Thiel, *Diffusion of Large Two-Dimensional Ag Clusters on Ag(100).* Physical Review Letters, 1994. **73**(19): p. 2591-2594.

104. J. M. Wen, J. W. Evans, M. C. Bartelt, J. W. Burnett, and P. A. Thiel, *Coarsening Mechanisms in a Metal Film: From Cluster Diffusion to Vacancy Ripening.* Physical Review Letters, 1996. **76**(4): p. 652-655.

105. H. Brune, K. Bromann, H. Roder, K. Kern, J. Jacobsen, P. Stoltze, K. Jacobsen, and J. Norskov, *Effect of strain on surface diffusion and nucleation.* Physical Review B, 1995. **52**(20): p. 14380-14383.

106. E. Z. Luo, J. Wollschlager, F. Wegner, and M. Henzler, *SPA-LEED studies of growth of Ag on Ag(111) at low temperatures* Applied Physics a-Materials Science & Processing, 1995. **60**(1): p. 19-25.

107. D. Stark, *Diffusion processes on stepped surfaces of thin metal films: Migration of silver adatoms on silver (111) terraces.* Surface Science, 1987. **189**: p. 1111-1116.

108. P. Offermann, *Ag-diffusion in PyC.* Journal of Nuclear Materials, 1977. **64**(3): p. 249-253.

109. H. Kawasaki, G. Sakai, and T. Kijima, *Direct observation of dynamic shape transformation and coalescence in platinum nanosheets on graphite surface at room temperature by time-resolved AFM.* Applied Surface Science, 2006. **253**(3): p. 1512-1516.

110. T. R. Linderoth, S. Horch, E. Laegsgaard, I. Stensgaard, and F. Besenbacher, *Surface diffusion of Pt on Pt(110): Arrhenius behavior of long jumps.* Physical Review Letters, 1997. **78**(26): p. 4978-4981.

111. M. L. Marcos and J. González Velasco, *Measurement of surface diffusion coefficients in air of columnar structured platinum near room temperature.* Chemical Physics Letters, 1998. **283**(5-6): p. 391-394.

112. R. Vandermeer, D. Jensen, and E. Woldt, *Grain boundary mobility during recrystallization of copper.* Metallurgical and Materials Transactions A, 1997. **28**(3): p. 749-754.

113. M. L. Taheri, D. Molodov, G. Gottstein, and A. D. Rollett, *Grain boundary mobility under a stored-energy driving force: a comparison to curvature-driven boundary migration.* Zeitschrift Fur Metallkunde, 2005. **96**(10): p. 1166-1170.

114. C. C. Yang, A. D. Rollett, and W. W. Mullins, *Measuring relative grain boundary energies and mobilities in an aluminum foil from triple junction geometry.* Scripta Materialia, 2001. **44**(12): p. 2735-2740.

115. G. Antczak and G. Ehrlich, *Surface diffusion : metals, metal atoms, and clusters*. 2010, New York: Cambridge University Press.

116. M. Gammage, *Personal communication*.

Vita

Michael Adewunmi Asoro attended the University of Lagos, Nigeria where he obtained a Bachelor of Science degree (First Class Honors) in Metallurgical and Materials Engineering in December 2006. In August 2007, he began his graduate study at the University of Texas at Austin and obtained a Master of Science in Engineering degree in Materials Science and Engineering in August 2009. He then continued with his graduate studies towards obtaining a PhD in Materials Science and Engineering. During his graduate study he received several awards including: The American Ceramic Society (ACerS) Graduate Excellence in Materials Science (GEMS) Diamond Award, Ralph Nelson Endowed Graduate School Continuing Fellowship, Nano Portfolio Student Travel Award, Graduate Student Professional Development Award and The Graduate School Pre-emptive Recruitment Fellowship. While obtaining his degree, he worked as a Teaching Assistant for Materials Processing Laboratory in the Mechanical Engineering department, as a Graduate Research Assistant in the Materials Science and Engineering Graduate Program and as a Summer Engineering Intern at ExxonMobil Upstream Research Company in Houston, Texas. After graduation, Michael Adewunmi Asoro will join Intel Corporation's Portland Technology Development in Hillsboro, Oregon as a Module & Integration Yield Engineer.

Email address: michaelasoro@utexas.edu

This dissertation was typed by the author.